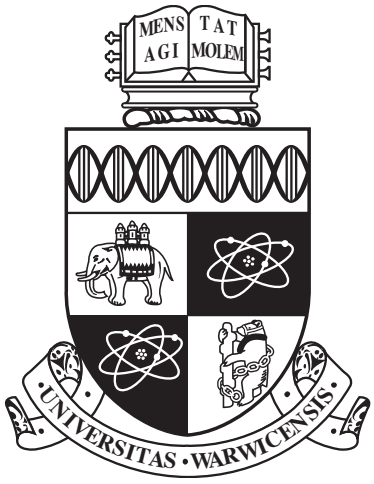

Image based modelling of bleb site selection

by

Sharon Collier

Thesis

Submitted to the University of Warwick

for the degree of

Doctor of Philosophy

MOAC

December 2017

THE UNIVERSITY OF
WARWICK

Contents

List of Tables **vi**

List of Figures **vii**

Acknowledgments **ix**

Declarations **x**

Abstract **xi**

Abbreviations **xiii**

Chapter 1 Introduction **1**

1.1 The role of blebbing in cell motility 1

1.1.1 Eukaryotic cell migration and cellular blebbing 1

1.1.2 Phases of the blebbing lifecycle 2

1.1.3 A constructive role for blebbing: migration in 3D resistive environments 5

1.2 Motivation: How are bleb sites selected? 6

1.2.1 Possible mechanisms for directing blebs to the cell front 6

1.3 *Dictyostelium* as a model organism 9

1.3.1 Chemotaxis in *Dictyostelium*: directed cell migration 9

1.3.2 Blebbing in *Dictyostelium* 12

1.3.3 Genetic control of blebbing 12

1.4 Existing numerical models for blebbing 16

1.5 The role of membrane tension 21

1.5.1 A biophysical model for curvature dependent bleb nucleation . . . 22

1.6 Project aims 23

Chapter 2 Theoretical methods **26**
2.1 Derivation of model equations: Overview . . . 26
2.2 Model framework . . . 26
2.3 Notation . . . 27
2.4 Functional form of the total membrane energy . . . 29
2.4.1 Membrane tension energy . . . 29
2.4.2 Membrane bending energy . . . 30
2.4.3 Test simulation for equivalence of curvature output for different parameterisations . . . 32
2.4.4 Membrane tension energy (including resting length) . . . 33
2.4.5 Coupling energy . . . 34
2.5 PDE for membrane displacement . . . 35
2.6 Motivation: principles from the calculus of variations . . . 36
2.6.1 Overview . . . 36
2.6.2 Variation of a general functional: Weak and strong forms of the Euler-Lagrange equations . . . 37
2.7 Determining the first variation of the membrane energy functional . . . 38
2.8 Numerical scheme . . . 41
2.9 Dimensional analysis . . . 42
2.10 Initialising model geometry from real cell contours . . . 45
2.10.1 QuimP work flow . . . 45
2.10.2 Generating model membrane, cortex and linker positions . . . 46
2.11 χ^2 test- statistical significance with respect to random bleb site selection . 48
2.12 Determining cellular polarisation axis . . . 49
2.12.1 Algorithm for automatic detection of the cell front, and calculation of cellular polarisation . . . 49
2.13 Kuiper test . . . 50
2.14 Fluorescence analysis . . . 50

Chapter 3 Experimental methods **52**
3.1 Overview . . . 52
3.2 Media . . . 52
3.3 Cell strains used . . . 53
3.4 *Dictyostelium* cell culture . . . 53
3.4.1 Axenic growth . . . 53
3.4.2 Growth in association with bacteria . . . 54

3.4.3 Harvesting and counting cells . . . 55
3.4.4 Strain preservation . . . 56
3.5 Establishing aggregation competent cells . . . 56
3.5.1 cAMP pulsing . . . 58
3.5.2 Overnight starvation . . . 58
3.6 Under agarose assay . . . 59
3.7 Imaging . . . 60
3.7.1 Factors influencing the quality of microscopy images . . . 61
3.8 Molecular cloning techniques . . . 62
3.8.1 Polymerase chain reaction . . . 62
3.8.2 Transformation into *E.coli* . . . 62
3.8.3 Plasmid purification . . . 63
3.8.4 Restriction digests and ligations . . . 63
3.8.5 Transformation into *Dictyostelium* . . . 63
3.9 Creation of a TalinA reporter . . . 64
3.10 Generating a fluorescently tagged TalinA knock-in . . . 67

Chapter 4 Development of a quantitative method for predicting bleb site selection 69
4.1 Motivation . . . 69
4.2 Influence of hydrostatic pressure on global blebbing propensity . . . 69
4.2.1 Identification of a critical pressure . . . 69
4.2.2 Relation between hydrostatic pressure and cellular circularity . . . 70
4.3 Optimizing the hydrostatic pressure parameter . . . 70
4.3.1 ROC curve analysis . . . 73
4.3.2 Summary data . . . 73
4.3.3 Method caveats . . . 75
4.4 Automatic bleb tracking (experimental data) . . . 76
4.5 Hydrostatic pressure as a bleb likelihood gauge . . . 78
4.5.1 Algorithm . . . 80
4.5.2 A threshold value for blebbing: optimising specificity and sensitivity 80
4.5.3 Bleb likelihood parameter distributions . . . 81
4.5.4 Bleb classification and localisation . . . 81
4.5.5 Predictive power of the model . . . 84
4.5.6 Method caveats . . . 86
4.6 Linker length as a bleb likelihood gauge . . . 86

4.6.1 Ranking bleb sites . . . 86
4.6.2 Method advantages . . . 87
4.7 Method validation . . . 87
4.7.1 Equivalence of ranked bleb order at sub-critical pressure, and the order blebs nucleate in upon increasing pressure . . . 87
4.7.2 Robustness of model with respect to node density . . . 89
4.7.3 Membrane peeling . . . 90

Chapter 5 Low vs high resistance: Is geometry always the determining factor? 94
5.1 Linker strain as a measure for local blebbing propensity . . . 94
5.2 Low resistive environments: additional mechanism required to restrict likely bleb sites to the cell front . . . 96
5.3 Uropod retraction and protrusion retractions affect local blebbing propensity . . . 100

Chapter 6 The influence of talin localisation in bleb polarisation 102
6.1 Motivation . . . 102
6.2 Talin knock-out cells bleb profusely . . . 102
6.3 TalinA spatial distribution: enrichment at the cell rear . . . 103
6.4 Talin enrichment is inversely proportional to blebbing frequency . . . 103
6.5 Inclusion of a linker stiffness gradient greatly improves model fit for cells moving in low resistive environments . . . 110

Chapter 7 Ongoing work 114
7.1 Multi-blebbing . . . 114
7.1.1 Motivation . . . 114
7.1.2 Characteristic time delay observed before the nucleation of daughter blebs . . . 114
7.1.3 Possible mechanisms for multi-blebbing: daughter blebbing vs. lobopodia . . . 115
7.1.4 Effect of repeated daughter blebbing on cell shape . . . 118
7.2 Towards a 3D visualisation of blebbing: diSPIM microscopy . . . 119
7.2.1 Motivation . . . 119
7.2.2 Is geometry driven bleb site selection a general mechanism? . . . 119
7.2.3 diSPIM imaging . . . 123
7.2.4 Microscope configuration . . . 124

7.2.5 Deconvolution 124
7.2.6 Preliminary results 126
7.2.7 Capturing blebbing in 3D 126
7.2.8 Macropinosomes 126

Chapter 8 Discussion and conclusions **129**
8.1 Discussion 129
8.1.1 Disentangling physical and biological mechanisms for bleb site selection 129
8.1.2 Extension to a stochastic model and time dependence of bleb nucleation 132
8.1.3 Extension of the model to 3D surfaces: using diSPIM data to initialize the model 132
8.2 Conclusions 133
.1 Code 136
.2 Optimisation of hydrostatic pressure: results tables 144
.3 Myosin-II distribution in chemotaxing *Dictyostelium* cells 147

List of Tables

2.1 SI units of all parameters 43

4.1 ROC curve summary data 75

1 2% agarose data results 145
2 0.7% agarose data results 146

List of Figures

1.1 Blebbing Lifecycle: . . . 4
1.2 Proposed mechanisms to direct blebbing activity to the cell front . . . 8
1.3 Blebbing in Dictyostelium . . . 13
1.4 Tyson model . . . 22

2.1 Thin cross section . . . 27
2.2 Model framework . . . 28
2.3 Circle test simulation . . . 32
2.4 Forces acting on membrane nodes . . . 36
2.5 QuimP segmentation . . . 47

3.1 *Dictyostelium*: social amoeba lifecycle . . . 57
3.2 Under agarose assay . . . 60
3.3 PJet-TalinA plasmid map . . . 65
3.4 TalinA-mNeon plasmid map . . . 66

4.1 Identification of a critical pressure . . . 71
4.2 Pressure vs circularity . . . 72
4.3 Model vs experimental bleb nucleation . . . 74
4.4 Automatically tracked blebs . . . 77
4.5 Automatic bleb tracking based on motility and fluorescence maps . . . 79
4.6 Distributions of bleb likelihood, using hydrostatic pressure as a bleb likelihood gauge . . . 82
4.7 Bleb likelihood ROC curves using hydrostatic pressure as a bleb likelihood gauge . . . 83
4.8 Classification of bleb sites: 2% agarose . . . 84
4.9 Classification of bleb sites: 0.7% agarose . . . 85
4.10 Ranking predicted bleb sites . . . 88

4.11 Equivalence of linker and pressure methods 89
4.12 Robustness of model to varying node spacing 91
4.13 Membrane peeling 93

5.1 Bleb likelihood distributions, as determined by linker length 95
5.2 Cell paths 97
5.3 Cellular circularity 98
5.4 Angular bleb distributions: experiment vs model 99
5.5 Uropod and protrusion retractions influence blebbing propensity 101

6.1 Talin knockout cells bleb profusely 104
6.2 TalinA-mNeon localisation in aggregation competent cells in buffer 105
6.3 TalinA-mNeon localisation in vegetative cells 105
6.4 Experimentally observed gradients in TalinA-mNeon fluorescence 106
6.5 TalinA-mNeon exhibits an exponentially graded distribution 107
6.6 Bleb location in TalinA-mNeon cells 108
6.7 Talin enrichment is inversely proportional to blebbing frequency 109
6.8 Inclusion of a linker stiffness gradient greatly improves model fit for cells moving in low resistive environments 112
6.9 Angular frequency distribution of model vs experimental bleb sites after inclusion of a linker gradient 113

7.1 Actin build up dynamics 115
7.2 Model multi-blebbing mechanisms 117
7.3 Decay of cellular polarisation 118
7.4 Model evolution over time by repeated daughter blebbing 120
7.5 *Dictyostelium* vs Fundulus deep cell 121
7.6 Fundulus deep bleb distribution 122
7.7 diSPIM configuration 125
7.8 3D blebbing 127
7.9 3D macropinosomes 128

1 Anterior to posterior myosin-II distribution. 147

Acknowledgments

I would like to thank the following people for their time and support.

Supervisors and colleagues:

Till Bretschneider

Rob Kay

Peggy Paschke

Richard Tyson

Evgeny Zatulovskiy

David Traynor

Andrew McAinsh

Muriel Erent

Friends and family:

Ben Collier

Richard Molyneux

Bronia Cross

Hamdi Hussain

David McCormack

Gina Grundy

Funding:

MOAC

EPSRC

This thesis was typeset with LaTeX 2$_\varepsilon$[1] by the author.

[1] LaTeX 2$_\varepsilon$ is an extension of LaTeX. LaTeX is a collection of macros for TeX. TeX is a trademark of the American Mathematical Society. The style package *warwickthesis* was used.

Declarations

This thesis is presented in accordance with the regulations for the degree of Doctor of Philosophy. It has been composed by myself and has not been submitted in any previous application for any degree. The work in this thesis has been undertaken by myself except where otherwise stated.

Abstract

Cellular blebs are fast, pressure-driven protrusions of the cell membrane that are initially devoid of F-actin. Although blebs have often been overlooked as a functional part of cell motility, blebbing has been shown to play an important role in migration in 3D mechanically resistive environments, such as movement through densely packed tissues. The location of bleb nucleation sites is often assumed to be entirely stochastic, however, cells migrating using blebbing motility have been repeatedly observed to perform persistent, directional movement. Given the compelling evidence on the role of blebbing in directional cell migration, relatively little is known on the mechanisms of bleb site selection; how bleb sites are determined and directed to the cell front remains an open question.

Previously, Tyson et al. found that chemotaxing *Dictyostelium* cells preferentially bleb from concave regions, where membrane tension could facilitate membrane-cortex detachment. Based on this, a biophysical model for curvature dependent bleb nucleation was proposed, hinting at the possibility that polarised blebbing was due to physical forces alone.

We develop a novel image based modeling approach, using real cell contours from image data to initialise the model. This enables us to link quantitative experimental data and predictive modeling on the spatial distribution of blebs for the first time. We proceed to show that the extent to which cell geometry is a good predictor of bleb site selection is highly dependent on the degree of mechanical resistance the cells experience. For cells in highly resistive environments, where we observe the front and rear of the cell to be geometrically distinct, our novel modeling approach demonstrates that physical forces are sufficient to polarise blebbing activity in chemotaxing cells. For cells in low resistive environments however, where the front and rear of the cell are not geometrically distinct, we show that an additional mechanism is required to restrict blebbing to the cell front.

We propose this additional mechanism to be a front-to-rear gradient in the linker protein TalinA. Creation of a TalinA-mNeon construct allows us to experimentally confirm the existence of an asymmetric linker distribution. We incorporate the observed exponential linker gradient within the model. Inclusion of this mechanism increases the predictive power of the model, with regard to the spatial distribution of experimentally observed bleb sites, through efficiently directing blebbing activity to the cell front.

We have created a method which links quantitative experimental data and predictive modeling, this tool allows us to disentangle the role of physical forces and biological mechanisms in the prediction of bleb nucleation sites.

Resulting Publications

- Collier, S., P. Paschke, R. R. Kay, Bretschneider, T. (2017). *Image based modeling of bleb site selection*. Scientific Reports, Pp. 312. DOI:10.1038/s41598-017-06875-9

- Baniukiewicz, P., Bretschneider, T., Collier, S. (2017). *QuimP- Analyzing transmembrane signalling in highly deformable cells*. Submitted. DOI: http://dx.doi.org/10.1101/171199.

Abbreviations

- ABD Actin Binding Domain
- Akt/PKB Serine/threonine protein kinase, otherwise known as protein kinase B.
- Arp2/3 Actin related proteins 2 and 3
- cAMP cyclic Adenosine MonoPhosphate
- cAR cyclic Adenosine monophosphate Receptor
- CDF Cumulative Distribution Function
- CRAC Cytosolic Regulator of Adenylyl Cyclase
- DIC Differential Interference Contrast Microscopy
- diSPIM dual-view inverted Selective Plane Illumination Microscope
- ECM Extra Cellular Matrix
- ECMM Electrostatic Contour Migration Method
- F-actin Filamentous-actin
- FERM 4.1 protein Ezrin, Radixin, Moesin
- FN False Negative
- FP False Positive
- GDP Guanosine DiPhosphate

- G-protein Guanine nucleotide-binding proteins
- GTP Guanosine TriPhosphate
- LEGI Local Excitation and Global Inhibition
- LSCM Laser Scanning Confocal Microscopy
- ODE Ordinary Differential Equation
- PCR Polymerase Chain Reaction
- PDE Partial Differential Equation
- PGC Primordial Germ Cell
- PH Pleckstrin Homology
- PI3K PhosphoInositide-3-Kinases
- PtdIns(3,4,5)P˙3 Phosphatidylinositol 3,4,5-triPhosphate
- PtdIns(4,5)P˙2 Phosphatidylinositol 4,5-bisPhosphate
- PTEN Phosphatase and TENsin homolog
- QuimP Quantitative Imaging of Membrane Proteins
- ROC Receiver Operator Characteristics
- SDCM Spinning Disc Confocal Microscopy
- SM Slime Mould
- TN True Negative
- TP True Positive

Chapter 1

Introduction

1.1 The role of blebbing in cell motility

1.1.1 Eukaryotic cell migration and cellular blebbing

The ability of eukaryotic cells to migrate directionally and efficiently is fundamental to a large variety of biological processes, including embryonic development, wound healing and targeted immune response to sites of inflammation [Furuta et al., 1995] [Kim et al., 1998] [Frangogiannis et al., 2002] [Rakic et al., 1994] . As such, disruptions to the functionality of cell motility can have profound effects on these processes, and have been associated with vascular disease, multiple sclerosis and tumour metastasis [Dellas et al., 2005]. Determining the mechanisms through which cells polarise and generate directional movement is therefore paramount to the development of therapeutic drugs for controlling such diseases.

Early studies of motility in crawling cells, such as neutrophils, fibroblasts and the soil amoeba *Dictyostelium*, revealed that cells migrate through successive expansions of the leading edge, and contraction of the cell rear [Mitchison and Cramer, 1996]. The most commonly studied method of leading edge extension is that driven by actin polymerisation. Monomeric actin is a globular protein, which when polymerised, forms microfilaments. These microfilaments are polar structures, with assembly and disassembly of the filament nucleating at opposite ends [Svitkina and Borisy, 1999]. The force exerted on the plasma membrane due to the rapid polymerisation of actin filaments is generally considered the main mechanism in driving the protrusion of the leading edge [Pollard and Borisy, 2003]. Filamentous actin (F-actin) can form branched networks which constitute a large proportion of the cellular cytoskeleton, contributing

to structural integrity, whilst the interaction with molecular motors also provides a critical role in motility through generating contractile forces [Insall and Machesky, 2009] [Mogilner and Oster, 1996]. Complete forward motion of the cell body consists of four distinct morphological stages: (i) protrusion of the leading edge, (ii) adhesion to the underlying substrate via focal adhesion complexes, (iii) contraction of the cortex, which pulls on the focal adhesions and thereby generates traction, and finally, (iv) de-adhesion at the trailing edge and disassembly of focal adhesions [Pollard and Borisy, 2003] [Ananthakrishnan and Ehrlicher, 2007].

An alternative mechanism for extension of the leading edge in migrating cells is through hydrostatic pressure dependent blebs [Charras and Paluch, 2008]. Blebs arise when the membrane locally detaches from the underlying actin cortex, and bulges outwards due to the flow of pressurised cytosol into the weakened section [Charras et al., 2008] [Goudarzi et al., 2012]. This intracellular fluid pressure arises due to the contraction of the acto-myosin cortex.

Although blebbing is often associated with apoptosis, it has also been shown to have a functional role in cell migration, particularly for cells moving through mechanically resistive environments, such as in densely packed tissues [Lämmermann and Sixt, 2009]. Blebbing motility has historically been overshadowed compared to studies of actin based protrusions (lamellipodia, pseudopodia and fillopodia), however, in recent years growing interest in the field has lead to numerous experimental and modelling advances into the mechanism of bleb nucleation, which we present in sections 1.3.3 and 1.4.

1.1.2 Phases of the blebbing lifecycle

The complete lifecycle of a bleb consists of three phases, (i) nucleation, (ii) expansion and (iii) retraction, although it is necessary to note that when used as a migratory mechanism, blebs are often not retracted, to enable sustained forward motion of the cell body [Charras and Paluch, 2008] [Fackler and Grosse, 2008] [Fink, 2003]. Here we briefly introduce some of the underlying mechanisms responsible for each stage in the lifecycle, although a more detailed consideration of the genetic regulation of these factors is discussed in section 1.3.3.

(i) Nucleation:

Bleb nucleation requires the existence of a small section of the plasma membrane to be uncoupled from the actin cortex. This can occur through either cortical rupture (figure 1.1 a1), where a tear forms in the actin cortex [Keller and Eggli, 1998] [Paluch et al., 2005], or through detachment of the linker proteins that adhere the membrane to the cortex [Cunningham, 1995] (figure 1.1 a2). Bleb nucleation due to linker detachment has been observed in numerous cell types, including *Dictyostelium*, Fundulus deep cells, zebrafish primordial germ cells (PGCs), and Walker carcinosarcoma cells [Zatulovskiy et al., 2014] [Fink, 2003] [Blaser et al., 2006] [Keller et al., 2002]. Bleb nucleation via cortical rupture is less commonly observed, although it has been shown to occur in Formin A deficient mutant *Dictyostelium* cells, where the mechanical integrity of the actin cortex is severely compromised [Ramalingam et al., 2015]. Bleb nucleation due to cortical rupture can also be artificially induced, by laser ablation [Peukes and Betz, 2014] [Goudarzi et al., 2012] [Tinevez et al., 2009].

(ii) Expansion:
The intracellular pressure due to acto-myosin contractility results in rapid expansion of the section of uncoupled membrane devoid of F-actin, into a hemi-spherical blister like protrusion [Langridge and Kay, 2006] [Yoshida and Soldati, 2006] [Jaglarz and Howard, 1995] [Fink, 2003] [Blaser et al., 2006] (figure 1.1 b1,b2). The timescale over which growth of the bleb continues differs dependent on cell type- for mammalian cells it can last for 5-30 seconds [Charras et al., 2008], whereas for *Dictyostelium* cells expansion is complete within 2 seconds [Zatulovskiy et al., 2014] [Fackler and Grosse, 2008]. The speed of bleb expansion is on average much faster than extension due to actin polymerisation [Charras and Paluch, 2008] [Yoshida and Soldati, 2006], with maximum protrusion speed of blebs in *Dictyostelium* observed to be approximately three times faster than that of pseudopodia [Zatulovskiy et al., 2014].

(iii) Retraction:
Bleb retraction relies on the repolymerisation of the actin cortex at the blebbed membrane (and recoupling via linker proteins), and recruitment of myosin to the new cortex [Charras et al., 2006] Keller and Eggli [1998] Fink [2003] (figure 1.1 c,d). Both of these processes can begin during bleb expansion, and may play a role in cessation of expansion as well as in retraction of the bleb [Cunningham et al., 1992] [Charras et al., 2006]. The cortex left behind by the blebbed membrane is simultaneously disassembled, unless of course the nucleation mechanism leading to the bleb was cortical rupture.

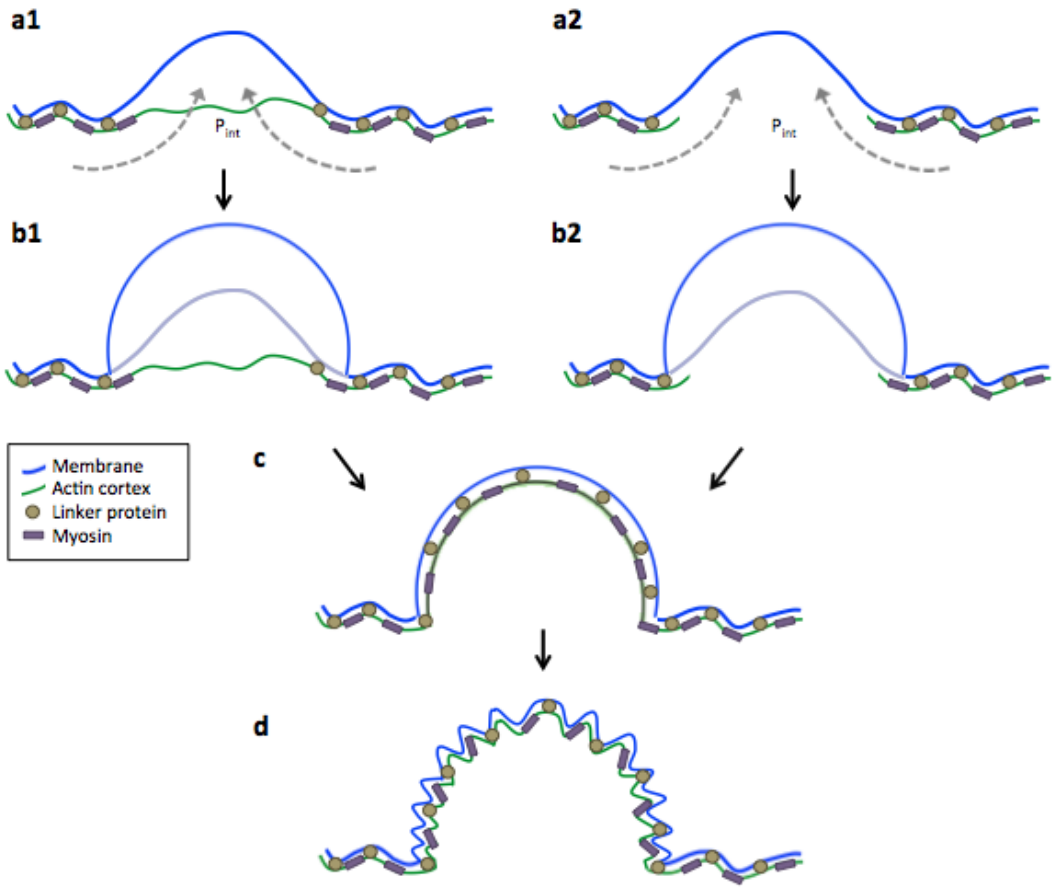

Figure 1.1: (a1) Bleb nucleation via detachment or breakage of linker proteins that adhere the membrane to the underlying cortex. Once a segment of membrane experiences local detachment from the cortex, the intracellular pressure pushes the detached section of membrane outwards. (a2) Alternatively, bleb nucleation can be a direct result of cortical rupture, where a lack of cortical strength or integrity causes tears in a small section of cortex. Since the membrane in this region will have nothing to be adhered to, intracellular pressure pushes it outwards as a bleb protrusion. Cortical rupture can be induced by laser ablation. (b1) Intracellular pressure causes continued growth of the bleb, whilst the old cortex remains visible as an 'F-actin scar.' (b2) Bleb expansion occurs, with no visible cortex remaining. (c) Actin polymerises under the blebbed membrane, forming a new cortex, and myosin-II is recruited. This stage is identical for both mechanisms of bleb nucleation, since by this point the intact cortex left behind in the case of the detachment mechanism has been fully degraded. (d) Bleb retraction through action of myosin-II motors on the new cortex. (Note that when blebs are employed as a migratory mechanism, the retraction stage of the bleb lifecycle is often not reached). Figure adapted from [Charras and Paluch, 2008].

1.1.3 A constructive role for blebbing: migration in 3D resistive environments

The most prevalent examples of blebbing motility observed can be subdivided into three categories: (i) blebbing motility during embryogenesis, (ii) amoeboid motility, and finally blebbing motility in tumour cells.

(i) blebbing motility during embryogenesis:
A large number of studies of cell migration in amphibian and fish embryos, observe blebbing to be a characteristic feature in early development [Trinkaus, 1973] [Holtfreter, 1943] [Wourms, 1972] [Holtfreter, 1946]. In particular, in zebrafish PGCs, tumbling cells migrate using blebs, with live imaging results demonstrating nucleation as a consequence of membrane-cortex detachment, rather than through cortical weakening. Alterations to the contractility of the acto-myosin cortex leading to abnormal PCG migration confirmed such protrusions to indeed be driven by intracellular hydrostatic pressure [Blaser et al., 2006]. Interestingly, a study by Diz-Munoz et al. demonstrated that blebbing can contribute to cell motility in functionally distinct ways; acting to either drive persistent migration (as is the case in PGCs) or as a stochastic way to explore the environment (as was observed in zebrafish mesendoderm cells) [Diz-Muñoz et al., 2016]. Fundulus deep cells from the killifish embryo have also been shown to use blebbing motility during embryogenesis, as well as to produce directed migration to sites of epithelial wounds in the yolk sac [Fink and Trinkaus, 1988]. Embryonic cell blebs often further elongate into cylindrical protrusions known as lobopodia [Holtfreter, 1946] [Yoshida and Inouye, 2001].

(ii) amoeboid motility
Blebbing motility is often referred to as amoeboid motility, since many amoeba migrate using spherical and tubular bleb or bleb-like protrusions [Mast, 1926] [Lämmermann and Sixt, 2009]. Expansion of the protrusions is due to cytoplasmic streaming, in a similarly intracellular pressure dependent manner as that of typical blebbing activity; where cytosol flows into weakened sections of the cell contour, where the membrane has detached from the cortex. Additionally such amoeboid protrusions are devoid of F-actin, but recover their association with actin upon retraction- similarly to blebs [Yanai et al., 1996] [Stockem et al., 1982] [Pomorski et al., 2007].

(iii) blebbing motility in tumour cells
Tumour cells have been shown to utilise blebbing as an invasive mode of migration

for pushing through dense tissue or extra cellular matrix (ECM) gels [Sahai and Marshall, 2003] [Pinner and Sahai, 2008]. Since this mode of migration does not require proteolytic degradation of the ECM, with protease inhibitors being a common target of tumour drug treatments, cells moving via the process of blebbing are unaffected and can continue to spread, and invade new tissues [Voura et al., 1998] [Wolf et al., 2003].

These examples highlight that blebbing motility is a common feature in many migratory processes, and may in some cases be the preferred method of cell migration. Indeed, experiments in *Dictyostelium* cells where blebbing is induced via migration underneath an agarose overlay, suggest that blebbing motility has an advantage over actin based protrusions for cells moving in mechanically resistive environments [Laevsky and Knecht, 2001] [Zatulovskiy et al., 2014]; perhaps due to the high protrusive thrust obtained through rapid expansion driven by intracellular pressure.

1.2 Motivation: How are bleb sites selected?

It is clear from the literature that many cells use blebbing motility, not only as a method of generating random protrusions, but also to generate persistent, directional movement. In order to migrate efficiently, cells must restrict blebbing activity to the leading edge. This raises the question of how bleb sites are selected, and polarised, and if blebs can be chemotactically oriented?

1.2.1 Possible mechanisms for directing blebs to the cell front

A variety of mechanisms can be envisioned to direct blebbing to the front of the cell: cortical weakening; global pressure gradients; and differences in membrane-cortex linker density. A schematic demonstrating how these three mechanisms could act is presented in figure 1.2

As discussed in section 1.1.2 a possible mechanism for bleb nucleation is that of weakening and subsequent rupture of the cortex. The clear difference in actin density between the front and rear of the cell has therefore been suggested to lead to increased blebbing at the front, giving a mechanism for bleb site selection [Ramalingam et al., 2015]. Since bleb formation via tears in the cortex are much less commonly observed than bleb formation due to membrane-cortex detachment, this is however unlikely to be a general mechanism for polarising bleb formation. In particular, in *Dictyostelium*

cells, blebs form without a loss of cortical integrity, as is evident by the presence of an intact F-actin scar [Langridge and Kay, 2006] left behind after the blebs forms.

Contraction of the cortex, producing a pressure surge might also promote blebbing. Myosin-II contractility is largely responsible for pressurizing the cytosol, and indeed, global blebbing propensity does depend on myosin-II activity, with both heavy and light chain myosin-II-null mutants being unable to bleb [Zatulovskiy et al., 2014]. Transient pressure gradients are possible thanks to the poroelastic nature of the cytoplasm, which consists of a porous actin meshwork through which viscous cytosol can flow [Maugis et al., 2010] [T. Mitchison, G. Charras, 2009]. The uropod is generally the most myosin-II-rich area of cells and is believed to be the most contractile. The high myosin-II contractility in the rear can induce global pressure gradients resulting in forward cytoplasmic streaming. If local pressure surges were to induce local blebbing, this would be predicted to occur in the rear of the cell, which is not observed, except in the case of Formin-A, mutants where the cortex of the uropod is weakened [Ramalingam et al., 2015].

The plasma membrane is attached to the underlying F-actin cortex by linker proteins, such as those carrying FERM domains, and there is evidence that asymmetric linker distributions can inhibit blebbing in the rear of the cell, and thus maintain cellular polarity [Diz-Munoz et al., 2010] . Round blebbing melanoma cells have a uropod like region, which is rich in the linker protein ezrin and where blebbing is significantly reduced, suggesting that ezrin hinders membrane detachment [Lorentzen et al., 2011]. In chemotaxing *Dictyostelium* cells, the linker protein Talin is enriched in the cell rear and Talin null mutants produce long trailing tails devoid of F-actin, indicating complete detachment of membrane and cortex [Tsujioka et al., 2012]. The localisations of ezrin and Talin were both shown to depend strongly on myosin-II activity, which is high in the rear of polarised migrating cells [Lorentzen et al., 2011] [Tsujioka et al., 2012]. In addition, a recent theoretical study aiming to model the migrational mode changes for cells moving through different matrix environments, found that in order to represent the experimentally observed dynamics, higher membrane to cortex linkage was required at the cell rear [Tozluoglu et al., 2015].

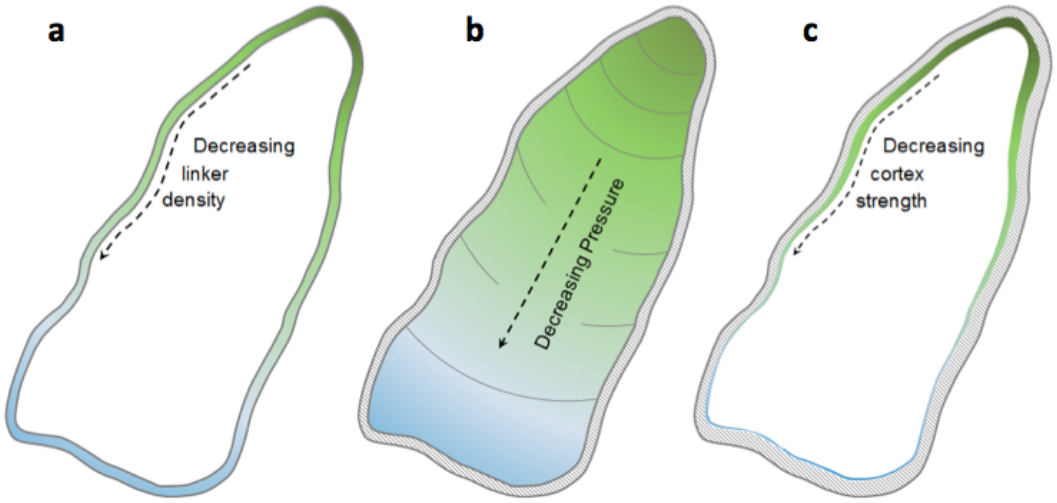

Figure 1.2: (a) An asymmetric gradient in the density of membrane to cortex adhesion proteins (linkers), where the linker density is higher in the cell rear has been observed in melanoma cells, and is a likely candidate for polarising bleb formation in *Dictyostelium* cells. (b) The existence of a long-range gradient in the intracellular hydrostatic pressure has been suggested a possible mechanism in facilitating bleb nucleation at the cell front as opposed to the rear in chemotaxing cells. Although myosin-II enrichment is indeed seen in the rear of polarised migrating cells, and myosin-II is largely responsible for pressurising the cell, the evidence on whether this would influence the local blebbing propensity in the desired manner is conflicting. (c) Differences in the cortical strength between the front and rear of migrating cells has been a popular suggestion in the literature as to how bleb site selection could be preferentially at the cell front, however, since in *Dictyostelium* cells, blebs form with an intact F-actin scar, as opposed to by cortical rupture, this is an unlikely candidate for polarising blebbing activity.

1.3 *Dictyostelium* as a model organism

Dictyostelium is a well established model organism, with the advantage of having many homologous genes to human cells, but with the simplicity of its genome allowing for easy genetic manipulation [Watts and Ashworth, 1970]. The lifecycle and rapid growth of the social amoeba *Dictyostelium* provide a platform for investigating cell processes such as cell differentiation, chemotaxis and apoptosis at both the single cellular and multi-cellular organism stages [King and Insall, 2009] [Chen et al., 1996]. *Dictyostelium* cells employ many of the same chemotactic mechanisms as other motile cells, including the activation of signal transduction pathways and the coordination of the cytoskeleton [Gerisch et al., 1995] [Gottwald et al., 1996] [Aizawa et al., 1997] [Parent et al., 1998].

Dictyostelium cells are also capable of using both actin driven and pressure-driven motility, with blebbing efficiently induced by mechanically resistive environments [Zatulovskiy et al., 2014] [Srivastava et al., 2017]. *Dictyostelium* cells chemotaxing to cyclic-AMP under an agarose overlay are observed to form polarised blebs up-gradient, and thus prove an ideal system for investigating bleb site selection.

1.3.1 Chemotaxis in *Dictyostelium*: directed cell migration

Chemotaxis is defined to be the process by which cells move along an extracellular gradient of diffusible chemicals. Not exclusive to *Dictyostelium*; chemotaxis was first observed in spermatozoa migration [Pfeffer, 1884], and soon after in leukocytes, where cells migrate along leukotrine gradients towards sites of inflammation [Leber, 1891]. Chemotaxis is also commonplace in many other motile eukaryotes. Until chemotaxis was extensively studied in bacteria however, relatively little was known about the sensory pathways and signal transduction machinery involved.

Dictyostelium cells respond to multiple chemoattractants (such as folic acid, lysophosphatidic acid and platelet activating factor), but the most well documented is of the response to cyclic adenosine monophosphate (cAMP) [Chen et al., 1996]. This response is highly dependent on the lifecycle stage of the *Dictyostelium*. Once *Dictyostelium* cells are deprived of their nutrient source, the cells secrete cAMP, which in turn promotes secretion of cAMP from neighbouring cells, and thus leads to cell aggregation and subsequent organisation into a multicellular slug [Bonner and Savage, 1947] [Konijn, 1972] [Gerisch, 1982].

In order for cells to chemotax, sensing of the environment and direction of the chemical gradient is required, which upon feedback must result in polarisation of the cell (establishing a distinct front and back) and subsequent movement.

Sensing of the environment

Chemotaxis in *Dictyostelium* is mediated by G-protein coupled receptors. G-proteins, or guanine nucleotide-binding proteins are a family of proteins, which through binding to either GTP (creating an active state) or to GDP (creating an inactive state), act as intracellular molecular switches. Interaction with surface receptors allow the G-proteins to participate in transmitting signals from extracellular stimuli into the cell.

Only four receptors exist that are known to have cAMP as the extracellular ligand; cAR1, cAR2, cAR3 and cAR4 (cAMP receptors 1,2,3,and 4 respectively). These receptors exhibit different affinities for cAMP, and are important in different stages of development [Kessin, 2001] [Louis et al., 1994] [Saxe et al., 1993] [Saxe III et al., 1996]. The cAR1 receptor is necessary during early development, and has been shown to be essential to aggregation [Parent and Devreotes, 1996]. cAR1 belongs to a class of seven-trans membrane domain receptors that can bind G-proteins. Interaction of trimeric G-proteins, consisting of α, β and γ subunits, with the cAR1 receptor results in a dissociation of the $\beta\gamma$ subunits from the α subunit. *Dictyostelium* cells devoid of either α subunit or $\beta\gamma$ heterodimer subunit, or cAR1 receptor, have been shown unable to respond to cAMP gradients [Kesbeke et al., 1988] [Wu et al., 1995] [Chen et al., 1996].

In order for cells to produce cAMP for aggregation, adenylyl cyclase must be activated by the cytosolic regulator of adenylyl cyclase (CRAC) [Insall et al., 1994]. The spatial distribution of CRAC in the presence of a chemotactic gradient in cAMP has been shown to be asymmetric, with enrichment at the cell front, whilst abolishing the gradient results in a homogeneous distribution around the cell membrane [Parent et al., 1998]. CRAC possesses a pleckstrin homology (PH) domain, which consists of a β sheet and a C-terminal α helix, and binds to membrane lipids such as phosphatidylinositol 3,4,5-triphosphate (PtdIns(3,4,5)P_3). Additionally, other PH domain containing proteins, also transiently associate with the membrane upon chemotactic stimulation, such as the Akt/PKB complex which acts as a signal transducer, whilst many PH domain proteins from the Rho family are responsible for actin remodelling [Meili et al., 1999]. Thus (PtdIns(3,4,5)P_3) is suggested to have a significant role in *Dictyostelium*

chemotaxis, mediating interactions for polarising the cell through selectively mobilizing the actin cytoskeleton machinery at the leading edge.

Translation of sensory information to movement: establishing cellular polarisation

Two classes of protein influence the metabolism of (PtdIns(3,4,5)P_3): type-1 phosphoinositide-3-kinases (P13Ks) and phosphatase and tensin homolog (PTEN). *Dictyostelium* possesses five types of P13Ks, which phosphorylate phosphatidylinositol 4,5-bisphosphate (PtdIns(4,5)P_2) to generate (PtdIns(3,4,5)P_3), whilst PTEN catalyses the dephosphorylation of (PtdIns(3,4,5)P_3) to (PtdIns(4,5)P_2) [Hoeller and Kay, 2007] [Funamoto et al., 2002]. Both P13Ks and PTEN act to amplify the metabolism of (PtdIns(3,4,5)P_3) in a directional manner, based on surface receptor signalling. Since the receptors on the cell membrane positioned further up gradient are activated slightly more frequently than those down gradient, a small asymmetric spatial distribution in the number of dissociated G-protein subunits results [Janetopoulos et al., 2001].

In the presence of a cAMP gradient, PI3Ks transiently localise up-gradient, at the front of the cell, whilst PTEN exhibits a complementary localisation pattern, dissociating from the leading edge but remaining membrane-bound at the cell rear. This results in an amplification of the spatial distribution of (PtdIns(3,4,5)P_3) in response to chemotactic gradient [Insall and Weiner, 2001]. The generally accepted mechanism for orchestrating the translocalisation of PI3Ks and PTEN is through a local-excitation, global-inhibition (LEGI) model, although there are numerous variations of the LEGI models presented in the literature. The overarching assumption of the models remains the same however- receptor occupancy prompts both a rapid local excitation and a slow global inhibition which collectively mediate the cellular response [Parent and Devreotes, 1999] [Levchenko and Iglesias, 2002]. For cells in a chemotactic gradient, the spatial gradient in receptor occupancy induces a stronger excitatory signal at the cell front. The inhibitory signal, although also higher at the cell front, spatially equilibrates via diffusion. Thus the net effect is of a stronger cellular response at the front (since excitation exceeds inhibition) than at the rear [Iglesias and Devreotes, 2008] [Xiong et al., 2010]. Such behaviour allow cells to translate a shallow external signal into a much steeper internal response.

1.3.2 Blebbing in *Dictyostelium*

Blebbing in *Dictyostelium* cells can be efficiently induced by increasing the mechanical resistance of their surrounding environment. Such environments can be imposed by forcing cells to chemotax through microchannels [Schuster et al., 2016] or by applying uniaxial pressure to them [Srivastava et al., 2017], or by forcing them to move underneath a thin agarose overlay. Srivastava et al. demonstrated that upon compression by a uniaxial load, myosin-II is rapidly recruited to the cortex, resulting in a loss of cellular polarisation, and quickly followed by cellular blebbing (within 30s). Under agar assays on the other hand were initially developed for mammalian cells [Nelson et al., 1975] and while mimicking some aspects of cell migration in complex 3D environments, such as the increased mechanical resistance, they have the advantage of optical simplicity. In addition, because the cells are flattened under agarose, the analysis of migration is easier allowing for analysis of protrusive behaviour to be restricted to two dimensions. Increasing the agarose concentration of the gel from 0.7% to 2% reliably increases the rate of blebbing in *Dictyostelium* cells, yielding a transition from mainly F-actin driven migration, to migration using blebs alone [Zatulovskiy et al., 2014]. Zatulovskiy et al. further demonstrated, through the tracking of fluorescent beads within the agar, that blebbing cells exert force on the surrounding gel, and must therefore experience mechanical resistance from it. It was also verified that blebbing induced through the under agarose assay was not due to the chemical composition of the overlay, cell flattening, the chemoattractant used or due to moving from one substrate to another.

Dictyostelium cells have been shown to be able to use blebbing motility to move directionally, in response to chemotactic gradients in cAMP and folic acid. Blebbing in a *Dictyostelium* cell chemotaxing under agarose to cAMP can be seen in figure 1.3, where the cell expresses an F-actin marker, ABD-GFP, and the agarose gel is stained with fluorescent RITC-dextran. The time series demonstrates the rapid expansion of blebs in *Dictyostelium* cells, whilst the cortical fluorescence of F-actin clearly shows that initial bleb expansion is devoid of F-actin.

1.3.3 Genetic control of blebbing

Much of the current understanding on the genetic regulation and control of blebs, in particular in *Dictyostelium*, has ben contributed by the Kay lab, who have performed perhaps the most exhaustive mutant screening analysis in relation to blebbing [Zatulovskiy et al., 2014].

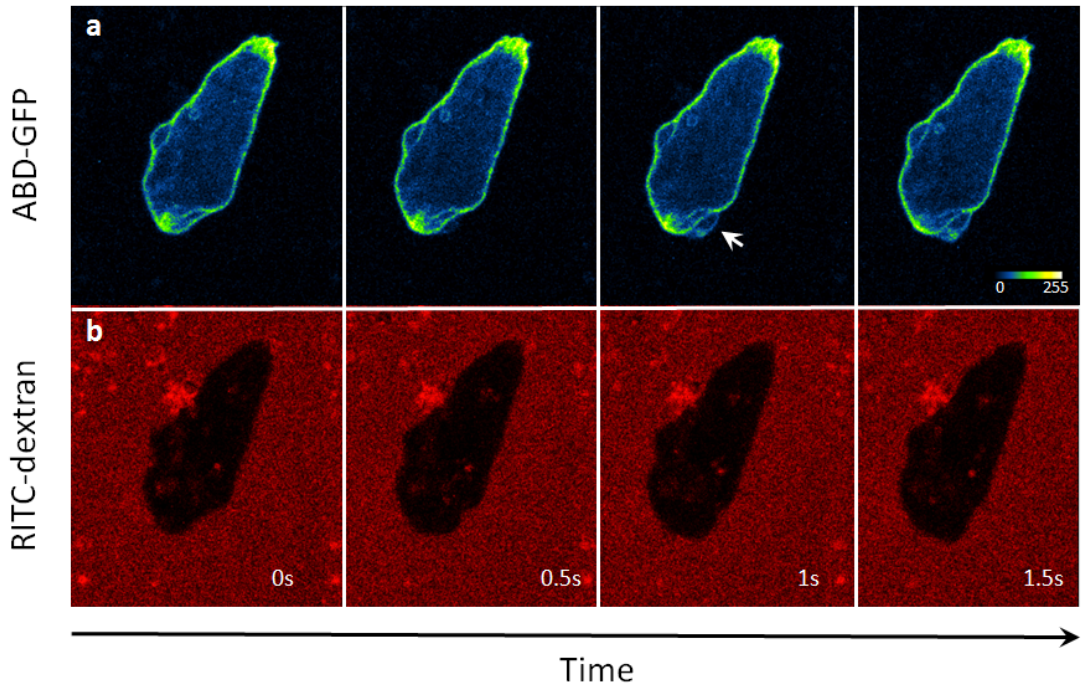

Figure 1.3: Bleb expansion in *Dictyostelium* cells is very rapid compared to mammalian cells. Here we observe a nucleation event (indicated by a white arrow) at $t = 0.5s$, with the bleb reaching its maximum expansion size by $t = 1.5s$. Cells express an F-actin marker, ABD-GFP (a) which clearly demonstrates where the cortex is left behind by the expanding membrane during bleb nucleation. Images are coloured according to ABD-GFP intensity. (b) The cell shown here is migrating underneath an agarose overlay (0.7% concentration) to promote blebbing, with the gel being fluorescently marked by RITC-dextran to act as a negative stain. Data collected by Evgeny Zatulovskiy.

Directional bleb formation up-gradient in response to a chemoattractant was shown to be a general principal; universally observed across a wide range of genetically distinct strains, including Ax2, NC4 and DdB. Such blebs were shown to coexist and interact with actin driven pseudopodia, with blebs even seen to occasionally transform into pseudopods, with continued polymerisation of the new cortex (this transitional state was referred to as 'blebbopodia'). Blebbing in *Dictyostelium* was also shown to have a strong dependence on developmental regulation, with blebs rarely observed in vegetative cells during random motility, but with the basal frequency increasing by nearly ten times within 8h of development. Once cells had started to form streams and aggregate, blebbing was seen to be the most commonly employed migrational mode.

The study by Zatulovskiy et al. aims to address the following overarching questions: How are blebs genetically controlled? (i.e. what factors influence global blebbing propensity?) and is blebbing dependent on chemotaxis sensory pathways?

Three assays were used to both qualitatively and quantitatively compare the impact of different mutations on blebbing (i) random motility of cells in buffer (to compare basal blebbing), (ii) migration under agarose (to assess the effect of mechanical resistance), and (iii) global stimulation by cAMP (to test ability of chemoattractant to induce blebbing- this is called the cyclic shock assay).

Recalling the mechanisms involved in each stage of the blebbing lifecycle, it is clear that the pre-requisites for bleb nucleation are: sufficient intracellular pressure to provide an outwards force on the cell membrane, and detachment of the membrane from the underlying cortex. Thus mutant studies for determining the genetic control of blebbing naturally fall into three categories: (i) genes affecting the hydrostatic pressure inside the cell, (ii) genes affecting the strength of membrane to cortex adhesion, and finally, (iii) genes influencing cortical stability.

Since myosin-II is largely responsible for pressurising the cell, it is fitting that both heavy and light chain myosin-II null mutants are unable to bleb in any of the three assays. The activity of myosin-II in chemotaxing *Dictyostelium* cells is partially dependent on cAMP signalling through downstream guanylyl-cyclases and cGMP-binding proteins, and disruption of this signalling pathway was therefore observed to significantly reduce blebbing.

Mutants lacking either membrane to cortex linker proteins Talin-A and Talin-B, or ponticulin exhibited a greatly increased blebbing phenotype. However, since Talin also plays a role in focal adhesion complexes, Talin null double mutant cells are poorly adhesive, and cannot penetrate under agar, they also detach during the cyclic shock assay, but bleb profusely in buffer. Ponticulin null cells are more adherent, and so can penetrate under agar, however the mutants only show a significant increase in blebbing frequency in the cyclic shock assay.

Mutations of actin binding proteins coronin (CorA) and the profilins (ProA and ProB), leading to the stabilization of F-actin or over-assembly of filaments, resulted in reduced blebbing activity. Conversely, mutants diminishing the polymerization of actin, mediated through the Arp2/3 actin nucleator complex, led to increased blebbing. Additionally, *Dictyostelium* cells with severely reduced levels of (PtdIns(4,5)P_2), a membrane lipid which binds numerous cortical proteins, were observed to have significantly higher blebbing frequencies in the buffer and cyclic shock assays, but again, cells seldomly managed to penetrate under agar.

These results are consistent with studies in mammalian cells, indicating an interplay between myosin-II based contractility of the cell, which facilitates blebbing, and actin polymerisation which resists it [Derivery et al., 2008] [Bergert et al., 2012] [Tozluoglu et al., 2013].

To address the question of whether bleb nucleation depends on chemotaxis sensory pathways, mutants deficient in cAMP receptors and associated G-proteins were investigated. Remarkably, many proteins deemed crucial to chemotaxis had no effect on bleb-driven motility. However, since the levels of (PtdIns(4,5)P_2) had already been seen to have an effect on blebbing activity, and the correct localisations of (PtdIns(4,5)P_2) and (PtdIns(3,4,5)P_3) are known to play an important role in chemotaxis, mutants of the metabolites of (PtdIns(3,4,5)P_3) were also examined. Knock-out cells for all five PI3Ks in *Dictyostelium* were found to be highly defective in terms of blebbing motility, although previous studies show that the same mutations have little effect on actin-based chemotaxis. Three PH domain containing proteins are downstream effectors for (PtdIns(3,4,5)P_3); Akt/PKB [Meili et al., 1999], CRAC [Insall et al., 1994] [Parent et al., 1998] and PhdA [Funamoto et al., 2002]. Mutants of the Akt/PKB complex were shown to have no effect on blebbing motility in response to a chemotactic gradient,

however, both CRAC and PhdA mutants exhibited a reduced blebbing response and deficiency in chemotactic movement. Blebbing was shown to be decreased in all three assays in CRAC null cells, but only in the cyclic shock assay for PhdA null cells. CRAC/PhdA double mutants were observed to have an even greater reduction in blebbing events than either single mutant. These results reveal a strong dependence on the activity of PI3Ks, and effectors of PIP3 levels, in bleb-driven motility in a chemotactic gradient, although the same results were not observed for actin-driven migration, suggesting that the two modes of motility are regulated via different sensory pathways.

It is also interesting to note that mutants with impaired blebbing ability were shown to move more slowly than wild-type cells under agar, whilst forming pseudopods rather than blebs. This again suggests that in some circumstance blebbing motility may indeed be the preferred migrational mode, providing advantages over the usual actin based pseudopodia movement.

1.4 Existing numerical models for blebbing

Mathematical models are employed to either determine mechanisms that give rise to experimentally observed phenomenon, or to generate predictions that lead to experimentally testable hypotheses, or a combination of the two. The majority of mathematical blebbing models presented in the literature focus on characterising different stages of the blebbing lifecycle, and mainly provide a framework to mimic experimental phenotypes.

Here we review pre-existing models in the literature which we categorise into focusing on either (i) bleb expansion, (ii) expansion and retraction (iii) nucleation or (iv) all stages of the blebbing lifecycle.

i) Numerous groups have modelled bleb expansion and growth, primarily as a means to probe the factors influencing the physical attributes of an expanding bleb.

Strychalski and Guy produced a 2D dynamic model, approximating the cell membrane and cortex as elastic; coupled together by linear springs representing the membrane-cortex adhesion molecules [Strychalski and Guy, 2011]. The cytosol was assumed to behave as a Newtonian fluid, but with the low Reynolds number meaning that the

governing fluid equations were given by the Stokes equations. Their model was used to investigate the effects of membrane and cortical elasticity on the shape and size of blebs. The effects of bulk cytosolic viscosity and cortical permeability on the timescale of bleb formation were explored, with the model identifying two distinct regimes, one where viscosity dominated the dynamics, and the other where drag or cortical permeability dominate. Upon investigating multi-blebbing however, their model was unable to reproduce the experimental result of secondary blebs being smaller than primary blebs, due to the pressure reduction resulting from bleb expansion being minimal.

Tinevez el al. combined their experimental work with modelling to study the correlation between cortical tension and bleb expansion [Tinevez et al., 2009]. Blebbing on cells of different tensions was induced in a controlled way via laser ablation, leading to the identification of a threshold value of surface tension, below which no blebs were able to nucleate. The maximal size of blebs above this threshold value were shown to depend strongly on tension, and this dependence could be reproduced via modelling the cell membrane and cortex as elastic surfaces, with the cytosol approximated as a compressible liquid-gel. The model utilized a simplified spherical geometry, and the intracellular pressure was assumed to be uniform. Although Tinevez et al. did not model bleb retraction, their experimental results showed that the characteristic time of bleb arrest did not depend on tension, and thus proposed a tension-independent mechanism such as actin repolymerisation at the blebbed membrane could be responsible for ceasing bleb expansion.

An elastic shell model, whereby the membrane and cortex were modelled together as a compound elastic material, rather than as separate entities was presented by Woolley et al. [Woolley et al., 2014]. In the simplest form of the model, blebs were formed by stretching the shell, which often violated the 4% maximal membrane stretch criteria shown to hold experimentally [Cunningham, 1995] [Tinevez et al., 2009]. Two further extensions of this model were presented in the same paper, with the second version of the model allowing the shell to grow as well as stretch, since the rapid expansion of blebs suggests the need for an additional mechanism that acts to increase the amount of available membrane. Although various mechanisms to produce extra membrane have been proposed in the literature (such as membrane unfolding or vesicles fusing with the bleb), the model was not used to explore these, simply allowing membrane in the blebbed region to increase, regardless of particular mechanism. The third version of the model fixed both the shape of the cell body and the bleb to be spherical. The

bending energy of the system was shown to be small, only becoming important in areas of strong curvature, such as the bleb neck, thus justifying the use of spherical cell and bleb geometries. Results for the pressure reduction upon bleb expansion, and final bleb size and shape were shown to be comparable across all three models. The spherical model was also used to investigate multi-blebbing; either through inducing blebbing at opposite ends of the cell body, or by inducing a bleb on top of the first bleb; and was able to reproduce the experimental result of secondary blebs being smaller. For blebs nucleating on opposite sides, the second bleb was shown to take significantly longer to form, even though its final size was smaller. In the case of a bleb forming on top of a pre-existing bleb, the second bleb was shown to be unable to grow as wide as the secondary bleb in the previous case, although all other parameters were identical.

A further model for bleb expansion was later produced by Woolley et al, this time considering the membrane and cortex separately, approximated by elastic elements, and connected by linker springs [Woolley et al., 2015]. The cytosol was not modelled, and the cortex was assumed to be static on the timescales considered. The model was used to investigate what mechanisms could be responsible for producing the small-necked blebs experimentally observed in muscle cells, where the neck diameter of the bleb was significantly smaller than its maximal width. The existence of such small-necked blebs poses an interesting modelling question of how to prevent rapid membrane peeling at the neck, in order to maintain the high curvature in this region. Two mechanisms were found that could produce blebs of the desired size, global contraction of the cortex and localized growth of membrane across the blebbing region. Interestingly, a third mechanism was also identified, showing that small-necked blebs could be produced if the neck regions of the bleb had increased membrane-cortex adhesion strength, however, this was dismissed by the authors as being non-biological. All of the models discussed in this section use simplified cell geometries, either circular or spherical, and artificially induce bleb nucleation by ablation of either cortex or linkers.

ii) Models including cortical dynamics have been developed to enable simulations of bleb retraction as well as expansion.

Young et al. presented a 2D model, comparable with that of Strychalski and Guy, approximating the membrane as a 1D elastic curve, and modelling the cytosol as an incompressible fluid governed by the Stokes equations [Young and Mitran, 2010]. The average effect of the cytoskeleton was included via filament forces imposed on

the membrane. Since the build up of a new cortex at the blebbed membrane, and subsequent activation of myosin-II motors is required to retract a bleb, the diffusion and advection of actin and myosin monomers into the bleb was encompassed by the model, with a transition term accounting for monomer to polymer transitions and vice-versa. The motion of the plasma membrane was modelled using a damped wave equation, with forces from fluid pressure, viscosity, and filaments as source terms. In order for bleb protrusions to maintain the 4% maximal membrane stretching criteria, a membrane unfolding mechanism was assumed, thus allowing large membrane displacements for relatively small strains. The model was able to produce geometrically realistic non-spherical protrusions and retractions.

Lim et al. developed a model to investigate travelling blebs, in addition to expansion and retraction of single blebs. Both membrane and cortex were modelled as elastic sheets, coupled together via adhesion springs, and with the cytosol as a Newtonian fluid [Lim et al., 2012]. A healing term was included, accounting for polymerisation of actin at the bleb, which allowed for reattachment of the cell membrane. Instead of the commonly assumed uniform hydrostatic pressure, the pressure term was coupled to local cortical contraction and healing, and set to be a travelling pulse, thus allowing for inhomogeneous pressure across the cell. The authors showed that asymmetric healing of the cortex could result in travelling blebs, which have been observed experimentally, and are referred to as 'circus movement' [Charras et al., 2008]. Again, both of these models artificially induced bleb nucleation by ablation of either cortex or linkers, and utilized a circular initial cell geometry.

iii) Relatively few models in the literature focus on bleb nucleation, instead usually artificially inducing blebbing, and then focusing on the later stages of the blebbing lifecycle.

A 3D coarse-grained spherical model was developed by Spangler et al., where the actin cortex was modelled as a triangulated mesh of elastic elements, coupled at the vertices to the lipid membrane via linear springs [Spangler et al., 2011]. The membrane was composed of a double layer of particles with two semi-flexible tails, with a positive tail-tail interaction term, thereby enabling self-assembly of the bilayer, although spontaneous curvature of the system was omitted. A repulsive potential between the lipid and cytoskeleton particles was assumed. The total interaction potential of the system included two-body interactions between particles, harmonic interactions for lipid

bonds and cytoskeletal elements, and three-body interactions accounting for bending rigidities of lipids and cortex. Movement of the lipid particles is then governed by molecular dynamics using a Langevin thermostat. Evolution of the system showed that bleb nucleation was energetically favourable for large values of ratio of areas between membrane and cortex i.e. suggesting a critical extension of linkers exists. The model also showed, in agreement with experiments and other modelling approaches, that bleb nucleation could be induced by ablation of the cortex locally, or interestingly, through a uniform contraction of the whole cortex.

Alert et al. produced an in depth study of bleb nucleation investigating the influence of membrane peeling [Alert and Casademunt, 2016]. The membrane was modelled as an elastic material, anchored to a static cortex via linker springs. Linkers in this model were allowed to attach as well as detach, such that areas of separated membrane could heal. The attachment rate of linkers was assumed to be constant, whilst the detachment rate was set to be force-dependent. The equations predicted the existence of a critical pressure, above which a membrane-cortex unbinding transition occurs. The model suggests that there is an energy barrier to bleb nucleation, and as such, a critical size of detached membrane is necessary to grow the patch further to become a bleb, whilst patches less than the critical radius can heal. (This is an advancement on earlier work by Charras et al. using classical nucleation theory to identify a critical bleb radius [Charras et al., 2008]). Investigating the peeling speed of stretched linkers on the edge of a patch identified that peeling only occurs if the linker length at the contact line exceeds the critical value, else the patch heals by adhesion. Interestingly, this study showed that, in contrast to classical nucleation theory, membrane peeling is not controlled by the energy cost of bleb formation, but rather entirely by linker kinetics. The authors also considered stochastic effects in order to investigate the statistics of bleb nucleation times. Thermal and chemical fluctuations of linkers were included in the model to promote bleb nucleation, and membrane undulations were considered at a linear level. The emergent probability distribution of bleb nucleation times was shown to feature an exponential tail, thus indicating the dominance of a single timescale. In both the deterministic and stochastic cases, an initially nearly flat membrane was used in the model, as opposed to a closed curve.

iv) The most complete blebbing model to date is that of Tozluoglu et al., where the full blebbing lifecycle is dynamically modelled; from nucleation to retraction [Tozluolu et al., 2013] [Tozluoglu et al., 2015]. The cell membrane is modelled as

elastic elements, whilst the cortex is modelled by viscoelastic elements (i.e. each discrete element is represented by a spring and dashpot in series). Contractility of the cortex is controlled via additional parallel myosin springs. The model was to visualize overall cell paths in different types of external environment, as a means to investigate the relationship between bleb driven motility and confined or resistive environments. Both experimental data and the model demonstrated that with increased confinement, increased cortical contractility yields increased cell velocities. In particular, bleb-based motility was found to dominate in confined, discontinuous ECM geometries. Although the focus of the work was not on bleb polarisation, a higher cortex-membrane linkage at the rear of the cell was found to be favourable in modelling migration in confined environments.

1.5 The role of membrane tension

Previously, blebbing in *Dictyostelium* was found to have a strong dependence on membrane geometry, with blebs being shown to preferentially nucleate from concave regions on the cell contour. Since the extension of pseudopods generates regions of negative curvature on either side of the actin based protrusion, it was suggested that this could be the mechanism through which blebs are polarised. Pseudopods are chemotactically oriented and tightly localized to the leading edge (up-gradient), with a narrow angular distribution; while blebs were shown to have a bimodal distribution, forming on either side of pseudopods from the highly concave regions on their flanks. It was therefore hypothesised that blebs and pseudopods effectively cooperate to cluster protrusions to the cell front [Tyson et al., 2014].

The resultant vector force due to membrane tension changes direction with position around the cell contour, dependent on local curvature. In concave regions, membrane tension provides an outwards force, which acts to facilitate detachment of the membrane from the cortex, contrary to convex regions where membrane tension pulls the membrane towards the cortex. This idea forms the basis for the conceptual model developed by Tyson et al. to illustrate how blebs could preferentially nucleate from areas of negative curvature (figure 1.4). The model is unique in the sense that it is the first to propose that the mechanism through which blebs are polarised is purely based on physical forces, not on biological regulation.

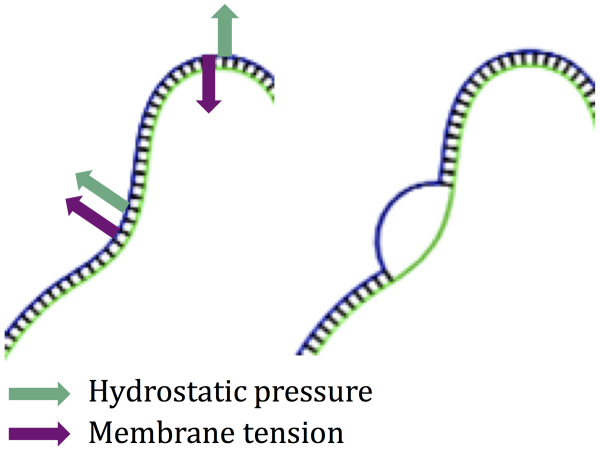

Figure 1.4: Idealised cell contour used by Tyson et al. to demonstrate how physical mechanisms alone could lead to protrusion clustering at the cell front, with blebs preferentially nucleating at the negatively curved flanks of pseudopods. Whilst the directions of the intracellular pressure and linker forces are fixed, the resultant force of the membrane tension changes sign dependent on local curvature, acting outwards in regions of negative curvature, thus facilitating membrane detachment and bleb nucleation in these regions.

1.5.1 A biophysical model for curvature dependent bleb nucleation

Here we present the framework for the original model by Tyson et al. to suggest how blebs and pseudopods cooperate through membrane tension to cluster protrusions to the cell front.

System description

We consider a 2D cross section of a cell, with the plasma membrane and cell cortex both approximated by closed contours consisting of a number of discrete nodes, which are connected by linear edges, assumed to act as springs in series. Corresponding nodes on the membrane and cortex are coupled by cortex to membrane linkers, acting as linear springs in parallel.

Intracellular pressure, acting on the membrane but not the porous cortex, is the main driver of blebbing. It puts linkers under strain, causing them to break beyond a critical extension, and allowing the detached membrane to form a bleb.

In *Dictyostelium* cells, bleb nucleation and expansion are very fast ($<$ 0.1 s) compared to cortex remodelling [Zatulovskiy et al., 2014], which is why we treat the cortex as fixed on the timescale of blebbing, similarly to the models presented by [Woolley et al., 2015] and [Alert et al., 2015].

Assuming the Helfrich model for membrane bending [Helfrich, 1973], the total membrane elastic energy integrated over the normalised contour length is given by,

$$E_{elastic} = \oint_0^1 (E_{tension} + E_{bending} + E_{coupling}) ds \tag{1.1}$$

where we integrate over the normalised contour length, which is parameterised in terms of fractional length along the contour, s.

The time dependence in the model comes from the inclusion of a viscous drag experienced by a bleb as it expands.

In the subsequent chapter, we derive the continuous form of each of the contributing energy terms appearing in the above integral, before determining the variational form of the energy necessary to solve the time dependent PDE, and finally writing this in the finite difference scheme used computationally.

1.6 Project aims

The current evidence on mechanisms of bleb site selection, with bleb formation polarised to the cell front is still an incomplete picture. Experimental studies show strong promise for asymmetric distributions in membrane to cortex linkage strength leading to directional blebbing. Nevertheless, in *Dictyostelium* cells experiments investigating the localisation of the membrane to cortex linker protein, TalinA, have only been carried out on cells in buffer or in slug aggregates; no quantitative blebbing assays linking Talin activity to local or global blebbing activity have been recorded. Some models in the literature have hinted at the necessity of an asymmetry in membrane-cortex adhesion strength to produce polarised blebbing, but with no direct link to quantitative experimental data. The model by Tyson et al. suggests the mechanism for bleb polarisation could be based entirely on physical forces, as opposed to biological control. However, as yet no direct link between experimental and modelling frameworks aiming to predict

the individual sites of bleb nucleation currently exists; thus the question of how blebs are chemotactically oriented remains largely open. In order to investigate this, we build upon the modelling work by Tyson et al. (and utilise the ABD-GFP cell data collected by Evgeny Zatulovskiy, in addition to generating our own image data) and aim to:

(i) **Develop a quantitative method to predict the sites of bleb nucleation in *Dictyostelium* cells chemotaxing in mechanically resistive environments, in which we:**

- Aim to use real cell contours extracted from confocal microscopy image data to initialise the Tyson model.

- Aim to measure the spatial distribution of experimental bleb sites, and quantitatively compare this to the spatial distribution of bleb sites predicted by the model.

This novel image based modelling approach will allow us to link experimental and modelling data on bleb polarisation for the first time.

(ii) **Determine to what extent cell geometry alone is sufficient to direct blebs to the cell front.**

We will probe the capability of physical forces, specifically due to cellular geometry, to polarise bleb formation, through analysing the spatial localisation of bleb sites predicted by the model, and how well these correspond to what is experimentally observed. We will investigate whether the spatial distribution of predicted bleb sites is impacted by the degree of mechanical resistance experienced by the *Dictyostelium* cells, by investigating the results for low and high resistive environments, imposed by overlays of 0.7% and 2% agarose gels respectively.

(iii) **For the proportion of bleb sites not explained by cellular geometry, we will further investigate the biological mechanisms which may influence bleb formation for cells in mechanically resistive environments.**

We will create fluorescently tagged constructs of the membrane to cortex linker protein TalinA, which we will use to generate high quality image data on the localisation of the linker, in chemotaxing *Dictyostelium* cells experiencing

mechanical resistance.

We will quantitatively analyse the fluorescent intensity profile of TalinA localisation, and aim to incorporate the results into an updated version of the model.

Chapter 2

Theoretical methods

2.1 Derivation of model equations: Overview

In this chapter we derive from first principles the governing model equations for evolution of the cell membrane over time, with force contributions from membrane tension, membrane bending, coupling to the actin cortex and intracellular hydrostatic pressure.

We additionally perform dimensional analysis on each of the terms in the resulting membrane evolution PDE, demonstrating that each is indeed consistent with a velocity.

2.2 Model framework

We use confocal microscopy image data of cells chemotaxing under agarose to initialise the model geometry (for method details see section 2.10), thus our analysis is based on cellular cross sections.

We approximate both the plasma membrane and the actin cortex by closed contours consisting of a number of discrete nodes, which are connected by linear edges, assumed to act as springs in series. The cortex is assumed to remain stationary on the time-scale of bleb nucleation, and thus in our model, the cortical nodes simply define the anchorage points for membrane nodes. Corresponding nodes on the membrane and cell cortex are coupled by cortex to membrane linkers, acting as linear springs in parallel. A critical extension is defined for such linker springs, beyond which they will

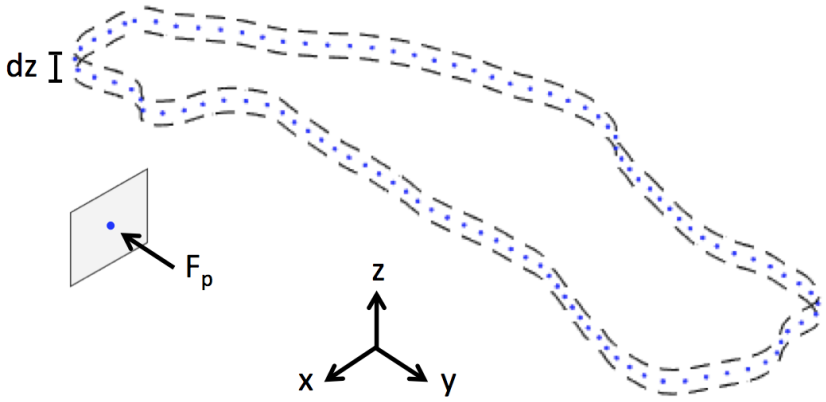

Figure 2.1: We solve the force balance PDE for membrane evolution on a thin cross sectional slice of height dz. Since the curvature differences along the z-direction are negligible, with our system being geometrically similar to a cylinder, the z-component of all forces acting on the membrane is assumed to be $= 0$. We make use of such a 3D system, although our forces reduce to a 2D approximation, since this enables us to use a physically meaningful pressure force, with the pressure parameter in units of Pa. The pressure force, F_p acts on a perpendicular area element $d\tilde{s} \cdot dz$, where $d\tilde{s}$ is the distance between nodes, and dz is of the order $d\tilde{s}$.

break, allowing the cell membrane to detach from the underlying cortex.

We assume the membrane and cortex nodes are described on a thin cellular cross section of height dz (figure 2.1). Since the cells under agarose are very flat, with negligible curvature variations in the z-direction, we assume the z-components of the forces acting on the cell membrane are 0. All forces act in the $x - y$ plane only, so our analysis on a thin strip is reduced to a 2D approximation. Critically, however, performing our analysis on a thin cross section allows us to use a physically meaningful pressure parameter with dimensions of Pa, or Nm^{-2}. (The 2D analogue of this would be to define a pressure parameter P_{2D}, with units of Nm^{-1}, which although mathematically valid, is difficult to compare to experimentally discussed values quoted in Pa.)

2.3 Notation

Here we introduce the vector notation used in the subsequent derivations.

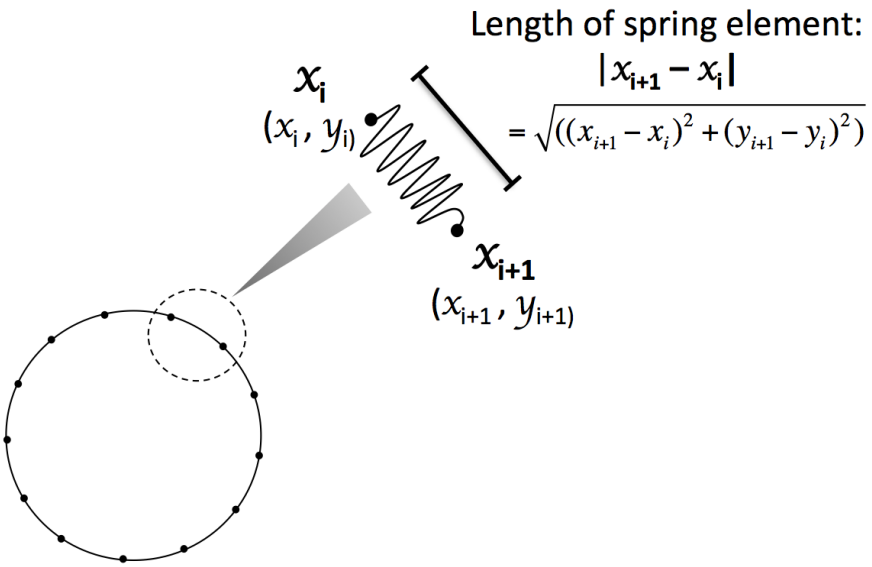

Figure 2.2: The model membrane is approximated by a closed contour of discrete nodes, connected by linear springs. The position of the ith node is expressed as $\mathbf{x}_i = (x_i, y_i)$, with nodes labelled from 1 to N clockwise around the contour. The length of the ith spring element is given by the magnitude of the vector difference between the node positions at each end of the spring.

Let $\mathbf{x} = (x, y)$ in cartesian coordinates, such that for a system consisting of N discrete nodes, the position of the ith node can be expressed as follows,

$$\mathbf{x}_i = (x_i, y_i) \tag{2.1}$$

The magnitude of the displacement, due to extension or compression, of a membrane spring element can thus be described by the euclidean distance of the difference between the positions of the two discrete nodes at each end of the spring, as demonstrated in figure 2.2.

We later reparameterise our equations in terms of the curvilinear coordinate along the curve, s, such that each discrete node can be described by s_i where the index $i = [1 : N]$, and therefore $\mathbf{x}(s_i) = \mathbf{x}_i$.

To write the final form of the discrete PDE for membrane evolution, we further condense our equations making use of the following, $\mathbf{x} = (x, y) = (x^0, x^1)$, such that both x and y components of the PDE can be expressed through the term x^j for

$j = [0, 1]$.

$$\mathbf{x}^j(s_i) = \begin{cases} x(s_i), & \text{for } j = 0 \\ y(s_i), & \text{for } j = 1 \end{cases}$$

2.4 Functional form of the total membrane energy

2.4.1 Membrane tension energy

Let the total elastic tension energy of N springs of equal length, connected in series to form a close curve, of length L be described by Hooke's law,

$$E = \frac{1}{2}kL^2 \tag{2.2}$$

Then we may rewrite this in terms of N as follows,

$$\begin{aligned} E &= \frac{1}{2}N^2k(\frac{L}{N})^2 \\ &= \frac{1}{2}\sum_{1}^{N} Nk\Big(|\Delta\mathbf{x}|\Big)^2 \end{aligned} \tag{2.3}$$

where we define $\Delta\mathbf{x} = L/N$

Now let us express E in terms of the fractional length or curvilinear coordinate along the contour, Δs, with

$$N = \frac{1}{\Delta s} \tag{2.4}$$

Thus giving,

$$
\begin{aligned}
E &= \frac{1}{2}\sum_{1}^{N}\frac{1}{\Delta s}k(|\Delta \mathbf{x}|)^2 \\
&= \frac{1}{2}\sum_{1}^{N}\frac{1}{\Delta s}\cdot\frac{\Delta s}{\Delta s}k(|\Delta \mathbf{x}|)^2 \\
&= \frac{1}{2}\sum_{1}^{N}k\left(\left|\frac{\Delta \mathbf{x}}{\Delta s}\right|\right)^2\Delta s
\end{aligned}
\tag{2.5}
$$

which for $\Delta s \to 0$ becomes,

$$
E = \frac{1}{2}\oint_0^1 k\left(\left|\frac{d\mathbf{x}}{ds}\right|\right)^2 ds \tag{2.6}
$$

This is the form of the tension energy if we neglect the resting length of the curve.

2.4.2 Membrane bending energy

The bending energy is given by,

$$
E_{bending} = \frac{1}{2}\oint_0^L \tilde{k_b}\left(\frac{1}{R_c}\right)^2 d\tilde{s} \tag{2.7}
$$

as is standard convention, where R_c is the radius of curvature, $\tilde{k_b}$ is the bending modulus (SI units Nm^2), and $\tilde{s}$ is the arc length (SI units m).

Recall that,

$$
\kappa = \frac{1}{R_c} \tag{2.8}
$$

with curvature, κ defined as

$$
\kappa = \left|\frac{d\mathbf{T}}{d\tilde{s}}\right| \tag{2.9}
$$

where $T(\tilde{s})$ is the unit tangent vector. For a curve, c, if $\boldsymbol{\gamma}(\tilde{s})$ is the arc length parameterisation of c, then the unit tangent vector $\mathbf{T}(\tilde{s})$ is given by, $\mathbf{T}(\tilde{s}) = \boldsymbol{\gamma}'(\tilde{s})$, therefore the curvature can be written as,

$$\kappa = |\mathbf{T}'(\tilde{s})| = |\boldsymbol{\gamma}''(\tilde{s})| = \left|\frac{d^2\tilde{\mathbf{x}}}{d\tilde{s}^2}\right| \tag{2.10}$$

where $\tilde{\boldsymbol{x}} = \boldsymbol{x}(\tilde{s})$ is the arc length parameterisation of $\boldsymbol{x}$.

To check for dimensional consistency, the dimensions of curvature as determined by equation 2.8 are of inverse length, and the dimensions of curvature as determined by equation 2.10 are m/m^2 and thus also of inverse length.

Thus equation 2.7 can be equivalently expressed as,

$$E_{bending} = \frac{1}{2}\oint_0^L \tilde{k_b}\left(\left|\frac{d^2\tilde{\mathbf{x}}}{d\tilde{s}^2}\right|\right)^2 d\tilde{s} \tag{2.11}$$

We now wish to rewrite equation 2.11 in terms of the dimensionless parameter, s, (normalised arc length), and thus proceed as follows,

$$\begin{aligned} s &= \frac{\tilde{s}}{L} \\ d\tilde{s} &= L ds \\ \frac{d}{d\tilde{s}} &= \frac{d}{L ds} \end{aligned} \tag{2.12}$$

$$\begin{aligned} E_{bending} &= \frac{1}{2}\oint_0^1 \tilde{k_b}\left(\left|\frac{d^2\mathbf{x}}{L^2 ds^2}\right|\right)^2 L ds \\ &= \frac{1}{2}\oint_0^1 \frac{\tilde{k_b}}{L^3}\left(\left|\frac{d^2\mathbf{x}}{ds^2}\right|\right)^2 ds \end{aligned} \tag{2.13}$$

$$E_{bending} = \frac{1}{2}\oint_0^1 k_b\left(\left|\frac{d^2\mathbf{x}}{ds^2}\right|\right)^2 ds \tag{2.14}$$

where $k_b = \tilde{k_b}/L^3$ (SI units Nm^{-1})

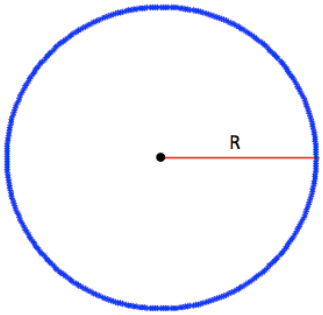

Figure 2.3: We apply the three equations for curvature, based on different parameterisations to a circle of radius R to check for numerical consistency.

2.4.3 Test simulation for equivalence of curvature output for different parameterisations

Here we run a simulation on a circle of radius R (figure 2.3), computing the curvature as (i) $1/R$, (ii) $|d^2\tilde{\mathbf{x}}/d\tilde{s}^2|$, where $d\tilde{s}$ is the distance between nodes and (iii) $|d^2\mathbf{x}/L^2ds^2|$, where $ds = 1/X$ is the dimensionless node spacing.

```
N = 360;
X = N-1; %number of nodes
l = [X,1:X-1]; r = [2:X,1]; %left and right indexing vectors
phi = linspace(0,2*pi,N);
phi(end) = []; %since closed curve
R = 5; %Define radius
x = R*cos(phi);
y = R*sin(phi);
%Method 1: compute curvature as 1/R
Curv_1 = 1/R;

%Method 2: compute curvature with s being arc length
per = sqrt( (x-x(r)).^2 + (y-y(r)).^2 ); %distance between
    adjacent nodes
arclength = sum(per);
avSpacing = mean(per);
ds2 = avSpacing^2; %actual distance between nodes
Second_x = (x(l) - 2*x + x(r))/ds2;
Second_y = (y(l) - 2*y + y(r))/ds2;
```

```
Curv_2 = mean(sqrt(Second_x.^2+Second_y.^2));

%Method 3: compute curvature with s being dimensionless
ds = 1/X;
ds2 = ds*ds;
Second_x = (x(l) - 2*x + x(r))/ds2;
Second_y = (y(l) - 2*y + y(r))/ds2;
Curv_3 = (1/arc length^2)*mean(sqrt(Second_x.^2+Second_y.^2));

display(sprintf('Radius input: %d',R));
display(sprintf('Curvature (1/R): %f',Curv_1));
display(sprintf('Curvature for ds is actual distance: %f',
    Curv_2));
display(sprintf('Curvature for ds is dimensionless: %f',Curv_3)
    );
```

```
Simulation Output
>> CurvatureCheck
Radius: 5
Curvature (1/R): 0.200000
Curvature using ds as actual distance: 0.200000
Curvature using ds as dimensionless: 0.200000
```

2.4.4 Membrane tension energy (including resting length)

We now return to the tension energy for the system, but include an associated resting length of the contour, x_0, such that the total contour length cannot compress to a length $L < x_0$. Following the same reasoning as previously, we have:

$$
\begin{aligned}
E_{tension} &= \frac{1}{2}N^2 k_t \frac{(L-x_0)^2}{N^2} \\
&= \frac{1}{2}N^2 k_t \left(|\Delta\mathbf{x}| - \frac{x_0}{N}\right)^2 \\
&= \frac{1}{2}\sum_1^N N k_t \left(|\Delta\mathbf{x}| - \frac{x_0}{N}\right)^2 \\
&= \frac{1}{2}\sum_1^N \frac{1}{\Delta s}\cdot\frac{\Delta s}{\Delta s} k_t \left(|\Delta\mathbf{x}| - \frac{x_0}{N}\right)^2 \\
&= \frac{1}{2}\sum_1^N k_t \left(\frac{|\Delta\mathbf{x}|}{\Delta s} - \frac{x_0}{N\Delta s}\right)^2 \Delta s \\
&= \frac{1}{2}\sum_1^N k_t \left(\frac{|\Delta\mathbf{x}|}{\Delta s} - x_0\right)^2 \Delta s
\end{aligned}
\tag{2.15}
$$

which for $\Delta s \to 0$ becomes,

$$
E_{tension} = \frac{1}{2}\oint_0^1 k_t \left(\left|\frac{d\mathbf{x}}{ds}\right| - x_0\right)^2 ds \tag{2.16}
$$

2.4.5 Coupling energy

We describe the coupling energy due to the elastic linkers that tether the membrane to the cortex in the following way,

$$
E_{coupling} = \frac{1}{2}k_c(|\mathbf{x} - \mathbf{x_c}| - l_0)^2 \tag{2.17}
$$

where $\mathbf{x}$ is the position vector for the membrane, and $\mathbf{x_c}$ for the cortex. l_0 is the resting length of the linkers.

Since the linker springs are connected in parallel to each other, joining each membrane and cortex node pair around the cell contour, we may immediately express the total coupling energy due to N linkers as the sum of spring energies from each individual element. In the limit that the fractional contour length tends to zero, this is expressed in the continuous form as follows,

$$
E_{coupling} = \frac{1}{2}\oint_0^1 k_c(|\mathbf{x} - \mathbf{x_c}| - l_0)^2 ds \tag{2.18}
$$

thus the total elastic energy of the membrane is given by,

$$\begin{aligned} E_{elastic} &= E_{tension} + E_{bending} + E_{coupling} \\ &= \oint_0^1 \left[\frac{k_t}{2} \left(\left| \frac{d\mathbf{x}}{ds} \right| - x_0 \right)^2 + \frac{k_b}{2} \left(\left| \frac{d^2\mathbf{x}}{ds^2} \right| \right)^2 + \frac{k_c}{2} (|\mathbf{x} - \mathbf{x_c}| - l_0)^2 \right] ds \end{aligned} \tag{2.19}$$

2.5 PDE for membrane displacement

We have now considered the internal sources of elastic forces acting on the plasma membrane; membrane elasticity (tension and bending), and coupling to the cortex (figure 2.4). We also know that the intracellular pressure will exert force on the membrane, putting the linkers under strain. However, the cell membrane will additionally experience the effects of the cell's external environment. The viscous fluid surrounding the cell imposes a drag force on the membrane when it is displaced. Since our model aims to describe blebbing, we assume that the only large-scale membrane displacements to evolve will be that of spherical bleb protrusions, and thus approximate the viscous force to be the Stoke's drag force on a sphere, given by,

$$\begin{aligned} F_{viscous} &= 6\pi\eta R \frac{\partial}{\partial t}\mathbf{x} \\ &= \omega \frac{\partial}{\partial t}\mathbf{x} \end{aligned} \tag{2.20}$$

where η is the dynamic viscosity of the surrounding fluid, and R is the radius of the bleb.

We assume that the cell membrane obeys force balance such that

$$\begin{aligned} 0 &= F_{tension} + F_{bending} + F_{coupling} + F_{pressure} + F_{viscous} \\ 0 &= F_{elastic} + F_{pressure} + F_{viscous} \\ F_{viscous} &= -F_{elastic} - F_{pressure} \\ F_{viscous} &= -\partial E_{elastic} - F_{pressure} \end{aligned} \tag{2.21}$$

Combining equations 2.20 and 2.21, yields the pde for membrane displacement, which we wish to numerically solve to investigate the geometric dependence of bleb nucleation,

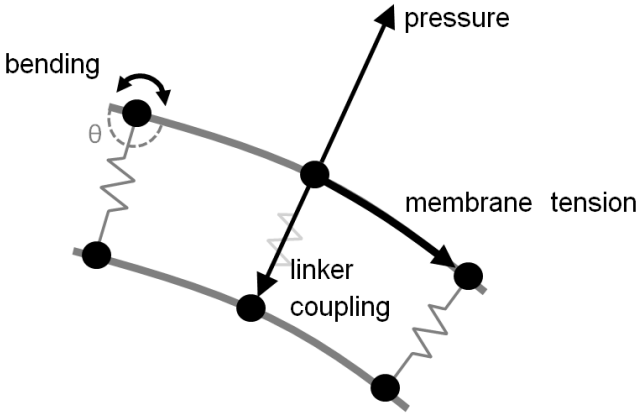

Figure 2.4: Schematic of forces acting on membrane nodes, with contributions from membrane bending, membrane tension, intracellular hydrostatic pressure and coupling via linkage to the cortex. Membrane nodes are adhered to the cortex via linkers, which we approximate as linear springs normal to the surface of the membrane. We assume the cortex remains stationary on the timescale of bleb nucleation, and thus simply acts as anchorage points to membrane nodes.

$$\omega \frac{\partial}{\partial t}\mathbf{x} = -\frac{\partial}{\partial \mathbf{x}} E_{elastic}(\mathbf{x}) - F_{pressure} \tag{2.22}$$

In order to determine the elastic force due to membrane tension, bending and coupling to the cortex, we must extremise (specifically minimise) the membrane energy functional. Motivation behind the method for computing the variation of the energy functional is discussed in detail in the succeeding sections

2.6 Motivation: principles from the calculus of variations

2.6.1 Overview

The calculus of variations is the mathematical field concerned with extremising (maximising or minimising) functionals. It defines the methodology through which the stationary points of integrals are determined.

Definition 1
A functional $F[y]$ depends on a function $y(x)$, through an integral:
$F[y] = \int dy f(y(x), y'(x), y''(x), ...)$

where the 'density' in the integrand,f, depends on the local value of y and, in principle its derivatives $y', y'', ...$ (where $y' = dy/dx$)

The derivative of such a functional, $\delta F/\delta y$ is called the first variation. The Euler-Lagrange equations, $\delta F/\delta y = 0$ are pdes, whose solutions yield the stationary points of the functional.

2.6.2 Variation of a general functional: Weak and strong forms of the Euler-Lagrange equations

Consider the following functional,

$$J[y] = \int_b^a dx f(y, y', x) \tag{2.23}$$

where $y' = dy/dx$. The functional $J[y]$ depends on all values of $y(x)$ between $x = a$ and $x = b$. We wish to determine the function $y(x)$ for which the variation δJ is zero for any small deviation δy away from the function $y(x)$.

We calculate the variation as follows,

$$\begin{aligned}
\delta J &= J[y + \delta y] - J[y] \\
&= \int_b^a [f(y + \delta y, y' + \delta y', x) - f(y, y', x)] \\
&= \int_b^a \left[f(y, y', x) + \left.\frac{\partial f}{\partial y}\right|_{y(x)} \delta y(x) + \left.\frac{\partial f}{\partial y'}\right|_{y'(x)} \delta y'(x) + ... - f(y, y', x) \right]
\end{aligned} \tag{2.24}$$

where we have applied the Taylor expansion for small δy and neglect higher order terms.

We continue to keep only terms of linear order in δy, and integrate by parts to remove the derivative term from δy,

$$\begin{aligned}
\delta J &= \int_b^a \left[\left.\frac{\partial f}{\partial y}\right|_{y(x)} \delta y(x) + \left.\frac{\partial f}{\partial y'}\right|_{y'(x)} \delta y'(x) \right] \\
&= \left.\frac{\partial f}{\partial y'}\right|_{y'(x)} \delta y(x) \Big|_b^a + \int_b^a \left[\left.\frac{\partial f}{\partial y}\right|_{y(x)} \delta y(x) - \left(\frac{d}{dx} \left.\frac{\partial f}{\partial y'}\right|_{y'(x)} \right) \delta y(x) \right]
\end{aligned} \tag{2.25}$$

Now we consider only variations with fixed end-points, $\delta y(a) = \delta y(b) = 0$, and therefore the variation is simply,

$$\delta J = \int_b^a \left[\left.\frac{\partial f}{\partial y}\right|_{y(x)} \delta y(x) - \left(\frac{d}{dx} \left.\frac{\partial f}{\partial y'}\right|_{y'(x)} \right) \right] \delta y(x) \tag{2.26}$$

Equation 2.26 is known as the weak-form Euler-Lagrange equation.

To have $\delta J = 0$ for any arbitrary fixed end-point variation δy, we apply the following lemma,

Lemma 1 (Fundamental lemma of the calculus of variations) *If a continuous function f on an open interval (a, b) satisfies the equality:*
$\oint_a^b f(x)v(x)dx = 0$
for all compactly supported smooth functions $v(x)$ on (a, b), then f is identically zero.

and thus recover the following equation,

$$\frac{\partial f}{\partial y} - \frac{d}{dx}\left(\frac{\partial f}{\partial y'}\right) = 0 \tag{2.27}$$

which is known as the strong-form Euler-Lagrange equation.

2.7 Determining the first variation of the membrane energy functional

As outlined by the variational method, we perturb $\mathbf{x}$ by a test function $\epsilon\mathbf{v}$, and compare $E(\mathbf{x})$ with $E(\mathbf{x} + \epsilon\mathbf{v})$, keeping only terms of linear order in ϵ:

$$\begin{aligned} \partial E &= \left.\frac{d}{d\epsilon} E(\mathbf{x} + \epsilon\mathbf{v})\right|_{\epsilon=0} = 0 \\ &= \left.\frac{E(\mathbf{x} + \epsilon\mathbf{v}) - E(\mathbf{x})}{\epsilon})\right|_{\epsilon=0} \end{aligned} \tag{2.28}$$

Note that this holds for all endpoint-fixed variations $\mathbf{v}$ in the tangent space to $\mathbb{R}^n$ at the point $\mathbf{x}$.

For simplicity, we determine the variation of each contribution (bending, tension, coupling) separately.

(i) Bending:
Since we have linearity of the d^2/ds^2 operator, we may separate out the linear terms as follows,

$$\begin{aligned}
E_{bending} &= \frac{1}{2}\oint_0^1 k_b\left(\left|\frac{d^2\mathbf{x}}{ds^2}\right|\right)^2 ds \\
\partial E_b &= \frac{k_b}{2\epsilon}\oint_0^1 \left[\left(\frac{d^2}{ds^2}(\mathbf{x}+\epsilon\mathbf{v})\right)^2 - \left(\frac{d^2}{ds^2}\mathbf{x}\right)^2\right] ds \\
&= \frac{k_b}{2\epsilon}\oint_0^1 \left[\left(\frac{d^2}{ds^2}(\mathbf{x}+\epsilon\mathbf{v})\right)\cdot\left(\frac{d^2}{ds^2}(\mathbf{x}+\epsilon\mathbf{v})\right) - \left(\frac{d^2}{ds^2}\mathbf{x}\right)\cdot\left(\frac{d^2}{ds^2}\mathbf{x}\right)\right] ds \\
&= \frac{k_b}{2\epsilon}\oint_0^1 \left[\frac{d^2}{ds^2}\mathbf{x}\cdot\frac{d^2}{ds^2}\mathbf{x} + 2\epsilon\frac{d^2}{ds^2}\mathbf{x}\cdot\frac{d^2}{ds^2}\mathbf{v} + \epsilon^2\frac{d^2}{ds^2}\mathbf{v} - \frac{d^2}{ds^2}\mathbf{x}\cdot\frac{d^2}{ds^2}\mathbf{x}\right] ds \\
&= k_b\oint_0^1 \left[\frac{d^2}{ds^2}\mathbf{x}\cdot\frac{d^2}{ds^2}\mathbf{v}\right] ds \\
&= k_b\oint_0^1 \left[\frac{d^4}{ds^4}\mathbf{x}\mathbf{v}\right] ds = 0
\end{aligned} \tag{2.29}$$

Equation 2.29 is the weak form Euler-Lagrange equation.

Thus by Lemma 1, we arrive at the strong form Euler Lagrange equation for the bending energy,

$$\partial E_b = k_b\frac{d^4}{ds^4}\mathbf{x} \tag{2.30}$$

(ii) Tension:

$$
\begin{aligned}
E_{tension} &= \frac{1}{2}\oint_0^1 k_t\left(\left|\frac{d\mathbf{x}}{ds}\right| - x_0\right)^2 ds \\
\partial E_t &= \frac{d}{d\epsilon}\frac{1}{2}\oint_0^1 k_t\left(\left|\frac{d}{ds}(\boldsymbol{x}+\epsilon\boldsymbol{v})\right| - x_0\right)^2 ds \\
&= \frac{d}{d\epsilon}\frac{1}{2}\oint_0^1 k_t\left(\left(\left(\frac{d}{ds}(\boldsymbol{x}+\epsilon\boldsymbol{v}\right)^2\right)^{1/2} - x_0\right)^2 ds \\
&= \oint_0^1 -k_t\left(\left|\frac{d}{ds}(\boldsymbol{x}+\epsilon\boldsymbol{v})\right| - x_0\right)\frac{1}{2|d(\boldsymbol{x}+\epsilon\boldsymbol{v})/ds|}2\frac{d}{ds}(\boldsymbol{x}+\epsilon\boldsymbol{v})\frac{d}{ds}\boldsymbol{v}ds\Big|_{\epsilon=0} \\
&= \oint_0^1 -k_t\left(\frac{d}{ds}\boldsymbol{x} - x_0\right)\frac{1}{|d\boldsymbol{x}/ds|}\frac{d}{ds}\boldsymbol{x}\frac{d}{ds}\boldsymbol{v}
\end{aligned}
\tag{2.31}
$$

We recover the strong form of the variation by the fundamental lemma of the calculus of variations, thus giving,

$$
\partial E_t = -k_t\frac{d}{ds}\left(\frac{d}{ds}\mathbf{x} - x_0\frac{d/ds\mathbf{x}}{|d/ds\mathbf{x}|}\right) \tag{2.32}
$$

(iii) Coupling:

$$
\begin{aligned}
E_{coupling} &= \frac{1}{2}\oint_0^1 k_c(|\mathbf{x}-\mathbf{x_c}|-l_0)^2 ds \\
\partial E_c &= \frac{d}{d\epsilon}\frac{1}{2}\oint_0^1 k_c(|(\boldsymbol{x}+\epsilon\boldsymbol{v})-\boldsymbol{x_C}|-l_0)^2 ds \\
\partial E_c &= \frac{d}{d\epsilon}\frac{1}{2}\oint_0^1 k_c((((\boldsymbol{x}+\epsilon\boldsymbol{v})-\boldsymbol{x_C})^2)^{1/2}-l_0)^2 ds \\
&= \frac{k_c}{2}\oint_0^1 \frac{2\boldsymbol{v}(-\boldsymbol{x_C}+\epsilon\boldsymbol{v}+x)(((-\boldsymbol{x_C}+\epsilon\boldsymbol{v}+x)^2)^{1/2})-l_0}{((-\boldsymbol{x_C}+\epsilon\boldsymbol{v}+x)^2)^{1/2}}ds\Big|_{\epsilon=0} \\
&= \frac{k_c}{2}\oint_0^1 \frac{2\boldsymbol{v}(-\boldsymbol{x_C}+x)(((-\boldsymbol{x_C}+x)^2)^{1/2})-l_0}{((-\boldsymbol{x_C}+x)^2)^{1/2}}ds \\
&= k_c\oint_0^1 \boldsymbol{v}\frac{(\boldsymbol{x}-\boldsymbol{x_C})}{|\boldsymbol{x}-\boldsymbol{x_C}|}(|\boldsymbol{x}-\boldsymbol{x_C}|-l_0)ds
\end{aligned}
\tag{2.33}
$$

Thus the strong form of equation 2.33 is given by,

$$
\partial E_c = k_c(|\mathbf{x}-\mathbf{x_c}|-l_0)\cdot\frac{(\mathbf{x}-\mathbf{x_c})}{|\mathbf{x}-\mathbf{x_c}|} \tag{2.34}
$$

2.8 Numerical scheme

In order to numerically solve equation 2.22, we first express the right hand side in terms of finite differences. Using this fully discrete form, we may then compute the position vector of all nodes at each time step, and thereby update the existing curve, allowing us to visualise the membrane deformations over time and determine the sites of bleb nucleation.

We define the scheme over the contour length on the interval $[1 : \Delta s : N]$, where N is the total number of discrete nodes, s_i. Periodic boundary conditions apply, since the system exists on a closed curve.

For a differentiable function $f(s)$ defined on the contour, we can approximate the spatial derivatives with respect to s as follows,

$$\partial_{s+} f(s_i) = \frac{f(s_{i+1}) - f(s_i)}{\Delta s} \tag{2.35}$$

$$\partial_{s-} f(s_i) = \frac{f(s_i) - f(s_i - 1)}{\Delta s} \tag{2.36}$$

$$\partial_{s,s} f(s_i) = \frac{f(s_{i+1}) - 2f(s_i) + f(s_{i-1})}{\Delta s^2} \tag{2.37}$$

$$\partial_{s,s,s,s} f(s_i) = \frac{\partial_{s,s} f(s_{i+1}) - \partial_{s,s} 2f(s_i) + \partial_{s,s} f(s_{i-1})}{\Delta s^2} \tag{2.38}$$

Note that we can define the fourth order term recursively as the second derivative of the second order term.

Together with these approximations and equations 2.30,2.32 and 2.34, we discretise the pde 2.22:

$$\begin{aligned} \frac{d}{dt} x^j = \frac{1}{\omega} \Bigg[& k_t \partial_{s,s} x^j - k_t x_0 \partial_{s-} \left(\frac{\partial_{s+} + x^j}{|\partial_s^+ \boldsymbol{x}|} \right) \\ & - k_b \partial_{s,s,s,s} x^j - k_c (|\boldsymbol{x} - \boldsymbol{x_c}| - l_0) \cdot \frac{(x^j - x_c^j)}{|\boldsymbol{x} - \boldsymbol{x_c}|} - F^j_{pressure} \Bigg] \end{aligned} \tag{2.39}$$

Note that we now express the position vector as $\mathbf{x} = (x^0, x^1) = (x, y)$, such that both x and y components of the PDE can be expressed through x^j, for $j = (0, 1)$.

Writing this out in full yields,

$$\begin{aligned}\frac{d}{dt}x^j = \frac{1}{\omega}\Bigg[& \frac{k_t}{\Delta s^2}\Bigg((x^j(s_{i+1}) - 2x^j(s_i) + x^j(s_{i-1})) \\ & - x_0\left(\frac{x^j(s_{i+1}) - x^j(s_i)}{|\boldsymbol{x}(s_{i+1}) - \boldsymbol{x}(s_i)|} - \frac{(x^j(s_i) - x(s_{i-1})}{|\boldsymbol{x}(s_i) - \boldsymbol{x}(s_{i-1}|}\right)\Bigg) \\ & - k_b\left(\frac{\partial_{s,s}x^j(s_{i+1}) - \partial_{s,s}2x^j(s_i) + \partial_{s,s}x^j(s_{i-1})}{\Delta s^2}\right) \\ & - k_c(|\boldsymbol{x}(s_i) - \boldsymbol{x_C}(s_i)| - l_0) \cdot \frac{(x^j(s_i) - x_c^j(s_i))}{|\boldsymbol{x}(s_i) - \boldsymbol{x_C}(s_i)|} - pA_i n^j(s_i)\end{aligned} \tag{2.40}$$

where the pressure parameter, $p = p_0(A_0/A)$, for initial pressure p_0, initial interior area A_0, and current interior area A. The area element on which the pressure force acts at node i is expressed as A_i, and is given by $A_i = d\tilde{s} \cdot dz$. The local normal vector to the contour is similarly denoted by n^j.

We then solve equation 2.40 numerically in MATLAB, utilising the built-in ode solvers.

2.9 Dimensional analysis

A comprehensive list of all parameters/variables used in the model equations and derivations, alongside their corresponding SI units is provided in table 2.9.

Making use of this, we now proceed with a dimensional analysis of the discrete membrane evolution PDE (equation 2.40).

$$\text{LHS: } \frac{d}{dt}x^j \rightarrow ms^{-1} \tag{2.41}$$

Table 2.1: SI units of all parameters

Parameter/variable	Description	SI Units
k_t	Membrane tension stiffness coefficient	Nm^{-1}
$\tilde{k_b}$	Membrane bending modulus	Nm^2
k_b	Rescaled membrane bending modulus	Nm^{-1}
k_c	Linker stiffness coefficient	Nm^{-1}
x	Membrane spring element vector	m
x_c	Cortex element vector	m
N	Number of nodes	--
$\tilde{s}$	Arc length	m
s	Normalised arc length parameter	--
Δs	Fractional contour length (node spacing)	--
R_c	Radius of curvature	m
κ	curvature	m^{-1}
n	Unit normal vector	--
x_0	Membrane resting length	m
l_0	Linker resting length	m
p	Hydrostatic pressure	Nm^{-2}
A	Cell area	m^2
η	Dynamic viscosity	Nsm^{-2}
ω	Drag coefficient	Nsm^{-1}

RHS, term 1: $\frac{1}{\omega}\partial E_{tension}$

$$\begin{aligned}
&= \frac{1}{\omega}\left[\frac{k_t}{\Delta s^2}\left((x^j(s_{i+1}) - 2x^j(s_i) + x^j(s_{i-1}))\right.\right.\\
&\quad \left.\left. - x_0\left(\frac{x^j(s_{i+1}) - x^j(s_i)}{|\boldsymbol{x}(s_{i+1}) - \boldsymbol{x}(s_i)|} - \frac{(x^j(s_i) - x(s_{i-1})}{|\boldsymbol{x}(s_i) - \boldsymbol{x}(s_{i-1}|}\right)\right)\right]\\
&\to \frac{1}{Nsm^{-1}}\left[Nm^{-1}(m-m)\right]\\
&= N^{-1}s^{-1}mNm^{-1}m\\
&= ms^{-1}
\end{aligned} \tag{2.42}$$

RHS, term 2: $\frac{1}{\omega}\partial E_{bending}$

$$\begin{aligned}
&= \frac{1}{\omega}\left[k_b\left(\frac{\partial_{s,s}x^j(s_{i+1}) - \partial_{s,s}2x^j(s_i) + \partial_{s,s}x^j(s_{i-1})}{\Delta s^2}\right)\right]\\
&\to \frac{1}{Nsm^{-1}}\left[Nm^{-1}m\right]\\
&= N^{-1}s^{-1}mNm^{-1}m\\
&= ms^{-1}
\end{aligned} \tag{2.43}$$

RHS, term 3: $\frac{1}{\omega}\partial E_{coupling}$

$$\begin{aligned}
&= \frac{1}{\omega}\left[k_c(|\boldsymbol{x}(s_i) - \boldsymbol{x_C}(s_i)| - l_0)\cdot\frac{(x^j(s_i) - x_c^j(s_i))}{|\boldsymbol{x}(s_i) - \boldsymbol{x_C}(s_i)|}\right]\\
&\to \frac{1}{Nsm^{-1}}\left[Nm^{-1}m\frac{m}{m}\right]\\
&= N^{-1}s^{-1}mNm^{-1}m\\
&= ms^{-1}
\end{aligned} \tag{2.44}$$

$$
\begin{aligned}
\text{RHS, term 4: } & \frac{1}{\omega} F_{pressure} \\
& = \frac{1}{\omega}\left[\frac{p_0 A_0}{A} A_i n^j\right] \\
& \rightarrow \frac{1}{N s m^{-1}}\left[N m^{-2} \frac{m^2}{m^2} m^2\right] \\
& = N^{-1} s^{-1} m N m^{-2} m^2 m^{-2} m^2 \\
& = m s^{-1}
\end{aligned}
\tag{2.45}
$$

2.10 Initialising model geometry from real cell contours

We use the Quantitative Imaging of Membrane Proteins (QuimP) ImageJ plugin to segment the cells imaged through confocal microscopy. QuimP was first created by Till Bretschneider and Thorsten Libotte in 2002 [Dormann et al., 2002] to automatically track cell outlines over time, as well as the local intensities of the cortical fluorescence. QuimP was further developed by Richard Tyson [Tyson et al., 2010] to include an upgraded node tracking technique, referred to as the electrostatic contour migration method (ECMM). Tyson also included tools for further quantitative analysis, such as functionality to generate spatio-temporal heatmaps of fluorescence and velocity. QuimP still continues to be developed, with an updated segmentation method included in the latest software release.

2.10.1 QuimP work flow

i Segmentation (BOA plugin): uses the active contour method, as adapted from Kass [Kass et al., 1988]. More recently, a random walk method has also been implemented, that allows for cell segmentation in the DIC channel. The following parameters are used in the segmentation process: node spacing, max iterations, blow up (the number of pixels used to increase expand the solution to the previous frame), critical velocity (cut-off speed after which the node position is frozen), image force (controls the magnitude of the force due to local image intensity gradient pushing nodes outwards), central force (controls the magnitude of the force pulling nodes inwards), contract force (controls the magnitude of the force pulling nodes together), final shrink (number of pixels used to shrink snake to the cell boundary), sample tan and sample norm (defines the width and height in pixels of the sampling box around each node for which the intensity is sampled), previous snake (uses segmentation solution

of previous time frame as initial condition for current time frame, if selected), and finally, expanding snake (used if the user wishes to expand the initial snake for segmentation). The balancing of the image, central and contraction forces is the major determining factor in the overall segmentation quality.

ii Membrane tracking (ECMM plugin): uses an electrostatic field method to track membrane node positions and velocities. (virtual charged markers placed on the contour migrate along the field lines between the current contour, and the oppositely charged contour at time frame $t = i + 1$, thus defining their new position. A fundamental characteristic of this approach is that field lines never cross).

iii Fluorescence measurement (ANA plugin): pixel intensities are sampled from the cortex, whose width is determined by the user.

iv Data analysis (Q analysis plugin): Generates statistics (x and y coordinates, node velocities, fluorescence intensities, cell area, cell perimeter) and spatio-temporal heat maps of velocity and fluorescence.

2.10.2 Generating model membrane, cortex and linker positions

To initialise the model geometry, the contour of interest was processed through the QuimP work flow outlined above, and read into MATLAB. x and y coordinates of the segmented cell contour were extracted from the snake file. The contour was then resampled such that the spacing between nodes is 0.3μm to allow for nucleating blebs to be resolved in enough detail. The cortex was then defined by moving each membrane node 40nm inwards, in the direction of the local normal. The normal vectors to the surface was computed as follows,

$$\begin{aligned} dx &= x(r) - x(l) \\ dy &= y(r) - y(l) \end{aligned} \tag{2.46}$$

$$\begin{aligned} n &= \sqrt{(}dx.^2 + dy.^2) \\ n_x &= -dy./n \\ n_y &= dx./n; \end{aligned} \tag{2.47}$$

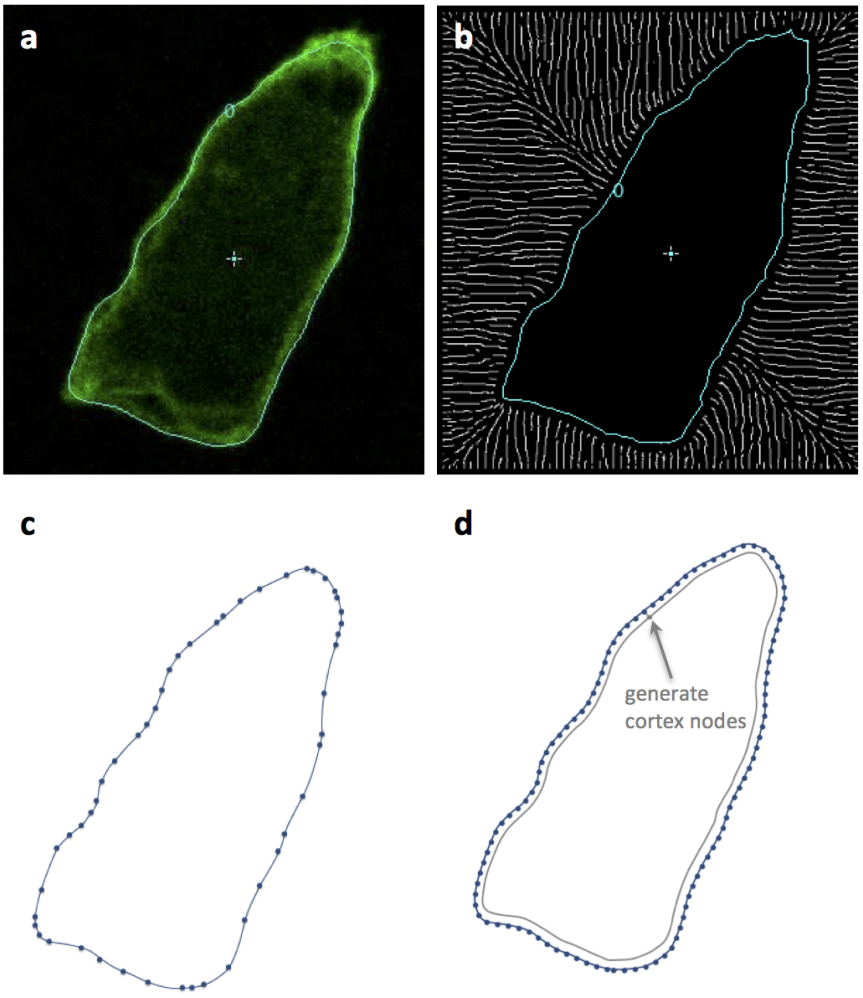

Figure 2.5: QuimP segmentation of *Dictyostelium* cell migrating under 0.7% agarose. (a) Segmented cell contour for cell expressing ABD-GFP (b) White paths indicate the contracting snake from the initial region of interest, with the solution converging to give the desired cell contour (c) Nodes are initially unevenly distributed. (d) We redistribute the membrane nodes, such that they are spaced at equidistant intervals, and generate the cortex nodes to be a distance d away, in the direction of the local normal, where d is the average linker length.

where the left and right indexing vectors are given by $l = [N, 1 : N-1], r = [2 : N, 1]$, for N nodes.

Linkers were then positioned between every membrane and cortex node pair.

2.11 χ^2 test- statistical significance with respect to random bleb site selection

To asses the hypothesis that bleb site selection is predominantly dependent on the cellular geometry, we have developed a method for ranking regions around the cell contour based on the bleb nucleation likelihood predicted by the model (section 4.6). Each experimentally observed bleb therefore is labelled by the rank of the region it covers. We define the 'bleb distribution' to be the distribution of rankings of experimentally observed blebs, for a sample of n cell contours.

We statistically test for significance above random bleb site selection, to show whether the bleb distribution we arrive at could have been entirely due to stochastic effects, by using χ^2 goodness of fit tests for each experimental condition (e.g low vs high resistance). The χ^2 test for goodness of fit of two distributions requires two inputs: the observed distribution (O) and the expected distribution (E). O is the bleb distribution, but we must generate the E distribution for random nucleation site selection. We do this by random re-sampling of the n cell contour rankings a large number of times (5000 iterations) to produce a 'test distribution'. The χ^2 test statistic is then given by,

$$\chi^2 = \sum_{i=1}^{n} \frac{(O_i - E_i)^2}{E_i} \tag{2.48}$$

with $k = N - 1$ degrees of freedom, for N bins. Since we are using ordinal data, we use class widths of 1.

The p-value for such a χ^2 test is defined by,

$$p = 1 - \frac{\gamma(k/2, \chi^2/2}{\Gamma(\chi^2/2)} \tag{2.49}$$

where Γ is the gamma function, and γ the lower incomplete gamma function.

To compute the significance level of individual bins, we must correct the p-values for multiple comparisons, for which many methods exist, but here we employ the most conservative of these: Bonferroni correction. The Bonferroni correction associates the chosen α for the statistical analysis to be for the entire set of n observations, and thus the α level for each comparison is defined to be α/n. (Recall that α is a number between 0 and 1 such that a p-value $p(z \geq z_{observed}) \leq \alpha$ is considered significant.

2.12 Determining cellular polarisation axis

In order to determine the polarisation of individual cells in each time frame of an image sequence, we fit the cell contours to an ellipse, as a means to estimate the length of the major and minor axes. The polarisation is then defined to be the ratio of the lengths of the two axes. We subsequently find the closet points on the cell contour to the end points of the major axis; these will define the front and rear of the cell. To assign which end is the front of the cell, we compare the contours of five successive time frames, and define the cell front to be the direction of persistent movement. For all circular statistic analysis, the front node of the cell is defined to be at 0^o, i.e. up-gradient in cAMP chemotaxis assays, and the rear node is defined to be at 180^o. All other nodes are assigned angles by linear interpolation between the front and rear nodes.

2.12.1 Algorithm for automatic detection of the cell front, and calculation of cellular polarisation

(i) Read in cell contour coordinates, $(\vec{x}, \vec{y})$

(ii) Define independent variable matrix $\tilde{X} = [\vec{x} \bigotimes \vec{x}, \vec{x} \bigotimes \vec{y}, \vec{y} \bigotimes \vec{y}, x, y]$

(iii) Compute optimum parameters using least squares estimator, $\vec{\beta} = (\tilde{X}'\tilde{X})^{-1}\tilde{X}'\vec{1}$

(iv) Calculate geometric parameters a, b, x_0, y_0, θ from the now known values of $\vec{\beta}$

(v) Find closest nodes (i.e. minimum euclidean distance) on cell contour to end-points of major axis

(vi) Determine which of these two nodes corresponds to the cell front, and which to the cell rear, by comparing successive time frames: for a contour at time frame $t = i$ compared to a contour at $t = i + 1$, the node corresponding to the cell rear will have migrated inside the contour, whereas the front node will have moved outside

(vii) For later circular statistics analysis and polar histograms, fix the front node to be at 0^o and the rear node to be 180^o. Recover angles of all other contour nodes between 0^o and 360^o via linear interpolation between the front and rear.

2.13 Kuiper test

The Kuiper test was used to compare the CDF functions of bleb frequency against angle (with 0^o defined to be the front of the cell and 180^o the rear) for experimental results vs. different versions of the model, to determine whether it is reasonable that the sample data from each could be approximated by the same distribution. The Kuiper test is closely related to the KolmogorovSmirnov test, and similarly uses the discrepancy statistics D_+ and D_- to represent the magnitudes of the most positive and negative differences between the two cumulative distributions being compared.

The Kuiper test statistic is given by,

$$\begin{aligned} V &= D_+ + D_- \\ &= max(|S_1 - S_2|) + max(|S_2 - S_1|) \end{aligned} \tag{2.50}$$

for cumulative distribution functions, S_1 and S_2.

The Kuiper test has the advantage over the Kolmogorov-Smirnov test in that since it considers both positive and negative differences, it is as sensitive in the distribution tails as at the median. In addition, the Kuiper test is circularly invariant, since if we were to change the starting point of the integration of the two probability distributions, although D_+ and D_- would change individually, their sum remains constant.

2.14 Fluorescence analysis

In order to extract the cortical fluorescence intensities for either ABD-GFP cells or TalinA-mNeon cells, we used the ANA plugin of the QuimP software. The cortical region was defined to be a continuos strip of uniform thickness, bounded by the cell outline. The fluorescence was then sampled in ANA at uniform intervals around the cell, using a 3x3 averaging kernel to record only the maximal intensity for each marker. To preserve

any thin protrusions or areas with large curvature gradients, the inner boundary of the cortical strip was determined through iteratively shifting the outer markers inwards, in the direction of the local normal. This was achieved whilst maintaining the original node density, and preventing self-intersections between subsequent boundaries. For all quantitative analysis, normalised fluorescence rather than absolute intensity values were used.

Chapter 3

Experimental methods

3.1 Overview

In the following sections, we will discuss the various techniques used to culture *Dictyostelium* cells, for the experimental results presented in this thesis, in addition to how the developmental stage in the social lifecycle was controlled, for example how cell aggregation was induced. We will subsequently discuss the under-agarose assay through which blebbing motility was promoted, and the imaging techniques used to visualise the cell migration. We also present the methods used for generating fluorescently tagged constructs of TalinA, a membrane-cortex linker protein.

3.2 Media

The majority of the experimental work in this thesis, was carried out at the LMB, where general cell culture media, buffers and stocks were kindly provided by the LMB cell biology division 'media kitchen'. 3D work, using the diSPIM light sheet microscope, was performed at the MCCB centre in Warwick, where media preparation had to be self-sufficient.

The most frequently used media and reagents are listed as follows,

- Axenic medium, HL5 (Formedium): peptone 14g/l, yeast extract 7g/l, glucose 13.5g/l, KH_2PO_4 0.5g/l, Na_2HPO_4 0.5g/l
- KK_2 buffer (sometimes referred to as development buffer): 16.5mM KH_2PO_4, 3.9mM K_2HPO_4, 2mM $MgSO_4$, 0.1mM $CaCl_2$ (pH 6.1)

- SM agar plates: 1% Bacto-Peptone (DIFCO), 0.1% yeast extract (DIFCO), 0.22% KH_2PO_4, 0.1% Na_2HPO_4, 1.5% agar, 1% glucose, 8mM $MgSO_4$.
- New Salts (NS): KCl 20mM, NaCl $20mM$, $CaCl_2.6H_2O$ 1mM
- Electroporation buffer (H40): 40mM HEPES/KOH (pH 7.0)
- Freezing medium: Horse serum, 7.5% DMSO

3.3 Cell strains used

In the majority of experiments, the axenic strain Ax2 (Kay laboratory strain; DBS0235521 in DictyBase) was used as the wild-type strain. Other strains used are as follows,

- HM2040: strain expressing ABD-GFP for visualizing F-actin.
- HM1554: TalinA/B- double knockout. (A kind gift of M.Tsuijioka to Kay laboratory). This strain was rescued by expressing TalinA-GFP or TalinA-mNeon.

3.4 *Dictyostelium* cell culture

True wild type *Dictyostelium* cells (NC-4 strain) can propagate in the presence of a bacterial food source either on a solid substrate, or in a liquid medium. The cells can be grown either in a 22^0C incubator, or on the laboratory bench, provided that room temperature is within a $2-3^0C$ tolerance of 22^0C. Nevertheless, it is often desirable to grow the *Dictyostelium* cells axenically (in the absence of bacteria), particularly for imaging purposes. Whilst all *Dictyostelium* strains can be cultured in the presence of bacteria, only axenic strains (Ax2, Ax3, Ax4 and derivatives) can be grown in the absence of bacteria. Each culturing method has its own advantages, for example for efficient isolation of clones, it is advantageous to grow the clones on bacteria, since the growth rates are approximately double that of axenic methods.

3.4.1 Axenic growth

Two culturing methods for axenic growth were used: (i) growth in shaking suspension and (ii) growth on plastic plates. Method (ii) was used when shaking incubators were not available, or when it was necessary to observe cells frequently, and when cell attachment to a substrate was desirable during growth. Here we will discuss in more

detail the protocols for both culturing methods, although it is standard procedure, since factors such as cell density are vital for not only for maintaining a healthy culture, but also for ensuring cells are in the desired developmental stage in the social amoeba lifecycle.

(i) Growth in shaking suspension

(i) Cells were inoculated at 5×10^4 cells ml^{-1} into a flask containing nutrient rich HL5 medium, and stored in a 22^0C shaking incubator at $180rpm$.

(ii) The liquid media volume was $\leq 20\%$ of the flask volume to ensure sufficient aeration

(iii) Cells were subsequently split into fresh media after 2-3 days, such that the density did not exceed 4×10^6 cells ml^{-1}.

(iv) Cultures were split as necessary to maintain a healthy population number (i.e. within the exponential growth phase, before stationary phase), for maximum of 4 weeks. After such a time period, cultures were renewed from frozen stocks (section 3.4.4) to prevent the accumulation of genetic mutations.

(ii) Growth on plates

(i) *Dictyostelium* cells were inoculated at 1×10^4 cells ml^{-1} into $10ml$ plates with HL5 media and stored in a standard (non-shaking) 22^0C incubator.

(ii) Cells attach to the surface of the plate during growth, and thus can be observed with a tissue culture microscope using 10-100x magnification.

(iii) Cultures were split as necessary to maintain a healthy population number.

3.4.2 Growth in association with bacteria

Although several methods for *Dictyostelium* growth with bacteria exist, here we only use the technique of co-culturing the *Dictyostelium* cells with live bacteria on SM plates. This method was only used for clonal isolation after transformation (section **??**), all other protocols used axenically grown cells.

(i) To inoculate the plates, 8×10^4 *Dictyostelium* cells were mixed with $0.2ml$ of overnight cultured *Klebsiella aerogenes*, and spread onto $10ml$ SM plates with a sterile glass spatula.

(ii) To ensure no undetected colonies were present on the SM plates which could lead to contamination of the amoeba, fresh plates were incubated for 2-3 days at 22^0C before use.

(iii) Since the bacterial growth rate is significantly higher than that of the *Dictyostelium*, the plate's appearance becomes fully opaque in the first day of culture, due to the 'bacterial lawn' covering the entire surface.

(iv) *Dictyostelium* subsequently clear this lawn by consuming the bacteria.

(v) Once the plate is fully cleared, *Dictyostelium* cells no longer have a food source, and therefore start to aggregate as they enter development.

(vi) Cells were harvested before this stage, after $42 - 48$hours, when the plates were only half cleared.

3.4.3 Harvesting and counting cells

Dictyostelium cells can be vortexed and centrifuged without lysis. However, cells cannot be left at high densities in a pellet for longer than a few minutes, since the cells become anaerobic, swell and can eventually lyse.

(i) Cells were harvested in salts solutions and centrifuged at 1400rpm for 2-3 minutes.

(ii) For *Dictyostelium* cultures grown axenically, cells were spun down in the HL5 media, and then washed twice by resuspension in either salts solution or KK_2.

(iii) For *Dictyostelium* cultures grown with bacteria on SM plates, a few ml of KK_2 was added to the SM plate, allowing the cells to be scraped off the surface into the liquid. This liquid was subsequently pipetted into sterile 50ml falcon tube. The cells were vortexed to break up any lumps, and KK_2 was added to make up a final volume of $25ml$. Cells were pelleted via centrifuging, and the supernatant discarded. The pellet was then resuspended in KK_2, and the washing process repeated 4-5 times or until the supernatant was clear. (3 SM plates were harvested per 50ml tube).

(iv) For either culturing technique, to count cells, the final pellet was resuspended to approximately 1×10^8 cells ml^{-1}. Cells were counted using either the coulter counter or a haemocytometer. (For the coulter counter cells were diluted 1:4000 in NS, and for the haemocytometer cells were diluted at 1:50). For cells that had

been cultured axenically in the shaking incubator, the haemocytometer was used to visually check the purity and health of the cells. For cells cultured axenically on plates, this was unnecessary, since the cells were observed frequently under the tissue culture microscope.

3.4.4 Strain preservation

Mutants forming and propagating in lab cell cultures can be a common problem in *Dictyostelium* labs [Bloomfield et al., 2015], since *Dictyostelium* strains are unstable, in addition to the lack of selective pressure that would be present in the cells' natural environment. Due to this, in order to ensure reliability and reproducibility of results, it was necessary to store strains in either spore form, or via freezing, and to renew cell cultures from fresh stocks at least every month. Strains stored in spore form on a silica gel at -20^oC have a lifetime of around 10 years, similarly to cells frozen at -80^oC, whilst the viability of cell stocks stored in liquid nitrogen is indefinite. For freezing, cells were harvested in log phase (5×10^6 cells ml^{-1}), centrifuged at 1400rpm for 2 minutes and resuspended in 1.5ml of freezing medium in a cryo-vial (Nunc). Cells were then stored for 24 hours at -80^oC in a cryolite preservation chamber (Stratagene) to eliminate cell rupture due to rapid freezing, before transferring to a liquid nitrogen tank for permanent storage.

3.5 Establishing aggregation competent cells

To study blebbing motility, we require that *Dictyostelium* cells have entered development, since for the cells to migrate under agarose, they must be responsive to cAMP signalling, and thus aggregation competent. A schematic of the *Dictyostelium* lifecycle with corresponding time in hours for each stage is shown in figure 3.1. To induce synchronous development, it is important to harvest vegetative cells in the mid-log phase ($1 - 4 \times 10^6$ cells ml^{-1}), since for cell cultures at higher density, it is likely that a proportion of the cells will have already begun development, and thus over the entire cell population, a significant amount of variation will exist in the expression levels of developmental genes.

Three key techniques for initiating *Dictyostelium* development in the lab exist: (i) development on solid media (usually filter paper),(ii) development on agar plates and (iii) development in suspension. For the work presented in this thesis, only the

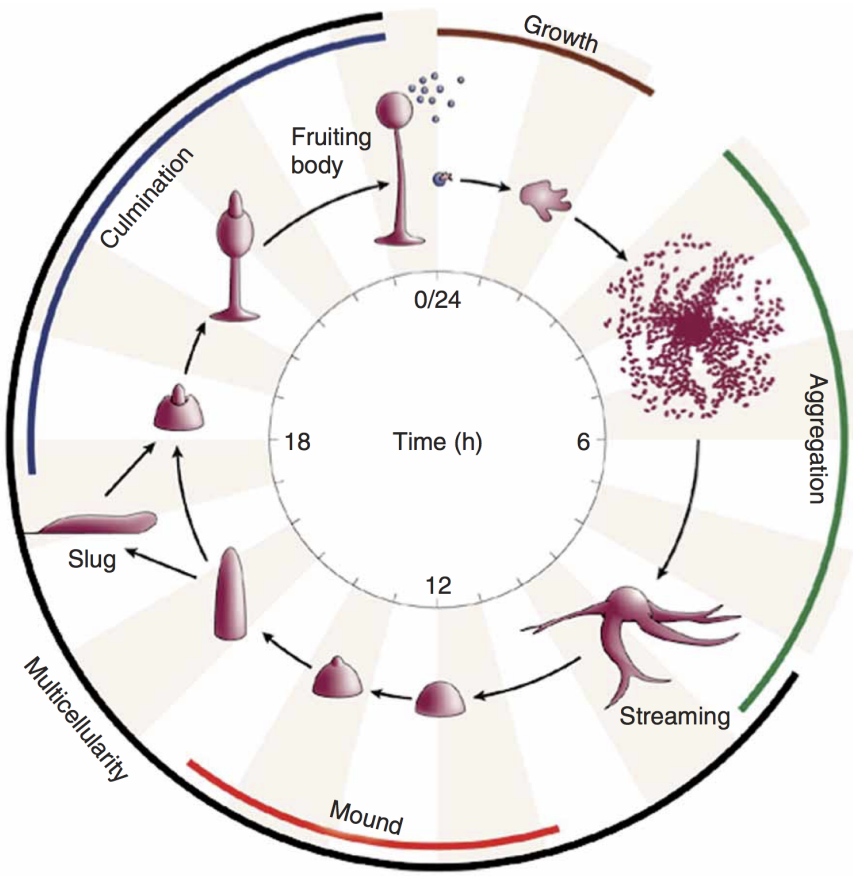

Figure 3.1: The lifecycle of *Dictyostelium* cells, progressing from a single cell amoeba to multicellular organism, and culminating in the formation of a fruiting body. The stage of the lifecycle is mediated by the abundance of the cells' food source. Image from [Fey et al., 2007].

later technique was employed, although two variations of suspension development were used: cAMP pulsing and overnight starvation.

3.5.1 cAMP pulsing

(i) Cells were harvested at 2×10^6 cells ml^{-1} and centrifuged at 1400rpm for approximately 4 minutes at room temperature.

(ii) Cells were then washed and resuspended in sterile developmental phosphate buffer.

(iii) The washing process was repeated a further two times, to avoid the presence of any leftover nutrient-rich buffer, since as *Dictyostelium* cell development is induced by starvation, any excess food source can interfere with developmental regulation.

(iv) After the final wash, cells were resuspended to a final concentration of 1×10^7 cells ml^{-1}, and transferred to a shaking incubator at 22^oC and 180rpm.

(v) cAMP pulsing was started $1-2$ hours after starvation was initiated, and continued for 5 hours. (A peristaltic pump was used to deliver cAMP to the shaking cell suspension, in 5s pulses every 6 minutes to a final concentration of 90nM. Since developing *Dictyostelium* cells express a phosphodiesterase enzyme, the added cAMP does not accumulate, but rather is degraded.

3.5.2 Overnight starvation

The protocol for overnight starvation follows the same initial three steps as the previous method, however, after the final cell wash, cells are plated onto tissue culture plates containing sterile KK_2 rather than maintained in a shaking incubator with cAMP pulses. No cAMP is added to the cells using this method, instead relying on the cell's own production of cAMP. Development in KK_2 plates is often done at 22^oC for the desired time of development ($6-8$hours for pre-streaming cells), however, if a high density cell population is optimum for imaging, then using this method risks cells streaming very rapidly. Since we wish to study blebbing motility in single cell migration, cells that are aggregation competent and highly polarised, yet not quite streaming are required. If however, the cells are stored at 10^oC instead, all cellular processes including developmental regulation are slowed sufficiently, such that cells can be left for a $12-16$ hour period at high density, and yet only reach a pre-streaming state of development, ideal for our purposes.

3.6 Under agarose assay

The first under-agarose migration assay for studying *Dictyostelium* cells was described by the Knecht group [Laevsky and Knecht, 2001], and was used as a means to increase the quality of microscopy images, since the cells were flattened under the agarose. The assay was further developed by Zatulovskiy et al. [Zatulovskiy et al., 2014] for promoting bleb-driven motility. Since this assay is fundamental to the results of this thesis, we proceed to describe the protocol in detail. (Note that as the concentration of agarose gel increases, *Dictyostelium* cells transition from mainly F-actin driven migration at 0.7% to entirely bleb-based motility at 2%).

(i) Aggregation competent cells were developed via either cAMP pulsing or overnight starvation, and harvested at 1×10^6 cells ml^{-1}.

(ii) The chamber to be used for imaging was pre-heated in a water-bath to $50 - 60^o$C, such that the glass would not crack when molten agarose was poured into it.

(iii) A suspension of $0.7 - 2\%$ low melting point ultrapure agarose in KK_2 was simultaneously heated until agarose was fully dissolved. (For experiments performed previously by Evgeny Zatulovskiy, used in the theoretical part of this thesis, 0.5mg/ml fluorescent RITC-dextran was also added to the agarose to negatively stain the cells).

(iv) Once the agarose cooled to $50 - 60^o$C, a thin layer was poured into the microscopy slide chambers. (Nunc Lab-Tek Chamber Slides, Thermo Scientific, were used with a well area 4.0cm^2. 800μl of agarose was used to create a layer $2mm$ thick).

(v) Chambers containing agarose were then kept in a moist box to prevent the gel from drying out.

(vi) Once the gel had fully stiffened, two parallel wells were cut using a sharp scalpel (A drawn gauge 1.5×8ml in size was used underneath the chamber to ensure that wells were consistently cut to the same size, with the same distance between the two wells. This was necessary to ensure cells are exposed to the same chemotactic gradient in duplicate experiments). The correct cutting of the wells is a critical step in this methodology: cuts that leave a scratch in the glass can abolish migration underneath the agarose entirely, whilst slight detachment of the gel from the slide which can occur when removing the cut gel piece, creates a gap through which cells can migrate with minimal resistance, and thus little blebbing activity.

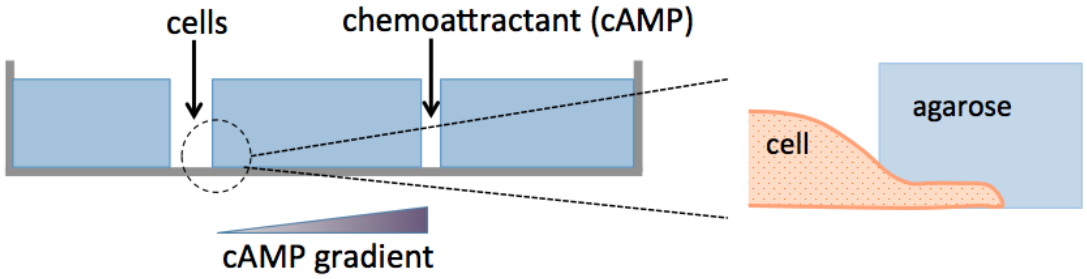

Figure 3.2: Blebbing in *Dictyostelium* can be induced by forcing the cells to migrate in a mechanically resistive environment. In this work, we use the under agarose assay, first developed by Knecht et al. to promote blebbing motility. Aggregation competent *Dictyostelium* cells, responsive to cAMP stimulation, were used in this assay. Two wells were cut into a $2mm$ thick agarose layer in a microscopy chamber. $4\mu M$ cAMP was added to one well, to establish a concentration gradient across the agarose gel. *Dictyostelium* cells were added to the other well (parallel to the first). *Dictyostelium* cells move up the concentration gradient in cAMP by forcing their way underneath the agarose layer. The concentration of the agarose gel was made to either 0.7% or 2%, to promote either predominantly F-actin driven migration with some blebbing, or migration using only blebs.

(vii) To one well, 4μM cAMP was added, whilst to the other well 1×10^5 developed *Dictyostelium* cells were added.

(viii) Before imaging, the chamber was left for at least 40 minutes, to allow time for the cAMP gradient to form across the gel, and for the cells to begin migrating underneath the agarose in response. (Figure 3.2).

3.7 Imaging

Dictyostelium cells are relatively small, $20-30\mu$m in length, and show very rapid bleb expansion, often complete within 1 second, and as such a microscope with sufficiently high spatial and temporal resolution was required. For observing blebbing motility, and recording images of high enough quality for accurate segmentation, a $40-63\times$ objective is optimal, and a frame rate of $0.5-2$ frames per second. Since the cells to be imaged are migrating underneath a layer of agarose, an inverted microscope was necessary. Images presented and analysed in this work were acquired in the relevant fluorescent channels (green for ABD-GFP, green for talin-A-mNeon, and red for dextran), at 2 frames per second, using either a spinning disc confocal microscope (Ultraview; PerkinElmer) with

a 100x oil-immersion objective, or with a Zeiss 710 laser scanning confocal microscope with a 63x oil-immersion objective. Images were collected using Zen 2010 software (Carl Zeiss).

3.7.1 Factors influencing the quality of microscopy images

(i) Thickness of agarose layer

Thicker layers of agarose gel absorb more of the laser light during imaging, in addition to reducing oxygen diffusion to cells underneath, resulting in limited migration. We therefore use layers no thicker than 2mm.

(ii) Agarose gel drying

If the agarose gel drys during imaging, its optical properties will change, leading to a loss of focus. The gel drying can also squash the underlying cells, significantly changing their appearance. To avoid this, KK_2 was added drop-wise to the wells and surface of the gel as necessary during microscopy.

(iii) Stage of *Dictyostelium* development reached

Since blebbing increases with development time, longer cAMP pulsing/starvation times are used than for classic chemotaxis assays. However, if cells proceed too far into development, they tend to aggregate into clumps, which are difficult to image, and affect the imaging contrast of nearby cells. To help eliminate this effect, cAMP pulsing was limited to 5 hours.

(iv) Expression level of fluorescently tagged construct

Clearly the expression level of the fluorescently tagged construct influences imaging quality, with a direct effect on signal to noise ratio. If the expression level and thus emitted fluorescence is too low, the difference between the object of interest and background fluorescence/auto-fluorescence is insufficient for accurate segmentation. For the majority of imaging analysed in this thesis however, ABD-GFP is used to visualise the distribution of F-actin, and has a very high expression level, such that even at very small exposure times (20ms), the signal to noise ratio is high enough for reliable

segmentation.

3.8 Molecular cloning techniques

3.8.1 Polymerase chain reaction

PrimeStar Max DNA Polymerase (Clonetech) was used to carry out PCR.

Reagent setup:

- 17μl MilliQ water
- 1μl template DNA (1000× diluted mini-prep)
- 1μl forward primer (10μM)
- 1μl reverse primer (10μM)
- 20μl PrimeStar Max

Thermocycling conditions:

Reagent setup:

No. cycles	Step	Temp (^{o}C)	Time
1	Initial denaturation	98	20s
30	denaturation	98	10s
	annealing	45	10s
	extension	68	40s
1	Final extension	68	1min

Since *Dictyostelium* genomic DNA is highly rich in A and T base pairs, the annealing temperature is lower than standard PCR protocols.

3.8.2 Transformation into *E.coli*

Plasmids were transformed into chemically competent *E.coli* XL10 cells using the heat shock method. 1μl of miniprep plasmid was added to 100μl of the competent cells and incubated on ice for 45 minutes. The cells were then heat shocked at 42^{o}C for 45 seconds on an eppendorf heat block, followed by a second incubation on ice for 2 minutes. SOB media was then added, and the cells were left to recover at 37^{o}C and 350rpm for 30

minutes. After recovery, cells were spun down at 4000rpm for 3 minutes, resuspended in 100μl of supernatant and plated onto plates containing ampicillin (since chosen plasmid contains ampicillin resistance to allow for selection of only positive clones). Plates were then incubated overnight for 37^{o}C.

3.8.3 Plasmid purification

Individual colonies were picked from the plates with the transformed *E.coli* and added to 2ml of LB medium, plus ampicillin, and incubated overnight at 37^{o}C in a shaking incubator. To purify the plasmid, a miniprep kit was used, following the manufacturer's protocol (Zymo research). For high plasmid concentrations, midiprep kits were used instead (Qiagen). The concentration of the purified plasmids was measured using a nanodrop instrument. Plasmids were confirmed to contain the desired insert via restriction digests and/or sequencing.

3.8.4 Restriction digests and ligations

Restriction digest of the DNA sequence was carried out by the appropriate restriction enzymes. The reactions were made to a total volume of 30μl, with usually 10μl insert, 3μl CutSmart, 15μl MPW water and 1μl of each enzyme and incubated at 37^{o}C for 45 minutes. In order to separate fragments by their molecular weight, to confirm positive clones, electrophoresis was carried out. The agarose gel was dissolved in 1$\times$ TBE buffer to create the gel, with SYBR safe DNA stain added to it for later visualisation of the bands. DNA loading dye was added to the digest product, which was loaded into the gel and run for $40-60$minutes at 110V. To extract the DNA, the desired bands were removed from the gel, and the Zymoclean DNA recovery kit (Zymo Research) was used as per the guidelines.

Ligation reactions were made to a 20μl total volume, using 15μl insert, 2μl vector, 2μl ligase buffer and 1μl ligase. The reactions were incubated at 16^{o}C overnight.

3.8.5 Transformation into *Dictyostelium*

Transformation of *Dictyostelium* cells with plasmids is carried out by the protocol developed by [Pang et al., 1998]. Cells are harvested in log phase at and resuspended at $4-5\times10^7$ cells ml^{-1} in H40 buffer. The cells are incubated on ice for 5 minutes. 100μl of the cell suspension is added into a pre-cooled electroporation cuvette, to which 2μg of plasmid was also added. Cells were then pulsed using 2 exponential pulses at 750V

within a 5s interval. Cells were left to recover for 1 hour before plating with HL5 medium to tissue culture plates (6 well/ 9 well/ 12 well). After 24 hours of incubation at 22^{o}C, the relevant antibiotic is added to maintain selection pressure.

3.9 Creation of a TalinA reporter

In order to investigate whether *Dictyostelium* cells have a polarised gradient in the localisation of the membrane-cortex linker protein, TalinA, with TalinA being enriched in the cell rear, it was necessary to create a fluorescently tagged TalinA construct. The generation of the Talin A reporter was achieved with the help of Peggy Paschke (Kay lab), using the Veltman extra-chromosomal expression vector system [Veltman et al. 2009]. The process used to create the construct is as follows:

(i) Amplify Talin A sequence from *Dictyostelium* genomic DNA by PCR.
Forward primer (oPI˙134):
CCGGATCCAAAATGTCAATTTCATTAAAAATTAATATTG
Reverse primer (oPI˙135):
GCACTAGTATTTTTATTATAATTTTGTTTTCTTGAATTTAAC

(ii) Clone PCR product into PJet1.2 cloning vector (transform into *E.coli* XL10 cells by heat shock. Select for positive clones by treatment with ampicillin. Gene sequence was confirmed using the Sanger sequencing service of source bioscience). Figure 3.3 shows the plasmid map for the Pjet-TalinA construct, with restriction sites highlighted.

(iii) Purify plasmids (miniprep/midiprep of bacterial culture). Concentration measured by nano drop and product confirmed by restriction digests (using restriction enzymes BamHI and SpeI)

(iv) Ligation of TalinA construct with mNeon expression vector, pP162. (pP162 was created by Peggy Paschke by ligating mNeon into *Dictyostelium* expression vector into pDM1203). pP162 has the following functional groups: (a) dicty replication -Ddp1, (b) ampicillin resistance cassette for selection in *E.coli*, (c) G418 resistance cassette driven by the CoA promoter and terminated by the mhcA terminator, and (d) dicty expression- under the control of the act15 promoter and act8 terminator. (Figure 3.4 shows the plasmid map for the generated TalinA-mNeon plasmid)

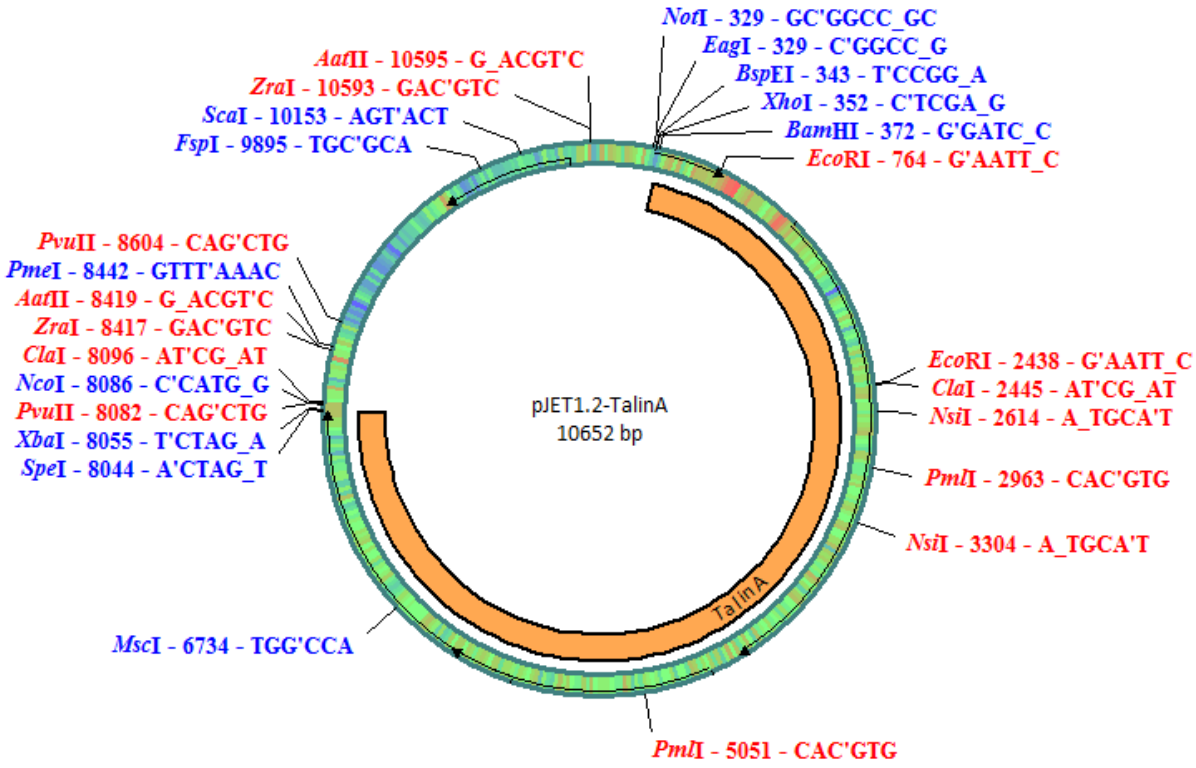

Figure 3.3: Pjet-TalinA plasmid, generated by cloning amplified genomic DNA of *Dictyostelium* TalinA into commercial PJet1.2 cloning vector. (competent XL10 E.coli cells were used for the transformation. Restriction sites that cut once are shown in blue, whilst those shown in red cut twice.

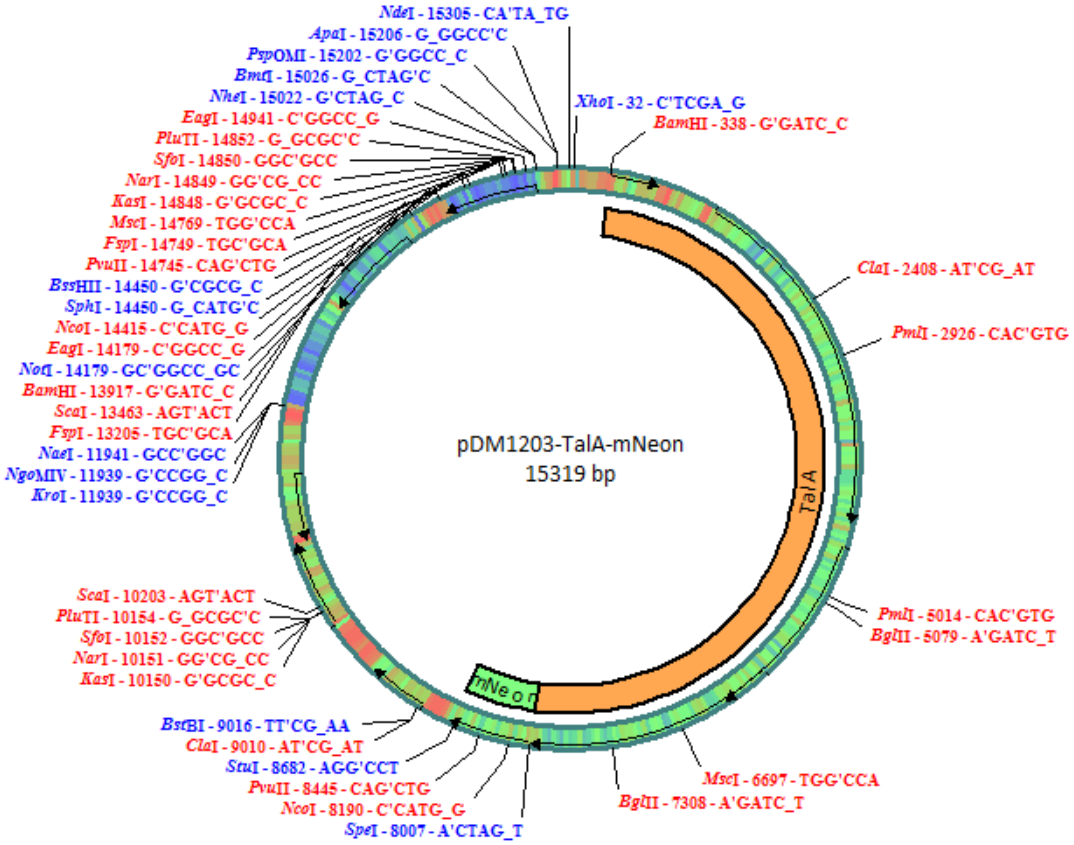

Figure 3.4: TalinA-mNeon plasmid map, generated via ligation of TalinA construct into with mNeon expression vector, pP162. Four functional groups are present in the plasmid: the site of *Dictyostelium* replication (Ddp1), an ampicillin resistance cassette for selection in E.coli, a G418 resistance cassette for selection in *Dictyostelium*, and the *Dictyostelium* expression site (under the control of actin15 promoter and actin8 terminator). Restriction sites that cut once are shown in blue, whilst those shown in red cut twice

3.10 Generating a fluorescently tagged TalinA knock-in

In collaboration with the Kay Lab, utilising the method developed by Douwe Veltman, we generated TalinA-GFP and TalinA-mNeon knock-ins. This was a necessary step to allow us to investigate the endogenous expression level of TalinA, as well as the spatial distribution of the linker protein. However, the fluorescent intensity level of the knock-in cells was too low to recover high signal to noise images necessary for quantitive analysis.

Results Overview

Aim (i) - Development of a quantitative method to predict bleb site selection

- Model initialised using real cell contours extracted from image data.

Optimising hydrostatic pressure (Section 4.3)

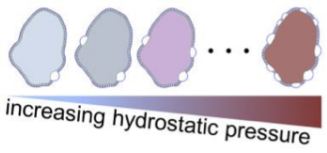

Implement automatic bleb tracking

Hydrostatic pressure as a likelihood gauge (Section 4.5)

Computational time optimisation

Linker length as a bleb likelihood gauge (Section 4.6)

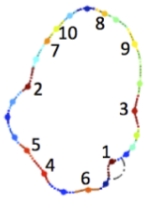

Aim (ii) – Determining whether cell geometry alone is sufficient to predict the sites of bleb nucleation

(a) Is cellular geometry a good predictor of bleb site selection

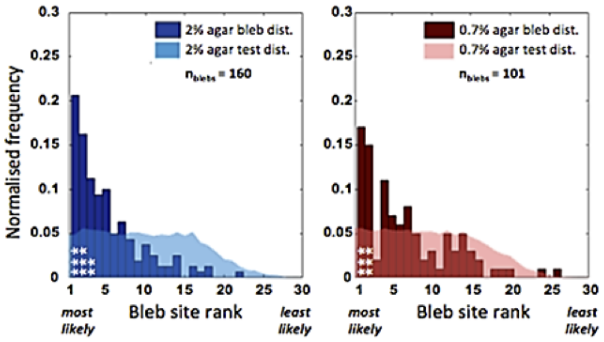

- Statistical analysis using χ^2 tests shows geometry alone is a good predictor of bleb site selection, especially for cells migrating in highly resistive environments. (Chapter 5)

(b) Cell movement in low vs. high resistive environments

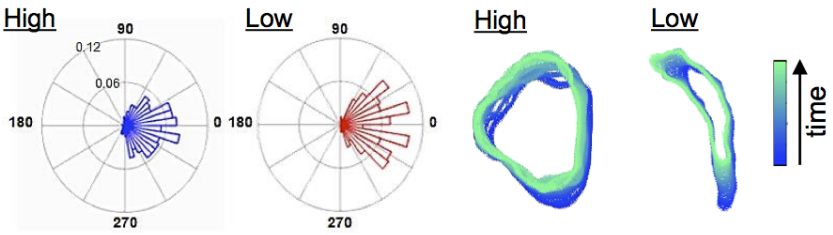

- Cell morphology is important.
- For cells migrating in low resistive environments, our results show an additional mechanism is required to further restrict blebbing to the cell front. (Chapter 5)

Aim (iii) – Further investigation of biological mechanisms that may influence bleb site selection

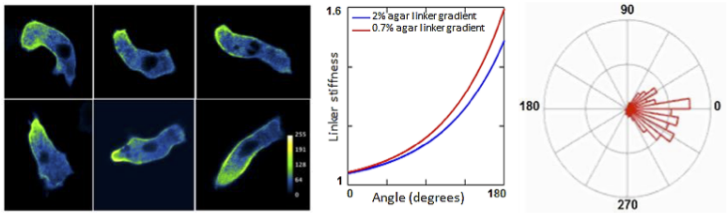

- We observe an exponential gradient in TalinA localisation.
- We incorporate this finding as an exponential stiffness within our model. (Chapter 6)

Ongoing work

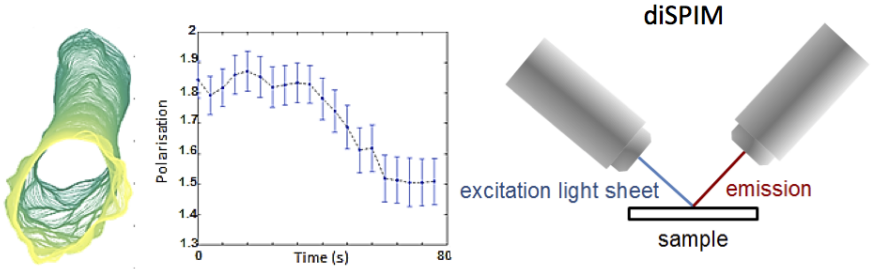

- (i) Preliminary results on multi-blebbing.
- (ii) 3d imaging using light sheet microscopy (diSPIM) (Chapter 7)

Chapter 4

Development of a quantitative method for predicting bleb site selection

4.1 Motivation

In order to create a method to directly link experimental and model data we initialise our model using real cell contours extracted from image data. In this chapter we show the development of our method to quantitatively examine the spatial distribution of model and experimental blebs, from a predominantly manual analysis to an automated process.

In addition, while our main focus within this chapter is on the initial instant of membrane detachment, i.e. predicting the location of bleb site nucleation, a consideration of bleb expansion and growth in the model via membrane peeling is also presented in section 4.7.3.

4.2 Influence of hydrostatic pressure on global blebbing propensity

4.2.1 Identification of a critical pressure

We find the parameter value of the intracellular hydrostatic pressure to have a significant effect on blebbing propensity globally, in line with observations of increased blebbing of cells in hypotonic medium. A critical value of the hydrostatic pressure can be identified

for each cell contour, below which, no blebs will nucleate, and above which, spontaneous bleb nucleation begins. Increasing the pressure parameter far above this critical value produces many blebs in the model, as demonstrated in figure 4.1.

4.2.2 Relation between hydrostatic pressure and cellular circularity

A clear separation between the values of the sub-critical pressure parameters determined for cells migrating under 2% and 0.7% agarose can be observed in figure 4.2. Cells under 0.7% agarose are typically more polarised, having circularities closer to 0, and bleb at lower pressures. Cells migrating under 2% agarose show significantly less variance in both the sub-critical pressure and circularity compared to 0.7% data, indicating that these cells are operating close to the limit of intracellular pressure.

4.3 Optimizing the hydrostatic pressure parameter

After the identification of a critical pressure, and noting that the pressure could be tuned to produce different numbers of blebs around the cell contour, the next reasonable step in mapping experimental and model data was to optimise the hydrostatic pressure parameter, to achieve the best experimental vs model match in terms of number of blebs produced and their nucleation site locations.

We used image data from the time frame before each experimental bleb was observed to initialise the model membrane and cortex geometries. For a given hydrostatic pressure parameter, the initial model geometry was evolved by the governing force balance pde to recover new membrane positions. We then manually classified the model bleb sites into true positives (regions where both experimental data and the model show bleb nucleation), false positives (regions where predicted blebs are not observed experimentally), and false negatives (regions where experimental blebs fail to be predicted by the model). The number of true negatives (regions where no experimental or model blebs nucleate) was then estimated through determining the total number of blebs that could fit around the cell perimeter, based on the average bleb diameter, and subtracting the sum of true and false positives and false negatives. The model specificity and sensitivity was then given by,

$$specificity = \frac{TN}{TN + FP} \tag{4.1}$$

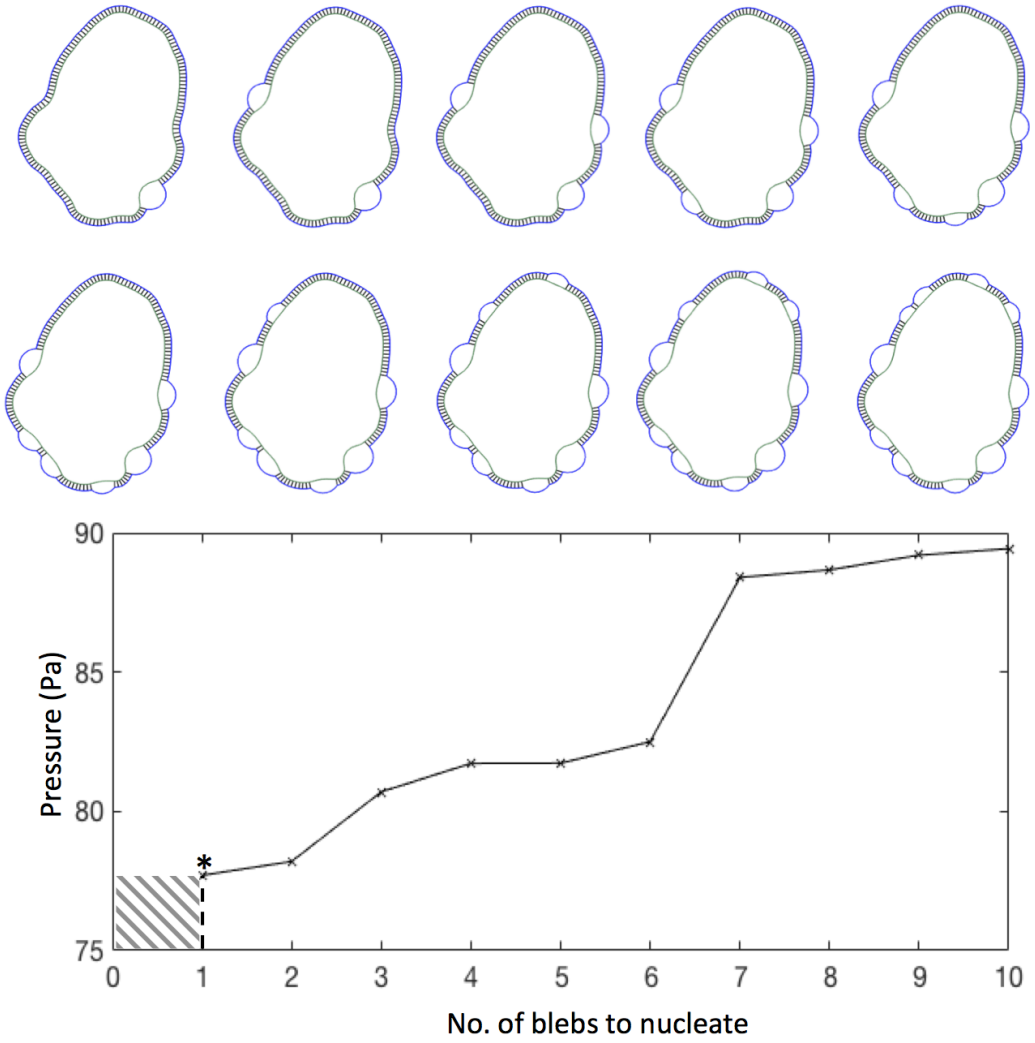

Figure 4.1: We identify the existence of a critical pressure for each cell contour used to initialise the model, below which no blebs nucleate. We treat the hydrostatic pressure as a free parameter, which we can tune to produce different numbers of blebs. Here we show the increase from the critical pressure at 77.7Pa to the pressure at which 10 blebs nucleate (89.4Pa) for an example *Dictyostelium* cell contour. Our findings of the dependence of hydrostatic pressure on blebbing propensity are in line with observations of cells in hypotonic medium.

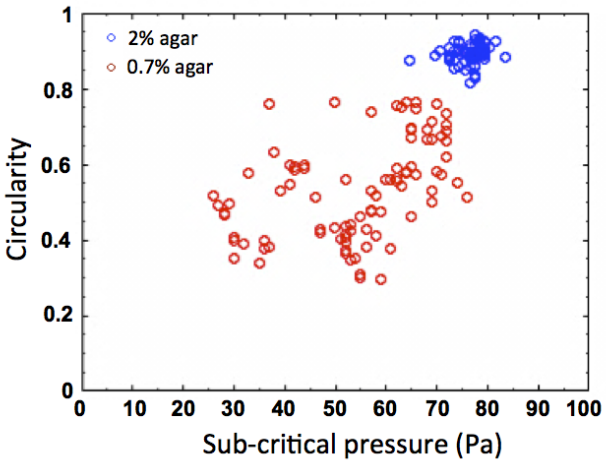

Figure 4.2: Relation between hydrostatic pressure and cellular circularity. All simulations are run at the sub-critical pressure, which we define to be the highest pressure parameter possible in the model, whilst still maintaining no bleb nucleation. The sub-critical pressure parameter for 0.7% and 2% agar cell contours is plotted against the cells circularity. (2% agar: 160 blebs across 8 cells. 0.7% agar: 101 blebs across 13 cells). Cells migrating under 0.7% agar are typically more polarised, since they migrate with mainly F-actin driven pseudopods, and have few blebbing events. Cell contours used in the model that were extracted from cells under 0.7% agar are shown to require a lower pressure parameter to initiate blebbing. For cells migrating under 2% agar, blebs alone are used to extend the cell front, and blebbing events are frequent. These cells are therefore much more rounded, with circularities close to 1. The small variance is both circularity and sub-critical pressure observed for the contours corresponding to 2% agar conditions suggest that these cells are functioning in a close-to-limit regime. In our previous work, a hydrostatic pressure parameter of 81 Pa was used in the simulation of an artificial, very rounded cell contour. Here, we find the optimum hydrostatic pressure (where model specificity and sensitivity are maximal) for all the contours considered to be in the range 30-100 Pa.

$$sensitivity = \frac{TP}{TP + FN} \tag{4.2}$$

An example of the nucleation of two true positive blebs in the model can be seen in figure 4.3, with the model initialised using a cell contour from migration underneath 0.7% agarose.

4.3.1 ROC curve analysis

For each image contour used to initialise the model, we gradually increased the pressure from the sub-critical value, until a pre-defined upper limit, recomputing the specificity and sensitivity for each pressure parameter value. These were then used to generate receiver operator characteristic (ROC) curves of $1 - specificity$, i.e. the false positive rate, against the sensitivity, or true positive rate. The optimum hydrostatic pressure value was then determined by that which optimised both the specificity and sensitivity; by finding the position on the ROC curve closest to the point (0,1), where all experimental blebs have been predicted by the model, and there are no false positives. (Note that a ROC curve is denoted worthless if it is below the line y = x, since the false positive rate is higher than the true positive rate). Full results tables for the optimum pressure, specificity and sensitivity are included in the appendices.

4.3.2 Summary data

The model summary data for cells under 2% and 0.7% agarose is included in table 1 (30 cell contours for each agarose concentration were analysed). Cells migrating under the 0.7% agarose are shown to have a mean area of 17.6% lower than that for the 2% agarose. However, due to the fact that they are on average twice as polarized, and thus have more distinct protrusions, their cell perimeter is on average 19.6% greater. The larger cell contour length for the 0.7% agarose case provides a considerably higher number of true negatives, and therefore an increased specificity over the 2% agar cells.

The proportion of the model blebs which are false positives in comparison to those which are true positives is significant. (19.91% c.f. 10.45%for the 2% agar, and 20.56% c.f. 4.80%for the 0.7% agar). The number of false negatives is low for both agar concentrations, being only 3.13% of the total model blebs for the 2% agar, and 0.43% for the 0.7% agar.

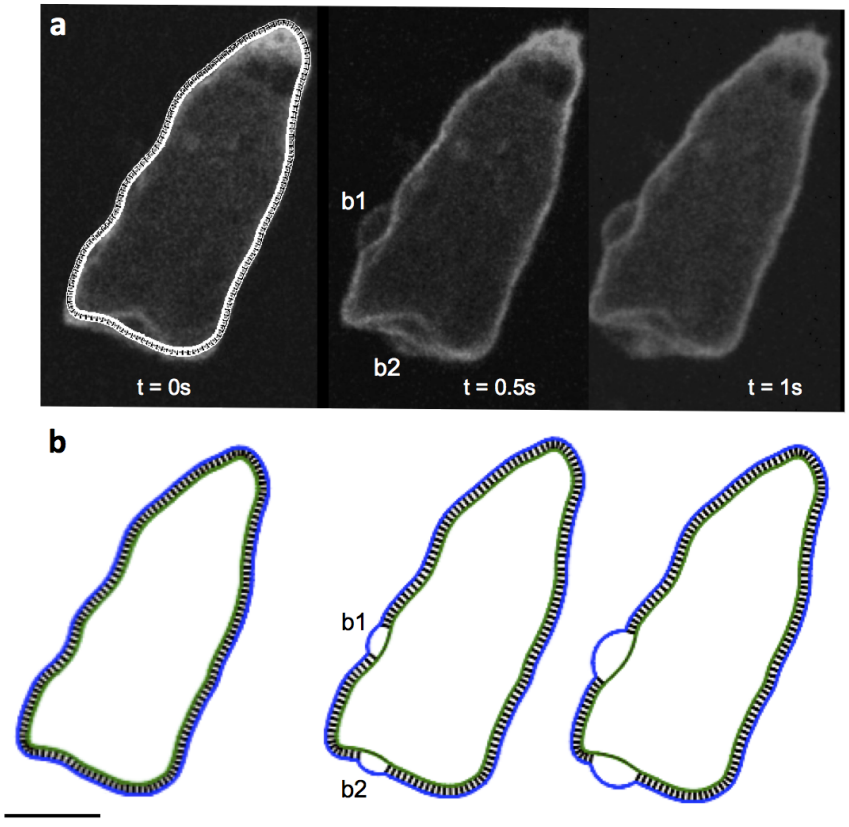

Figure 4.3: (a) Dictyostelium cell contours are extracted from confocal image data using QuimP segmentation. The cells express ABD GFP, an F actin marker. Blebbing regions are seen to leave behind an F actin scar, where the old cortex remains intact. The cell shown here is migrating under 0.7% agar. The time series indicates the rapid speed of bleb expansion in Dictyostelium cells. The nucleation of two blebs is observed experimentally. Scale bars are of length 5 microns. (b) The extracted cell contour is used as the initial geometry in the model, with linkers positioned between the membrane and cortex at equally spaced intervals. All linkers are scaled by a factor of 5 for visual purposes. Model prediction for the sites of bleb nucleation for the given contour, showing two true positive nucleation sites.

Table 4.1: ROC curve summary data

2 % agar	Mean	Std	Coefficient of Variance
Cell Area (um)	168.45	21.93	0.13
Circularity (Degree of Polarisation)	0.82	0.09	0.10
Contour Length	52.78	2.95	0.06
Bleb Diameter	2.96	0.66	0.22
Specificity	0.74	0.19	0.26
Sensitivity	0.71	0.39	0.55
0.7 % agar	**Mean**	**Std**	**Coefficient of Variance**
Cell Area (um)	138.85	32.11	0.23
Circularity (Degree of Polarisation)	0.43	0.09	0.21
Contour Length	65.68	12.07	0.18
Bleb Diameter	2.94	0.59	0.20
Specificity	0.79	0.06	0.08
Sensitivity	0.79	0.36	0.46

As an initial crude fitting procedure, the specificity and sensitivity values obtained from the model are optimistic. Nevertheless, the high numbers of false positives indicated a large scope for development of the model. We later investigate the false positive cases to see if there are any emergent patterns between regions where the model predicts blebs to nucleate that are not experimentally observed, however, we first focus on improvement of the method by which we compare model and experimental results.

4.3.3 Method caveats

Although as a first approach, we see some promising results in terms of model specificity and sensitivity, there are several weak points in the methodology. Firstly, all analysis was performed manually, and thus slow and subject to human bias. Also, due to the considerable time required to manually compare and classify model and experimental blebbing regions, only 30 cell contours were analysed. Secondly, the use of a binary classifier (TP or FP, TN or FN) is not the most suitable tool for understanding a system with inherent stochasticity. We start to address this first in terms of automating the process of identifying the node positions of experimental blebs, which also allows us to match experimental and model bleb positions computationally.

4.4 Automatic bleb tracking (experimental data)

In order for the quantitative analysis of the fit of the model to experimental data to be high throughput and efficient, it was optimal to create an algorithm to automatically detect the node positions of experimentally observed blebs.

For image data of cells migrating through highly resistive environments (2% agarose gel), the classification and automatic detection of blebbing regions was simple, since in this case cells move using only blebs. As bleb expansion is very rapid, blebbing regions can be identified as the areas where the cell has protruded greater than a minimum distance constraint in given time period (thus eliminating any areas where the contour has small-scale outward movement due to segmentation noise or slight membrane fluctuations). We apply a minimum distance constraint of 0.2μm for a single time frame (images recorded at 2 frames per second), and manual checking of the highlighted blebbing regions reveals this method correctly identifies 100% of the experimental blebs, with no false positives. An example of the correct identification of blebbing nodes on the cell contour is given in figure 4.4.

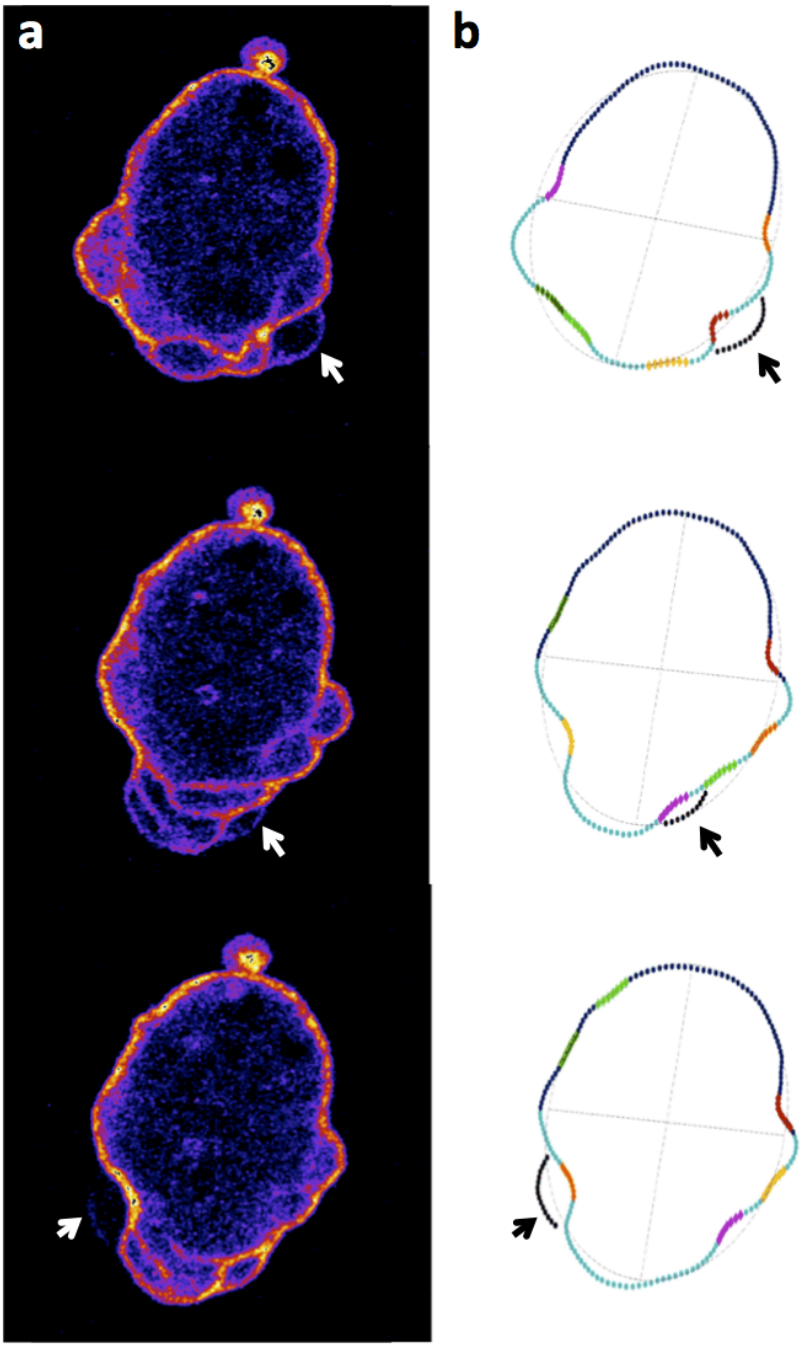

Figure 4.4: Example output of our automatic bleb tracking algorithm. (a) *Dictyostelium* cell expressing ABD-GFP, colour scaled according to fluorescence intensity. The nucleation of experimental blebs are indicated by white arrows. (b) Segmented contours of the *Dictyostelium* cells, with automatically identified blebbing regions indicated by black dotted line in addition to a black arrow. We also indicate the polarisation of the cell, by fitting the contours to an ellipse. The posterior half of the cell is labelled in dark blue, and the anterior half in light blue. The top 6 most likely sites of the model are indicated by the coloured regions, with red being the most likely, and dark green the least likely.

For the case of image data retrieved from cells migrating through low resistive environments (0.7% agarose gel), however, we can no longer rely simply on a distance constraint. Cells chemotaxing under 0.7% agarose migrate using mainly F-actin driven pseudopodia, with a small proportion of blebs. Although bleb expansion is frequently much faster than actin based protrusions, there is a small amount of overlap in the expansion speeds observed for both types of protrusion [ref, richards paper]. This, in combination with the fact that blebs expand to a smaller final size on average than was observed for the cells in high resistive environments, leads to a non-zero error rate in identifying blebbing regions using a minimum distance constraint. This can be resolved by making use of the cortical fluorescence intensity of F-actin around the cell contour. Since the nucleation mechanism of *Dictyostelium* blebs is through membrane detachment from the cortex (as opposed to cortical rupture), blebs initially are devoid of F-actin, such that the cortical fluorescence of ABD-GFP across blebbing nodes is very low. Fluorescence on its own is also insufficient to correctly identify all blebs, with no false positives, as fluctuations in actin fluorescence produce regions with low fluorescence that do not correspond to a bleb. Using both the protrusion speed, and the cortical fluorescence however, we are able to correctly identify 100% of the experimental blebs, with no false positives. We use the spatio-temporal heat maps of cortical ABD-GFP fluorescence and membrane speed, with the criteria that blebbing regions must be both a local minima in cortical fluorescence and a maxima in membrane protrusion speed.

4.5 Hydrostatic pressure as a bleb likelihood gauge

After automating the identification of experimental blebbing regions, we now return to the problem of mapping experimental data onto the model's bleb site predictions in an aims to quantify how well the model performs. We now increase the number of contours we analyse, with 133 for 2% agarose and 100 for 0.7% agarose (the amount of data recorded becomes the limiting factor here, rather than how much we can analyse).

We build upon the previous method of optimizing the hydrostatic pressure parameter, by now using the value of the pressure parameter at which each bleb nucleates to quantify how likely one site is over another. The algorithm we create to employ pressure as a blebbing likelihood gauge is as follows,

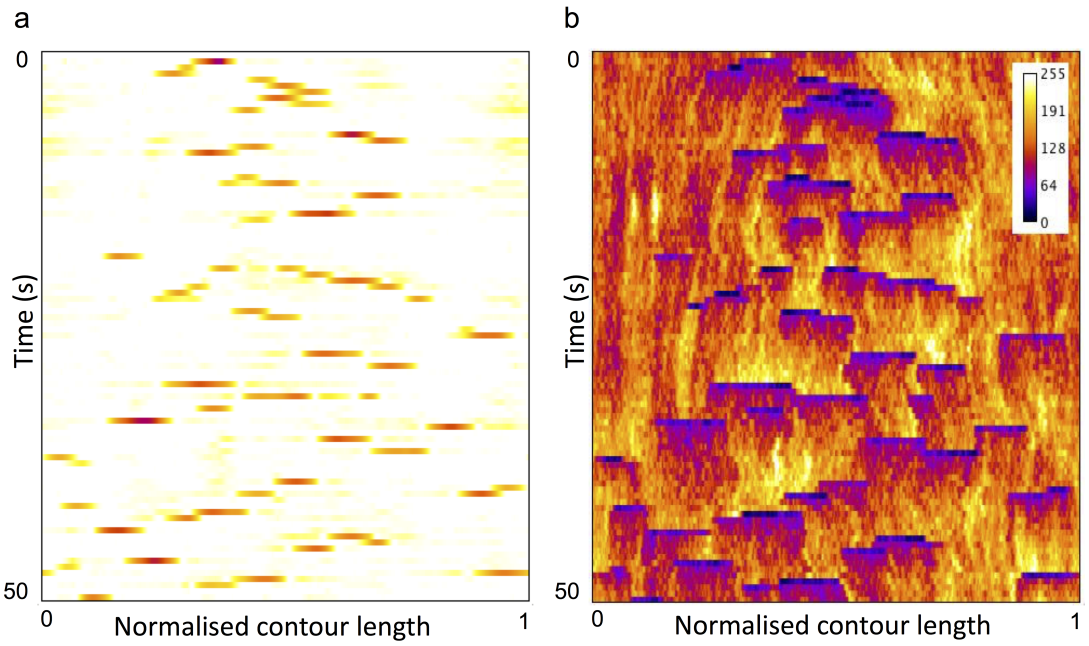

Figure 4.5: Our automatic bleb tracking algorithm for cells migrating in low resistive environments relies on both the motility and fluorescence maps, with the criteria that blebbing regions are both a local minima in actin fluorescence intensity, and a local maxima in membrane protrusion speed. (a) Spatio-temporal heatmap colour scaled according to membrane protrusion speed. (b) Spatio-temporal heatmap colour scaled according to ABD-GFP fluorescence intensity

4.5.1 Algorithm

(i) Model pressure is set to a sub-critical value, P_0 such that no blebs nucleate

(ii) Pressure is incrementally increased by P_{step} until first linker breaks and bleb nucleation begins

(iii) $P_1 = P_{min}$ is the pressure reached at the formation of the first bleb. The corresponding region on the contour is denoted the most likely site for bleb nucleation.

(iv) Pressure is increased again in a stepwise manner until linkers break at a new location (rather than due to continued expansion of the first bleb). $P = P_2$.

(v) We continue to increase the pressure until the whole membrane has detached from the cortex ($P_n = P_{max}$). Results are stored in a matrix containing the order of blebbing regions and the pressures at which they occur.

(vi) The pressure is normalised between 0 (P_{min}) and 1 (P_{max}) to yield P_{NORM}, and the blebbing likelihood parameter is defined to be $1 - P_{NORM}$, such that the site of most likely bleb nucleation is assigned a value of 1.

(vii) Results for each contour are displayed visually using heatmaps, where each node on the cell contour is coloured according to its bleb likelihood parameter.

4.5.2 A threshold value for blebbing: optimising specificity and sensitivity

For each cell contour analysed, the node positions where a bleb is experimentally observed are automatically identified, and the bleb likelihood parameter for the given region is recorded. This process is repeated for all cell contours in each agarose dataset, allowing us to map the experimental data onto the model by generating distributions of the bleb likelihood parameters corresponding to real blebs.

As previously, we classify bleb sites into either TP, FP, TN or FN, but now we use the bleb likelihood parameter (normalised pressure) to threshold the point at which we define a region to be a bleb. For each dataset, 2% and 0.7% agarose, we determine a single threshold value which optimises the specificity and sensitivity for all contours analysed within that dataset, via ROC curve analysis. For a particular cell contour, nodes above the threshold value are defined to be blebs, and subsequently classified into either true or false positives, depending on whether they align with the experimentally

observed blebbing regions. Nodes below the threshold value are defined to not nucleate blebs, and are thus classified into either true or false negatives.

4.5.3 Bleb likelihood parameter distributions

We see from figure 4.6 that the distributions for the bleb likelihood parameter, as determined by normalised pressure, are strongly skewed, indicating that experimental blebs often form in regions of high likelihood as predicted by the model. The model performs better than a consideration of the curvature alone (i.e. computing normalized curvature of the contour, and plotting the distribution of the curvature values at which experimental blebs are observed), since it takes into account the whole geometric landscape. Regions of negative curvature between two highly convex peaks are more likely sites of bleb nucleation than regions of negative curvature with a high positive peak on one side, but a gentle increase in curvature on the other side.

Note that we also generate a test distribution (by random re-sampling), representing the distribution of bleb likelihood parameters we would observe if bleb site selection was random, rather than due to any physical mechanisms or biological regulation. We evaluate whether the distribution of model predictions is significant compared to the distribution we would achieve if bleb site selection was random using chi squared tests. Bonferroni correction is implemented to account for multiple comparisons. The 2% agarose data has high sensitivity since a large proportion of the data is significant compared to the test distribution. The lower threshold on true positives however means that often regions exist above the true positive likelihood parameter, thus leading to false positives, and so a lower specificity. A much smaller proportion of the 0.7% data is significant compared to the test distribution; the model predicts the existence of many likely regions, leading to a lower sensitivity. The high threshold for true positives imposed does however mean we have a low proportion of false positives, and thus a high specificity.

4.5.4 Bleb classification and localisation

Figures 4.8 and 4.9 demonstrates the classification of blebs into true or false positives. Regions highlighted in red are the predicted nucleation sites of the model, above the given threshold criteria. The cells have been fitted to an ellipse, to identify the posterior (dark blue) and anterior (light blue) regions of the cell. Experimental blebs are identified in black, and allow for classification of the model bleb sites into true positives or

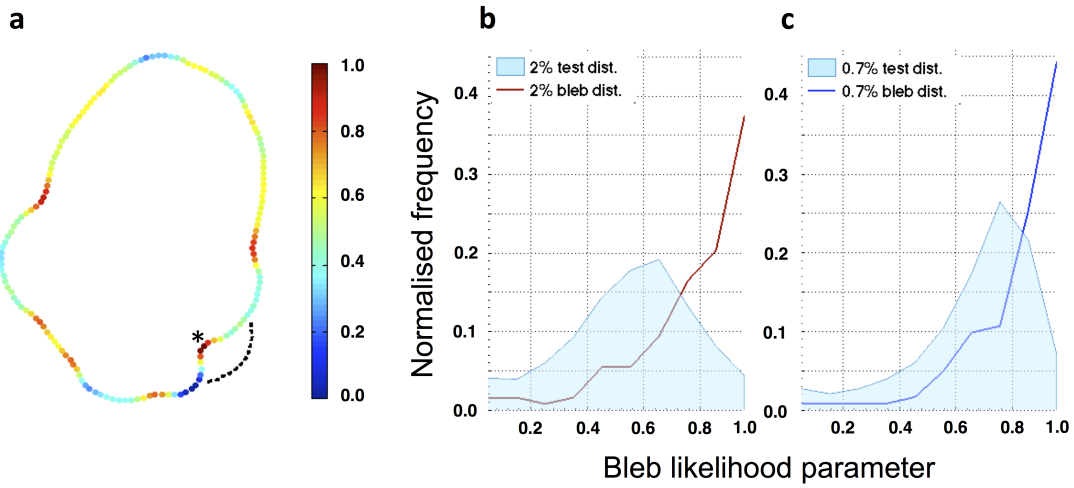

Figure 4.6: (a) Spatial distribution of bleb likelihood parameter (1- normalised pressure at which region blebs). Regions in red are the most likely nucleation sites predicted by the model. The dotted line marks the experimentally observed bleb formed in the next time frame, with corresponding nucleation site indicated by *. (b-c) Distributions for the bleb likelihood parameter at the nucleation site of experimentally observed blebs- marked by red and blue line graphs for 2% agar and 0.7% agar data respectively. Both distributions are strongly weighted towards higher bleb likelihood parameters (lower pressures), indicating that experimental blebs correlate well with the regions of highest nucleation probability predicted by the model. Test distributions are marked by the light blue areas. At higher values of the bleb likelihood parameter, the distance between the test distributions and bleb distributions is large, thus yielding a high significance level when the distributions are compared using χ^2tests. Class widths of 0.1 and Bonferroni corrections for multiple comparisons were used in the analysis.

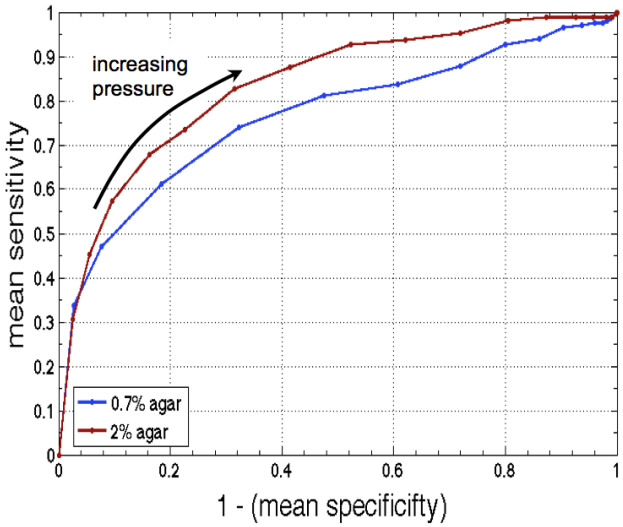

Figure 4.7: ROC curves. True and false positive rates are evaluated for different bleb likelihood parameter thresholds. Contour regions with bleb likelihood parameter above the threshold are considered to be blebbing regions. Regions where both the model and experimental data show blebs are defined as true positives. The model is shown to account for 70% of the observed blebs for 2% agarose data, and 60% of the 0.7% agarose blebs.

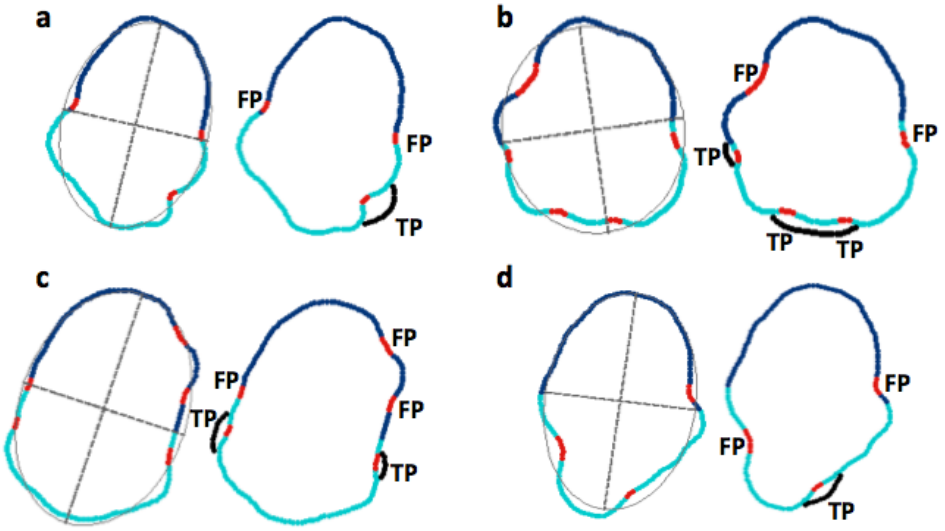

Figure 4.8: Bleb classification for example contours from cells migrating underneath 2% agarose. Posterior region of the cell (dark blue), anterior region (light blue) and predicted nucleation sites (red). Experimental blebs are identified in black, and allow for classification of the model bleb sites into true positives or false positives. The P predicted nucleation sites are regions where the bleb likelihood parameter (1-normalised pressure required to nucleate a bleb in that region) is greater than the determined threshold. A bulk thresholding criteria was used to optimise sensitivity and specificity, such that the likelihood parameter above which blebs are defined to nucleate is the same for all contours of each agarose dataset.

false positives. We notice that many of the false positives are located on the posterior membrane of the cell, a factor that we discuss in more detail in sections 5.2 and 5.3.

4.5.5 Predictive power of the model

Given a time series of cell contours, we can predict the number of blebs to nucleate, and their locations, with 60-70% sensitivity and 80% specificity, based on physical mechanisms alone. Note that these values are based on average properties from the bulk ROC curves- i.e. using the same threshold for every single cell in each dataset. (1 threshold for 2% agar data, and 1 threshold for 0.7% data) The specificity and sensitivity can be considerably improved by optimising the threshold for each individual cell.

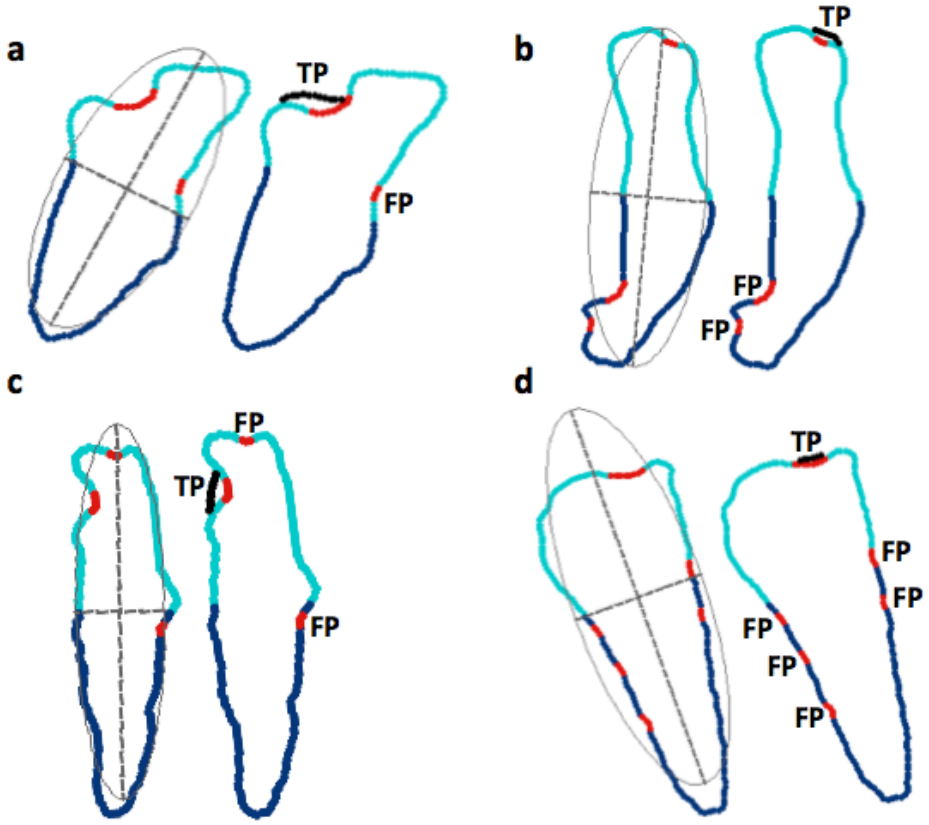

Figure 4.9: Bleb classification for example contours from cells migrating underneath 0.7% agarose. Posterior region of the cell (dark blue), anterior region (light blue) and predicted nucleation sites (red). Experimental blebs are identified in black, and allow for classification of the model bleb sites into true positives or false positives. Many of the false positives are located on the posterior membrane of the cell.

4.5.6 Method caveats

Although we create a method in which we quantify how likely one region is over another, generating distributions of bleb likelihood, we do not make full use of this information, since we again reduce the analysis to that of a binary classifier. We only use the likelihood to threshold the data. Additionally, although we have reduced the level of human bias and increased our efficiency through automating the process of bleb identification and classification, generating the bleb likelihood parameters for all nodes on a contour is still a slow process, since each simulation is run many times at many different pressure parameters. The final method we introduce in this thesis aims to address both of these caveats.

4.6 Linker length as a bleb likelihood gauge

We aim to improve the previous method by making use of the likelihood distributions, not limiting our analysis to specificity and sensitivity.

To assess the quality of bleb site predictions, a measure is required for the likelihood of bleb nucleation in a given region, relative to other regions on the same contour. Here we use the length of linkers to determine blebbing propensity, rather than hydrostatic pressure, since it is computationally more efficient. It is also a more intuitive measure, since linker length is directly linked to bleb formation, in that model blebs nucleate in regions where linkers break due to extension beyond a critical length. Blebbing propensity was determined by computing the evolution of membrane nodes in the model, and changes in linker lengths, according to the governing force balance pde.

4.6.1 Ranking bleb sites

Identification of model nucleation sites

To determine local blebbing propensity, we perform computations at a sub-critical pressure, which is defined as the highest pressure that does not result in linkers breaking and subsequent nucleation of blebs. This reveals regions where linkers are most extended, and therefore more likely to break and nucleate a bleb (figure 4.10 c).

We determine local maxima in the heat maps of linker lengths and rank these sites in order of their bleb nucleation likelihood: The models most likely bleb site corresponds to the longest linker, and is given a rank of 1, the least likely nucleation

site has a rank of n, where n is the number of sites that exist for a given cell.

The local maxima in the linker length distribution computed at the sub-critical pressure yield single node positions for bleb nucleation sites, whilst the width of each bleb site is determined by the distance between the first two local minima on either side of the nucleation site (figure 4.10 d). The nodes corresponding to the whole width of each bleb site all correspond to the same rank.

Mapping experimental data onto the model

We automatically track the positions of experimentally observed blebs, and use the contours from time frames immediately preceding nucleation events as model input geometry, as in the previous method. For a given contour, we identify the position of the experimental bleb observed in the next time frame, and record the corresponding rank for bleb nucleation in that region as predicted by the model (figure 4.10 d). Note that if the location of the experimental bleb covers more than one ranked region, we assign to it the rank of the region it predominantly covers. This procedure was repeated for 160 blebs observed in 133 time frames of 8 migrating cells under 2% agarose and 101 blebs in 100 time frames of 13 cells under 0.7% agarose.

4.6.2 Method advantages

This method is computationally more efficient, since we do not re-run the simulations for a range of parameter values, but rather only once for each contour, at the sub-critical pressure. (Although the simulations are run for a long enough time to reach steady state). We no longer use a binary classifier, but make use of the whole distribution to analyse the performance of the model, see section 5.1

4.7 Method validation

4.7.1 Equivalence of ranked bleb order at sub-critical pressure, and the order blebs nucleate in upon increasing pressure

The likelihood order for bleb nucleation predicted by the model is independent on whether we use linker length or hydrostatic pressure as a gauge for local blebbing propensity.

We demonstrate in figure 4.11 (a-f) that the order of model bleb sites predicted

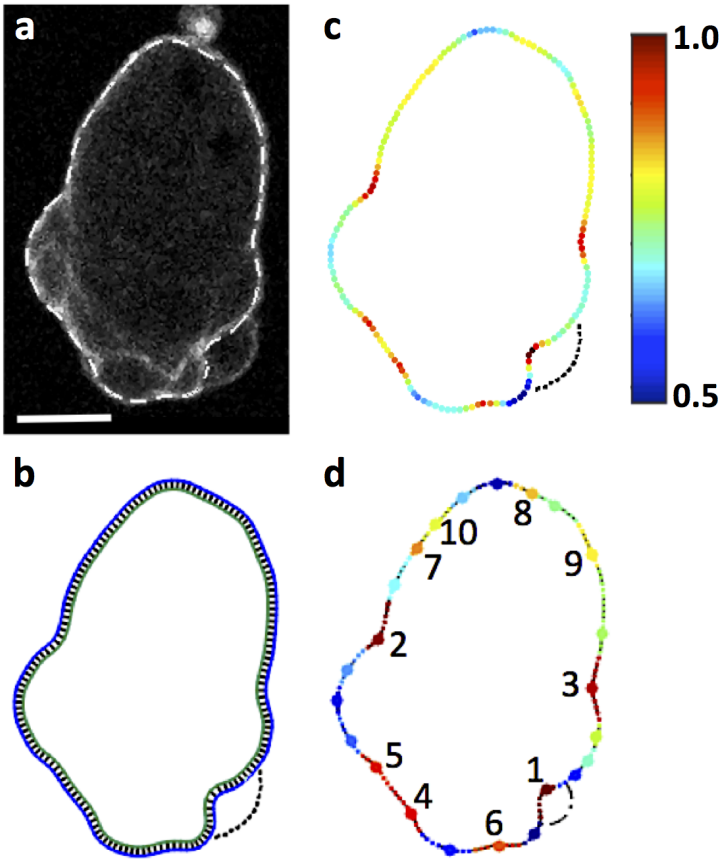

Figure 4.10: Image based model fitting of blebbing in a Dictyostelium cell chemotaxing under 2% agarose a) Blebs leave behind an F-actin scar labelled by ABD-GFP, indicating the position of the old cortex. Dashed line: Cell contour prior to formation of the bleb to the lower right. Scale bar: 5m. b) Initialisation of the model based on the contour in a, with equally spaced linkers positioned between membrane and cortex. Linkers are scaled by a factor of 5 for visual purposes. Dashed line: Position of bleb observed in a. c) Simulation output at sub-critical pressure, which is not sufficient to break linkers and produce blebs. Colours indicate the distribution of linker lengths, from dark blue (relaxed) to dark red (maximally extended), as indicated by the colour bar. Red regions are more likely to nucleate blebs under increased pressure. d) First 10 predicted bleb nucleation sites, ranked in order of likelihood of linkers breaking. Dash-dot line: Outline of most likely model bleb computed at critical pressure.

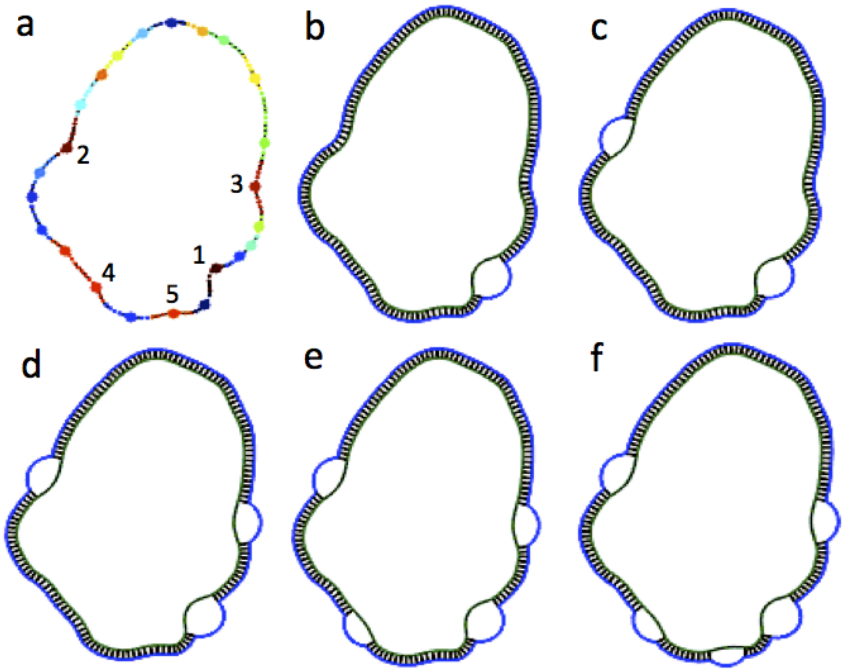

Figure 4.11: Simulated bleb nucleation (a) Model prediction of the likelihood order of regions around the cell contour nucleating a bleb. Bleb sites are ranked based on linker length, with the top 5 sites labelled. Colours indicate the distribution of linker lengths, from dark blue (relaxed) to dark red (maximally extended). (b-c) Simulated bleb nucleation and expansion upon increasing hydrostatic pressure parameter, demonstrating the order of bleb nucleation matches what is predicted based on linker length. The pressure parameters for the simulations are 78Pa, 79Pa, 81Pa, 81.9Pa and 82.5Pa respectively.

by linker length does indeed correspond to the order blebs nucleate in upon increasing the hydrostatic pressure parameter of the system above the critical value.

4.7.2 Robustness of model with respect to node density

We use a node spacing in the model of $0.3\mu m$ since this is sufficient to resolve nucleation events in enough detail, and reduces time to numerically solve the force balance pde, however, it is useful to demonstrate that the model results are independent of node spacing. We run simulations at two additional node spacings, $0.15\mu m$ and $0.075\mu m$ and examine shifts in ranked positions of bleb sites. We define the absolute mean rank difference (MRD) as follows,

$$|MRD| = \frac{sum_{j=1}^{N} C_{i,j} - F_{i,j}}{N} \tag{4.3}$$

where N is the number of contours, C is the coarse grain rank, F is the fine grain rank, and i is the ith bleb site for each contour, j.

Figure 4.12 demonstrates that although some swaps in ranked orderings occur between simulations at different node spacings, this is minimal, with the maximum $|MRD|$ being < 1.5, and with no change in the orderings of the first three most likely sites.

4.7.3 Membrane peeling

The question of how blebs expand without complete 'unzipping' of the membrane from the cortex, whilst maintaining high curvature at their flanks has been investigated by Woolley et al.,[ref woolley 2015] who found that increasing the stiffness of the neck linkers in their model led to phenotypically accurate bleb profiles. Woolley however dismissed this finding as non-biological, and instead suggested mechanisms of global cortical contraction, or local growth of membrane at the bleb (neither yet experimentally validated). Here, we propose that increased stiffness of the neck linkers of an expanding bleb is in-fact a physically meaningful result of mapping a 3D cellular problem onto a 2D model representation. In the true 3D system, as a bleb expands, the number of linkers present surrounding the bleb circumference, and thus the number of linkers required to be broken/detached in order to grow the bleb, increases with each successive increase of the bleb circumference, making rapid membrane unzipping unlikely. In the 2D model representation however, the number of linkers at the bleb boundary is two (one either side), regardless of how large the bleb grows. We therefore increase the stiffness of the bleb neck linkers in our 2D model, in proportion to the number of the linkers they represent, such that

$$\begin{aligned} k_{neck} &= k(r_{bleb}); \\ &= \frac{1}{2} r_{bleb} \cdot ds \cdot \pi \cdot k \end{aligned} \tag{4.4}$$

where k is the linker stiffness, ds is the node spacing, r_{bleb} is the radius of the bleb, and k_{neck} is the computed representative stiffness of each neck linker.

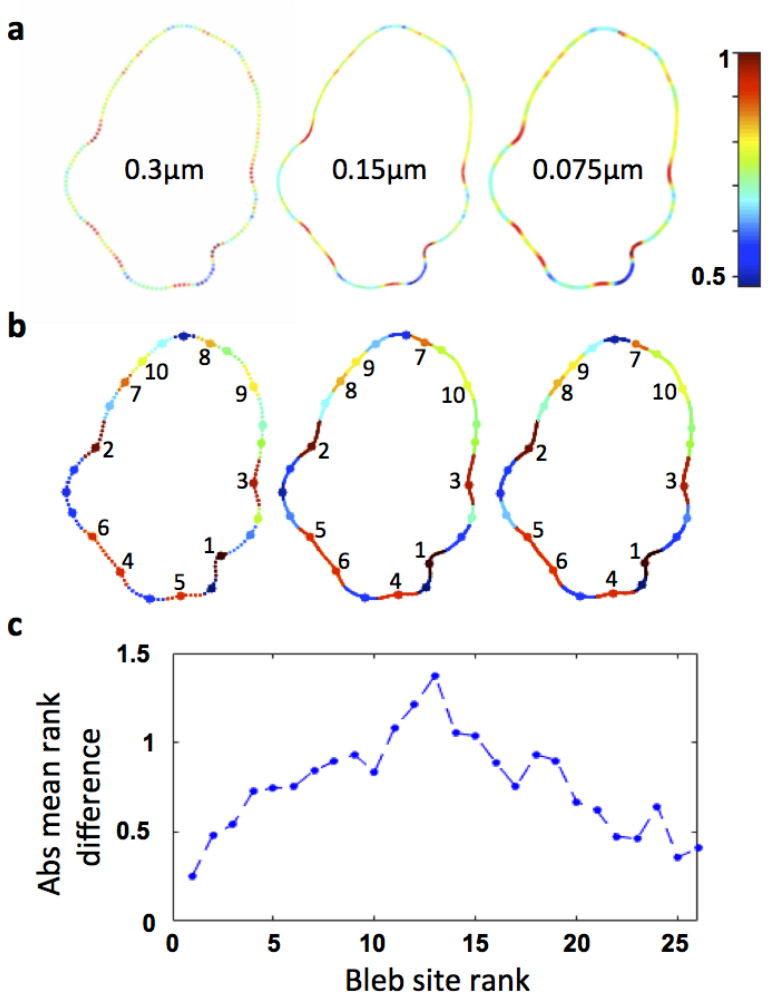

Figure 4.12: (a) Example of the distribution of normalised linker lengths computed at the sub-critical pressure for varying node densities for a single cell contour, colour coded from least extended (blue) to maximally extended (red). (b) First 10 bleb nucleation sites predicted by the model for the same cell contour shown for each corresponding spacing. Order of first three bleb sites remains unchanged. (c) Plot of absolute mean rank difference between coarsest and finest grid spacing, for all contours and all bleb sites, demonstrating minimal reorderings of ranked bleb sites occur, even upon increasing the model node density four-fold. The least reorderings are observed for the most likely and least likely model sites.

Inclusion of this neck stiffness, representative of the 3D system, allows our model to not only recover more phenotypically realistic blebs, but also gives rise to a bleb expansion mechanism whereby the bleb diameter size increases smoothly with increasing contact angle of the bleb, until the point where the strain on the neck linkers is critical, such that further tearing of the membrane from the cell body occurs. This step-wise form of expansion is in good agreement with that experimentally observed by Charras et al. [Charras and Paluch, 2008], as demonstrated in figure 4.13. Such a mechanism is also in agreement with the finding of Alert et al., [Alert and Casademunt, 2016], with membrane peeling governing bleb nucleation and shown capable of strongly enhancing it.

We present the results of our method for predicting the sites of bleb nucleation, based on model linker length, in the subsequent chapter, in addition to comparing our findings for low and high mechanically resistive environments.

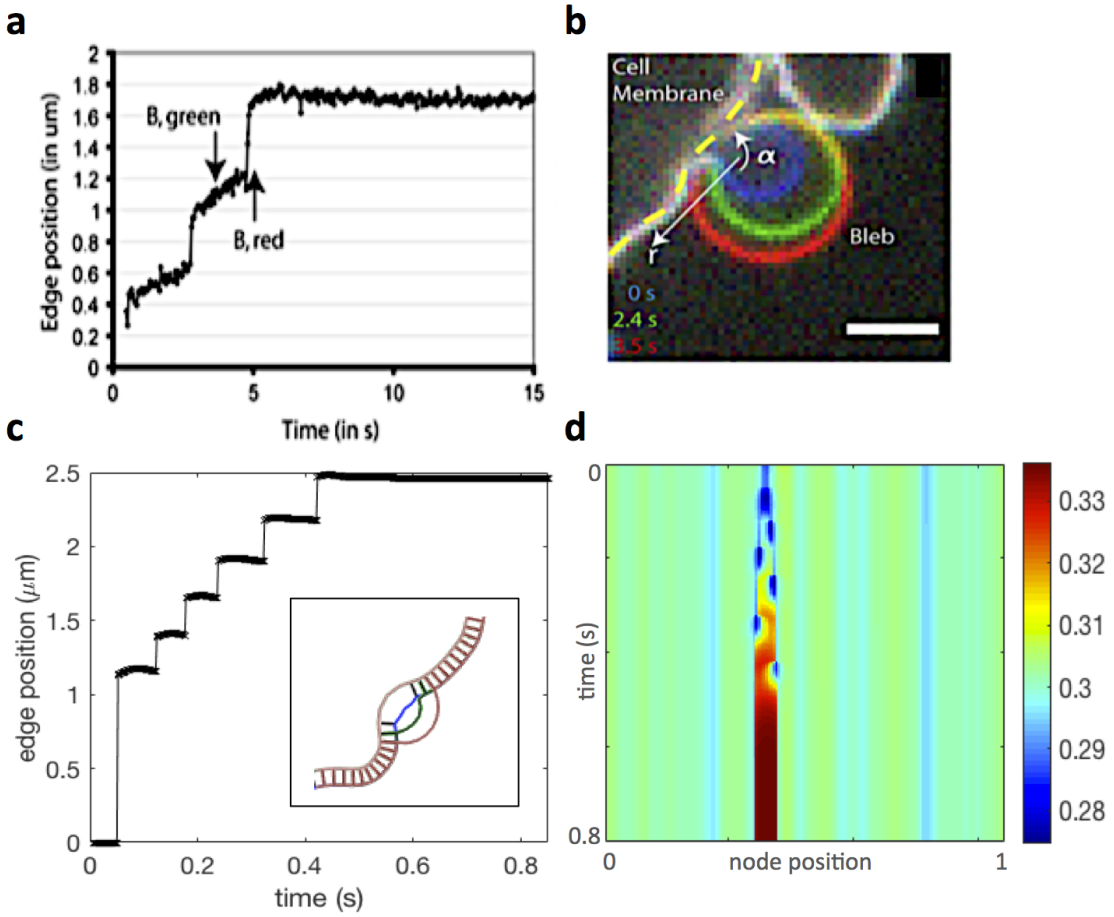

Figure 4.13: Our model demonstrates a stepwise bleb expansion mechanism. After the initial linker breakage and subsequent membrane detachment, intracellular pressure causes the detached membrane to protrude outwards, increasing the strain on the neck linkers. This results in a smooth increase in the bleb diameter, until the point at which the strain on the neck linkers is such that they break, causing a sudden large increase in diameter size as the membrane peels away from the cortex. (a-b) Experimental data from work by Charras et al. [Charras et al., 2008]. (c) Model results demonstrating the stepwise increase in bleb neck diameter over time. Inset: model bleb outline for 3 successive neck breakage events overlayed. (d) Spatio-temporal heat map of node spacing for all points on the cell contour over time, again demonstrating how node spacing at the bleb neck varies in a stepwise manner as it expands

Chapter 5

Low vs high resistance: Is geometry always the determining factor?

5.1 Linker strain as a measure for local blebbing propensity

Figure 5.1 (a,b) shows the frequency distributions of model ranks for experimentally observed blebs (bleb rank distribution, or short, bleb distribution) for cells migrating underneath either 2% or 0.7% agarose overlays. Test distributions (shaded regions) for each agarose dataset were generated by random resampling of ranked nucleation sites, giving the model rank distributions to be expected if bleb site selection was an entirely random process. We use χ^2 goodness of fit tests to statistically compare the observed rank distribution to the expected rank distribution, with class widths of 1, and Bonferroni correction for multiple comparisons.

If geometry were indeed the driving mechanism in the selection of bleb nucleation sites, we would require the χ^2 tests to be statistically significant, with the frequency of observed blebs in the most likely sites predicted by the model much higher than the expected frequency suggested by the test distribution. Additionally we would require the least likely sites predicted by the model to coincide with a lower than expected frequency of experimental bleb sites.

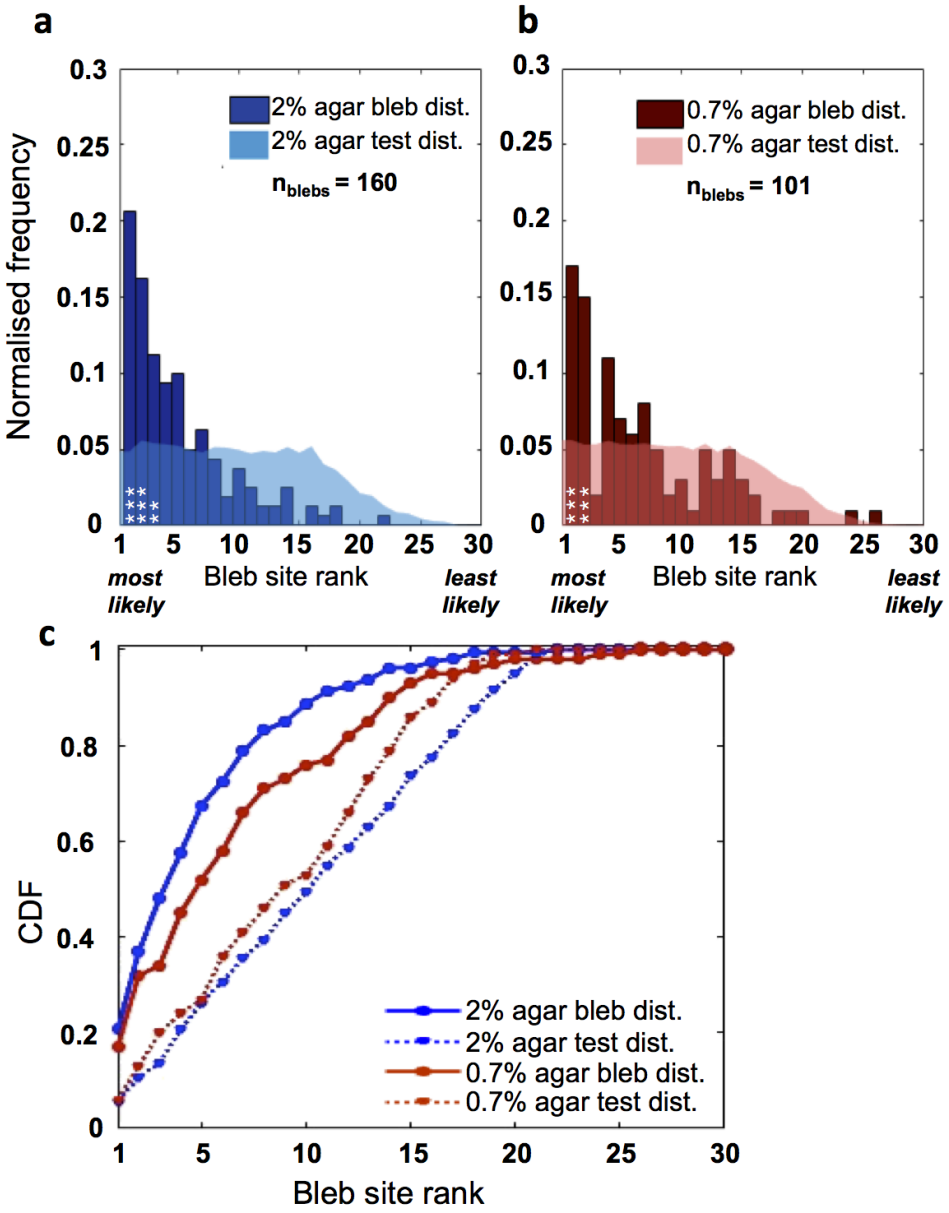

Figure 5.1: Bleb sites are not distributed randomly. (a-b) Frequency of observed blebs plotted against model bleb site rank, with test distributions assuming blebs are randomly distributed shown in lighter colours (Blue: 2% agarose, 160 blebs across 8 cells; red: 0.7% agarose, 101 blebs across 13 cells). Both distributions are strongly weighted towards the most likely ranked sites predicted by the model, where differences to the test distributions are significant on a level of 0.001 (bins marked *** , χ^2 test, class widths of 1 with Bonferroni corrections for multiple comparisons). (c) Cumulative distribution function (CDF) demonstrate that the majority of experimentally observed bleb sites are captured within a relatively small proportion of model likelihood ranks, and are clearly not distributed randomly. The CDF curve for 2% agarose is shifted up and to the left compared to the 0.7% agarose data (under-curve areas of 82.48% and 75.60%, respectively), showing that the original model predicts bleb site selection in a highly resistive environment better (Theoretical maximum: 100% if all observed blebs would be predicted by the most likely model bleb site).

The bleb distributions for both agarose data sets were indeed found to be significantly better than the test distributions (p-values: 3*10^-25 for 2%; 8*10^-6 for 0.7%), with the 2% data having a greater number of significant bins than the 0.7% data. In addition, for both agarose concentrations, the highest frequency of experimentally observed blebs coincides with the most likely nucleation site predicted by the model.

Cumulative distribution function (CDF) plots show that the majority of experimental bleb site locations are captured within the top few most highly ranked bleb sites produced by the model (figure 5.1 c). Comparing the areas under the CDF curve for each dataset to the area of the theoretical maximum, where 100% of the experimental blebs observed nucleate from the most likely model site, enables us to estimate the predictive power of our model. For cells migrating under 2% agarose, this area is 82.37% of the theoretical maximum area, compared to 75.60% for the 0.7% agarose data.

Our results therefore show that cell geometry is a good predictor of where blebs will form in chemotaxing Dictyostelium cells, especially for cells migrating in highly resistive environments.

5.2 Low resistive environments: additional mechanism required to restrict likely bleb sites to the cell front

We next investigated the cases where the models predictions break down, especially why it performs better with cells under 2% compared to 0.7% agarose. The microscopy movies show two major differences between cells in the two conditions:

(i) Cells under 2% agarose are much rounder than those under 0.7% agarose, and in particular have a pronounced round tail (circularity difference $p < 0.001$, Mann Whitney U test; figure 5.3)

(ii) the chemotactic orientation of experimental blebs is superior in cells migrating under 0.7% agarose, with 88% of blebs nucleating in the front half of the cell compared to 74% under 2% agarose (figure 5.2).

Examining further the morphology of contours for cells migrating underneath 2%

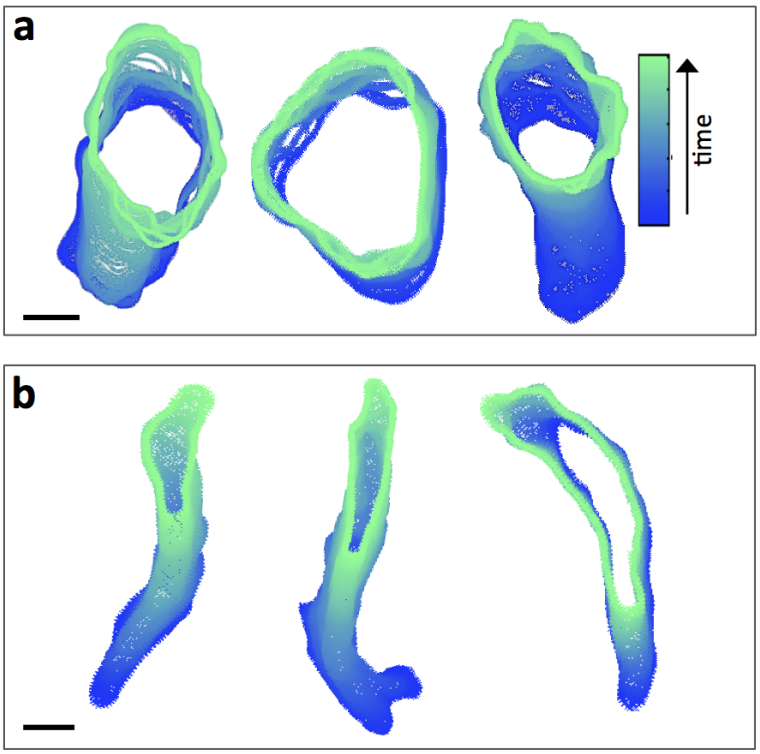

Figure 5.2: Observed front-rear gradients in blebbing are predicted by the original model for cells under 2% agarose, where blebs are suppressed at the round cell rear. In elongated cells under 0.7% agarose additional mechanisms are required.Contours of cells migrating under 2% agarose cells are rounder (a), under 0.7% agarose more elongated (ab), with differences in circularity being significant

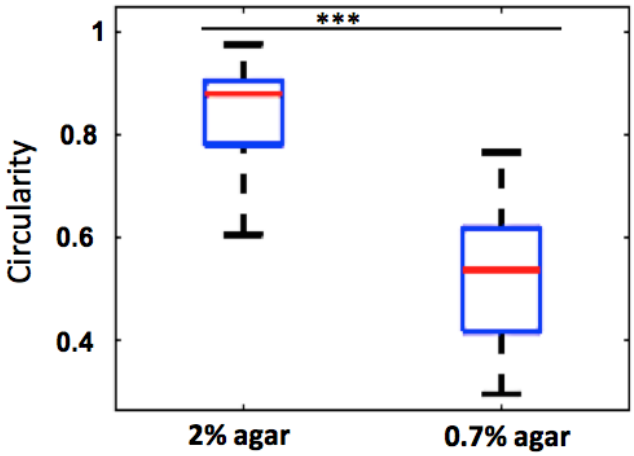

Figure 5.3: Boxplots of cellular circularity for cells migrating under 2% or 0.7% agarose.We observe a significant difference in the circularity between low and high resistive environments, with cells migrating under 2% agarose being much more rounded than those under 0.7% agarose. Mann Whitney U-test, p value ¡ 0.001

agarose reveals that the front and rear of the cell are geometrically distinct (example contour, figure 5.4 c, left). For a single time frame of an image sequence, without prior knowledge of which direction the cell is moving in, the front of the cell is easily identifiable, based on geometry alone. Since the nucleation likelihood of bleb sites in the model are driven by differences in local cellular geometry, with the positive curvature of the highly rounded cell rear disfavouring blebbing, the model is able to produce an asymmetric blebbing propensity profile when applied to such contours. Indeed, for cases where the model is initialised using contours from cells migrating in highly resistive environments, polar histograms for the angular distribution of the top 3 most likely nucleation sites predict 63.4% of blebs to lie in the front half of the cell (figure 5.4 a,b).

For cells migrating underneath 0.7% agarose however, we see that the front and rear of the cell are not geometrically distinct (example contour, figure 5.4 c, right). Both the pseudopod and the uropod have positive curvature, and disfavour blebbing, whilst negatively curved regions (likely sites for bleb nucleation) are more evenly distributed around the cell contour than compared to the 2% data. The polar histograms of the top 3 most likely bleb sites for cells migrating in low resistive environments thus predict that 50% of blebs will form in the front half of the cell. The model is therefore not able to reproduce the strong asymmetry observed in experiments (88% in front).

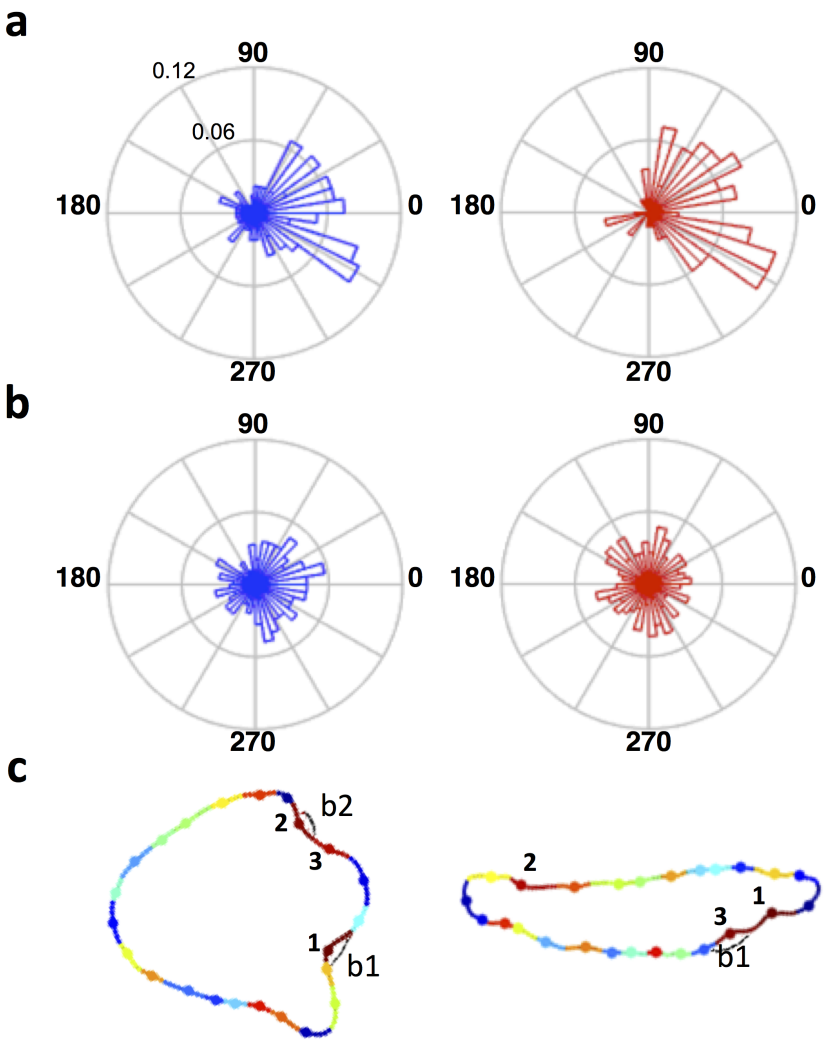

Figure 5.4: (a) Polar histograms of the angular position of experimental bleb nucleation sites around the cell contour confirm that blebs are more frequently observed in the front half of the cell (88% of blebs under 0.7% (red) and 74% under 2% agarose (blue)). (b) Distribution of the top 3 likely bleb sites predicted by the model. The original model based on geometry alone is sufficient to generate a gradient in blebbing activity under 2% agarose, with blebbing suppressed at the round cell rear (63.4% of blebs in the front). Under 0.7%, however, the distribution is homogeneous (50.3% at the front), suggesting additional mechanisms to direct blebs to the front. (c) Representative model outputs for a cell under 2% agarose (left) and 0.7% agarose (right) demonstrating this effect: Under 2% agarose the 3 most likely (red) regions are at the front. Under 0.7% agarose red labelled regions can be also seen at the cell rear, contrary to what we observe experimentally.

We conclude that there must be an additional mechanism in elongated cells migrating in low resistive environments that acts to either promote blebbing activity at the cell front, or decrease the bleb nucleation likelihood at negatively curved regions at the rear of the cell.

5.3 Uropod retraction and protrusion retractions affect local blebbing propensity

We recall from section 5.3 that a gradient in the density of membrane to cortex linkers was a strong candidate for polarising bleb formation in *Dictyostelium* cells. It has been shown by Tsujioka et al. that myosin-II was required for the posterior localization of the linker proteins, with talin enriched in the cell rear (although it is important to note that only cells migrating in buffer were considered, with blebbing motility not investigated, and with the density distribution of talin not quantitatively analysed). For chemotaxing *Dictyostelium* cells, we observe a recruitment of myosin-II to the cell rear, to generate cortical contraction and retraction of the back of the cell (Appendix, figure 1). Linker proteins connecting the membrane and cortex are required for force transmission between the two layers, such that active retraction of the cortex also retracts the membrane. As demonstrated by the polar histograms in figure 5.4, experimental blebs are rarely observed at the rear of the cell, where myosin-II driven retraction of the uropod occurs.

Although blebs are often not retracted when used as a migratory mechanism, we also investigate cases where bleb retraction is observed (28 cases in all image sequences analysed). Blebs create regions of strong negative curvature on their flanks as they expand, which are likely sites of nucleation for new blebs. Under 2% agarose conditions, where cells move using only blebs, blebs are frequently observed to nucleate on the flanks of previous blebs (we will refer to these as daughter blebs). However, for the 28 cases where blebs were retracted, no daughter blebs were observed to nucleate on their negatively curved flanks. We show an example in figure 5.5 where two experimental blebs are retracted, and whilst we demonstrate with contour colour scaling of model blebbing propensity, that the flanks of these blebs are sites of high bleb nucleation likelihood, no blebs are seen to nucleate in these regions.

We therefore suggest that the spatial distribution of linker proteins is indeed

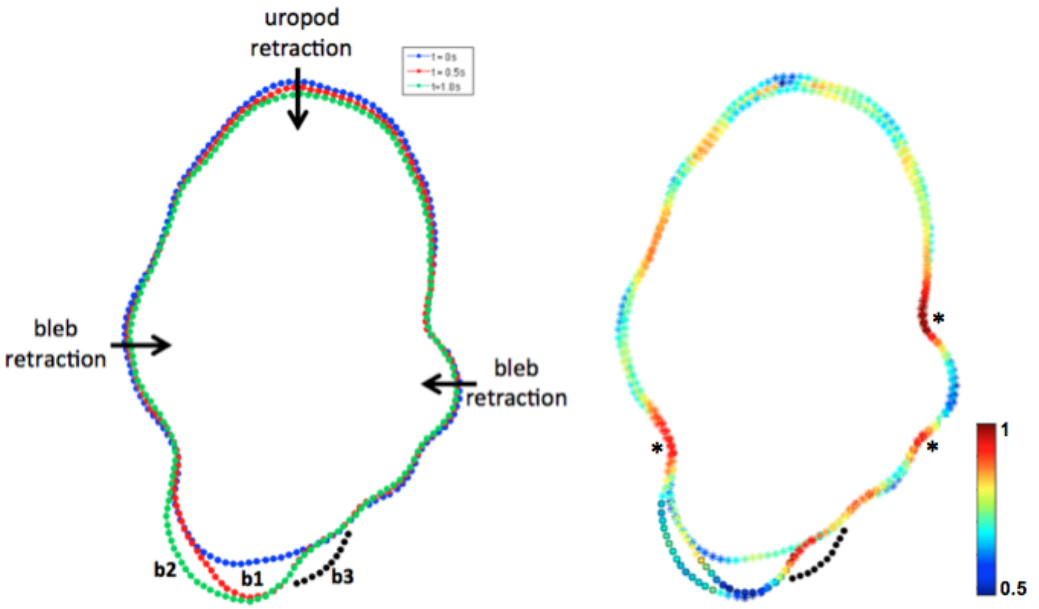

Figure 5.5: Uropod and protrusion retractions influence blebbing propensity. Here we show four successive time frames of a cell migrating underneath 2% agarose, demonstrating the nucleation of three experimental blebs at the front of the cell. We include the same contours coloured according to bleb nucleation likelihood as predicted by the model, colour scaled from most (red) to least (blue) likely. We note that very likely sites predicted by the model, that exist across a retracting region are not observed to nucleate blebs (indicated by *)

closely coupled with myosin-II activity, with areas of increased linker density coinciding with regions of retraction, to aid in efficient force transmission, and reducing membrane detachment likelihood/ unproductive blebbing down-gradient of the chemoattractant. We continue in the next chapter to probe whether a distribution in membrane to cortex linker proteins exists in *Dictyostelium* cells migrating in mechanically resistive environments, and if this could be the additional mechanism required to reduce blebbing propensity across the rear of the cell.

Chapter 6

The influence of talin localisation in bleb polarisation

6.1 Motivation

As discussed previously (section 5.3), an asymmetric spatial distribution of the linker protein TalinA is a likely mechanism for polarising blebbing activity in chemotaxing *Dictyostelium* cells. However, the relation between Talin localisation and bleb site location has not yet been investigated. We therefore created a TalinA reporter (details in section 3.9) to allow us to determine whether a graded distribution in TalinA localisation is present in cells migrating under agarose, and if so, to quantitatively analyse the fluorescence intensity profile, and to examine the correlation with blebbing frequency.

6.2 Talin knock-out cells bleb profusely

If the spatial distribution of TalinA is indeed responsible for reducing blebbing likelihood at the cell rear, and promoting blebbing at the cell front, we would expect cells devoid of Talin to have poor migration efficiency, with blebs not limited to the cell front. Here we observe TalinA/B- double knockout cells (a kind gift of M.Tsujioka to the Kay lab) in buffer, both in vegetative and aggregation competent stages of the social amoeba lifecycle. Figure 6.1 (a1-a3) demonstrates that the vegetative cells in buffer are highly rounded and do not attach to the underlying substrate. Cells cannot crawl due to the lack of attachment, however, blebbing protrusions are still observed. Aggregation competent cells in buffer are shown in figure 6.1 (b1-b3) and exhibit many more blebs than wild-type cells in buffer, in addition to producing long tubular blebs reminiscent of lobopodia.

Due to the attachment deficiency of Talin knockout cells, the under agarose assay utilised for promoting blebbing motility cannot be used, since the cells are incapable of forcing their way underneath the gel. In order to still visualise the knockout cells in a mechanically resistive environment, we developed a modified under agarose setup, whereby a thin agarose layer is lowered onto cells shortly after aspirating the majority of liquid media. Figure 6.1 (c1-c3) shows examples of aggregation competent Talin knockout cells under agar, where again, long tubular bleb protrusions are observed, as well as classic hemi-spherical blebs, neither of which are limited to the cell front.

6.3 TalinA spatial distribution: enrichment at the cell rear

After transformation of the *Dictyostelium* TalinA/B- knockout cells with TalinA-mNeon, we observe a full phenotype rescue, most apparent by the recovery of cell-substrate attachment capability.

We observe a clear asymmetric distribution in the fluorescence intensity of TalinA-mNeon in aggregation competent cells randomly migrating in buffer (figure 6.2). Interestingly, in vegetative cells, we observe a recruitment of TalinA-mNeon to the periphery of macropinosomes (figure 6.3).

6.4 Talin enrichment is inversely proportional to blebbing frequency

An enriched TalinA-mNeon cell posterior is also observed in cells chemotaxing under agarose, as shown in figure (6.4 a1,b1). To analyse this in detail, we segmented cell outlines, and extracted cortical fluorescence intensities, thus allowing us to visualise cell contour plots over time, colour coded according to normalised fluorescence (figure 6.4 a2,b2).

Figure 6.5 shows the collective TalinA-mNeon fluorescence profiles plotted against the angle along the cell polarisation axis (3 cells for each agarose concentration, 30 time points per cell). A striking spatial gradient of TalinA-mNeon is observed in both low and high resistive environments, which exponentially increases from front to rear of the cell (R^2 values for an exponential fit to the data are 0.83 and 0.77 for 0.7% and 2% agarose respectively).

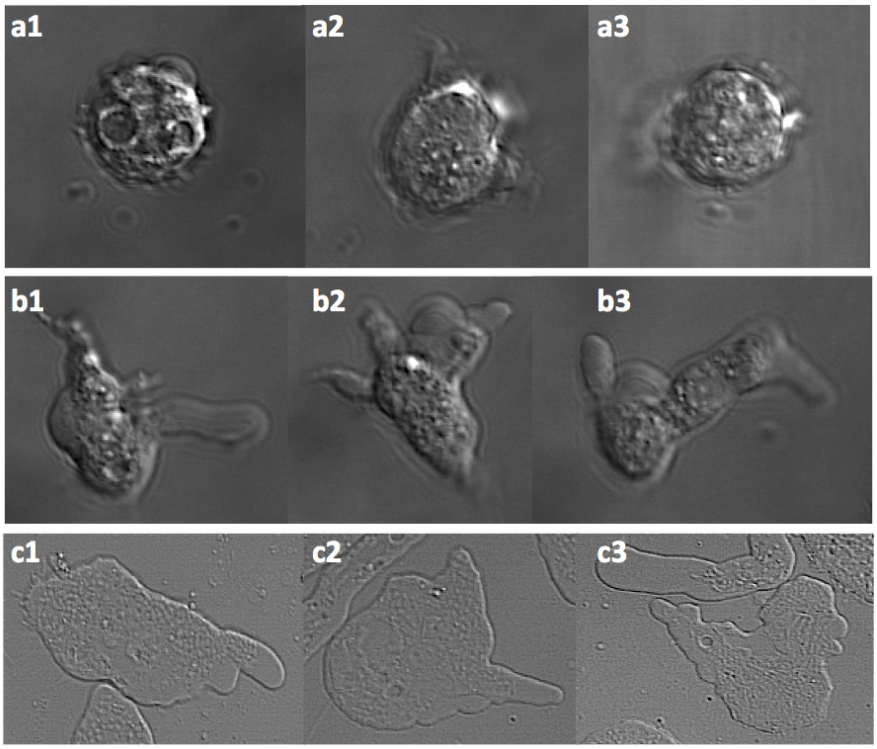

Figure 6.1: Morphology and migration efficiency of TalinA/B- knockout cells differs greatly from that of wild type Ax2 cells. (a1-a3) Vegetative TalinA/B- cells in buffer are seen to have a very rounded morphology and do not attach to the substrate. (b1-b3) Early development stage TalinA/B- cells in buffer still exhibit poor attachment to the substrate. Long bleb-like protrusions are often observed to extend towards neighbouring cells. (c1-c3) Early development stage TalinA/B- cells under agar. The cells are much flatter due to compression by the agar. Long bleb-like protrusions as well as classic spherical blebs are observed to nucleate very frequently. The migration efficiency of the knockout cells under agar is very poor due to (i) lack of proper rear retraction, (ii) many non productive blebs at the sides and rear of the cell and (iii) retraction of protrusions leads to multiple blebbing events on the flanks of the retracting region.

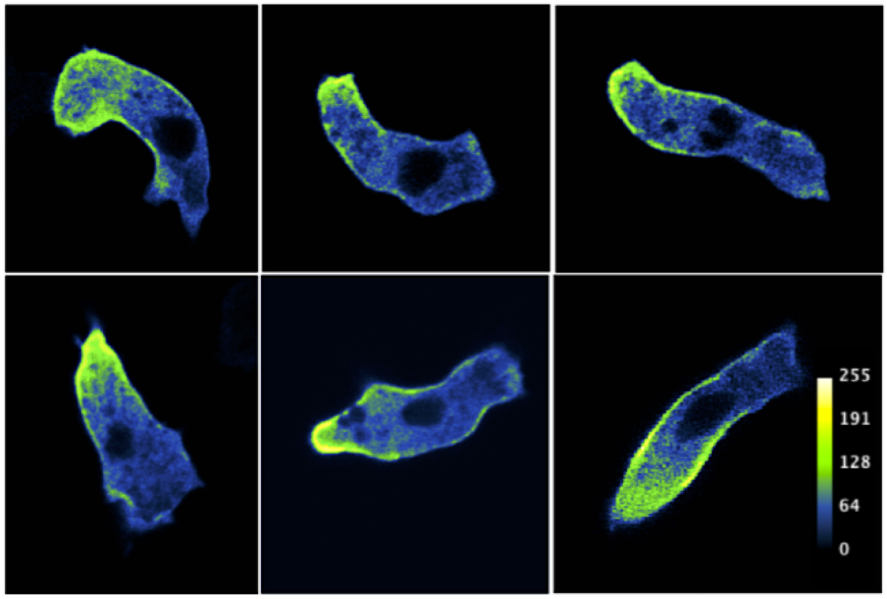

Figure 6.2: A striking asymmetric gradient is observed in the spatial distribution of TalinA-mNeon fluorescence for *Dictyostelium* cells randomly migrating in buffer. Images were recorded by laser scanning confocal microscopy (LSCM) at 2 frames per second. Images are colour scaled according to fluorescence intensity.

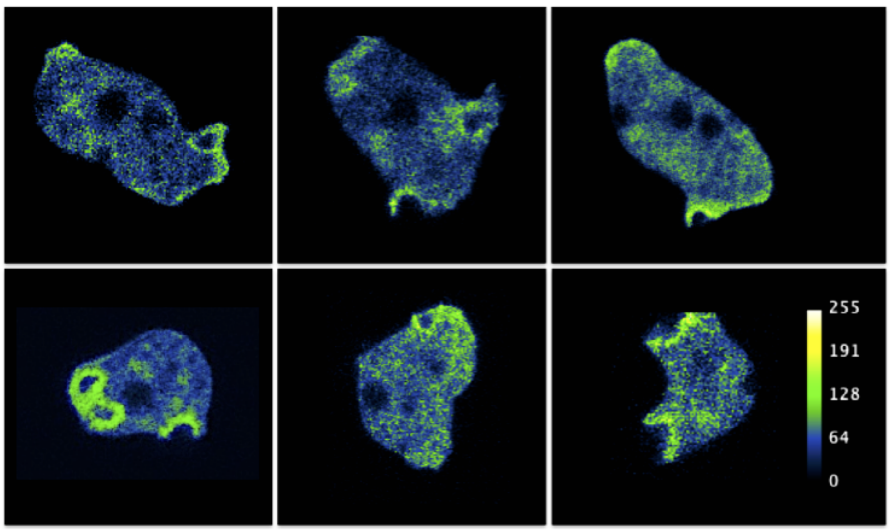

Figure 6.3: In vegetative *Dictyostelium* cells, we see that TalinA-mNeon localises to the edge of macropinocytic cups. Images are colour scaled according to fluorescence intensity.

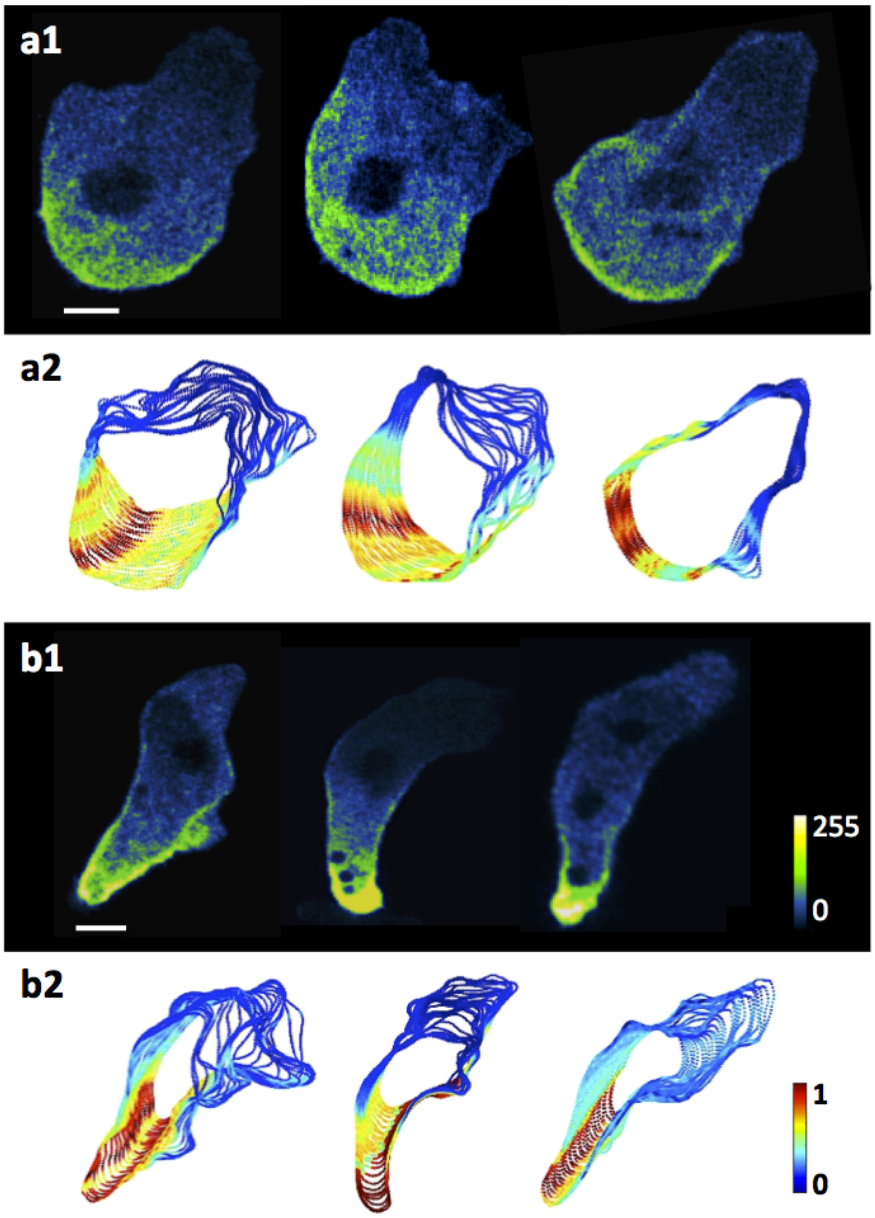

Figure 6.4: TalinA gradients correlate with front-rear gradients in blebbing activity. (a1) Dictyostelium cells chemotaxing under 0.7% agarose, with TalinA-mNeon primarily enriched in the cell rear. (a2) Corresponding cell contours for 30 time points recorded at 2 frames per second, colour scaled according to fluorescent intensity normalised for each cell (blue: low, red: high). (b1, b2) Graded distribution of TalinA-mNeon observed under 2% agarose. Bars: 5 microns.

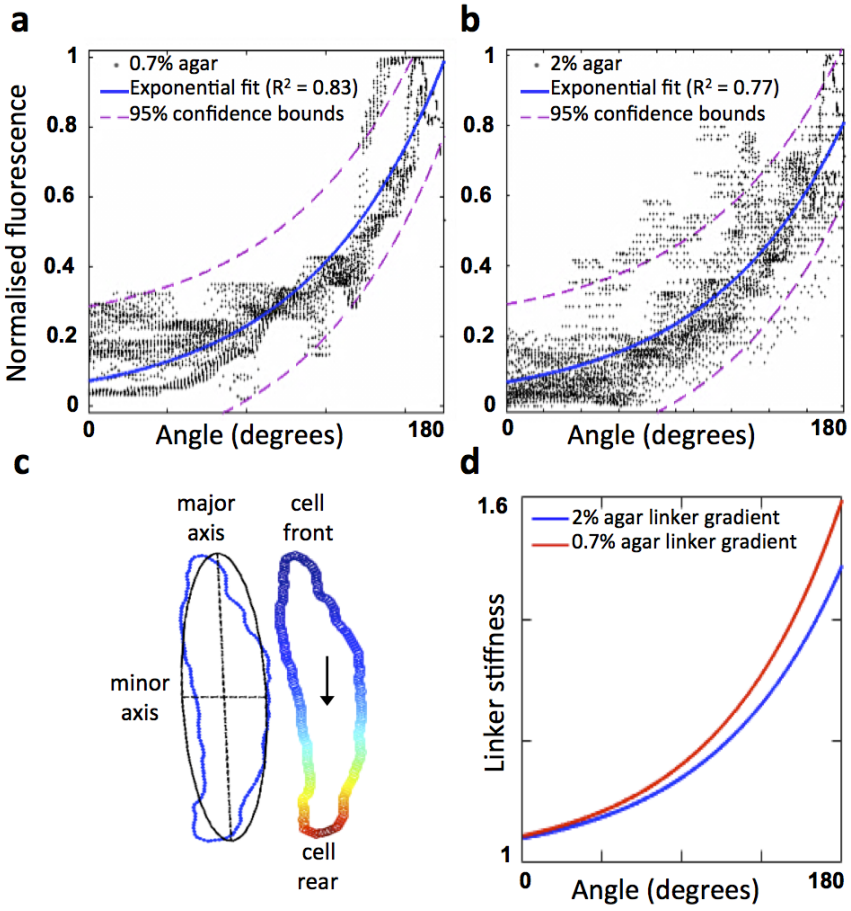

Figure 6.5: (c1-c2) Combined fluorescence profiles for the 3 time series shown in a2, b2, plotted against angular position around the cell contour, with 0o defined as the cell front. TalinA-mNeon fluorescence increases exponentially from cell front to rear (0.7% agarose, R2=0.83, 2% agarose, R2=0.77). (d-e) In the model we translate observed TalinA-mNeon distributions into gradients in membrane to cortex linkage strength, along the polarization axis of the cells. We use a maximum of 60% increase in linker strength between the very front and rear of the cells, as measured in micropipette aspiration assays [Merkel et al., 2000].

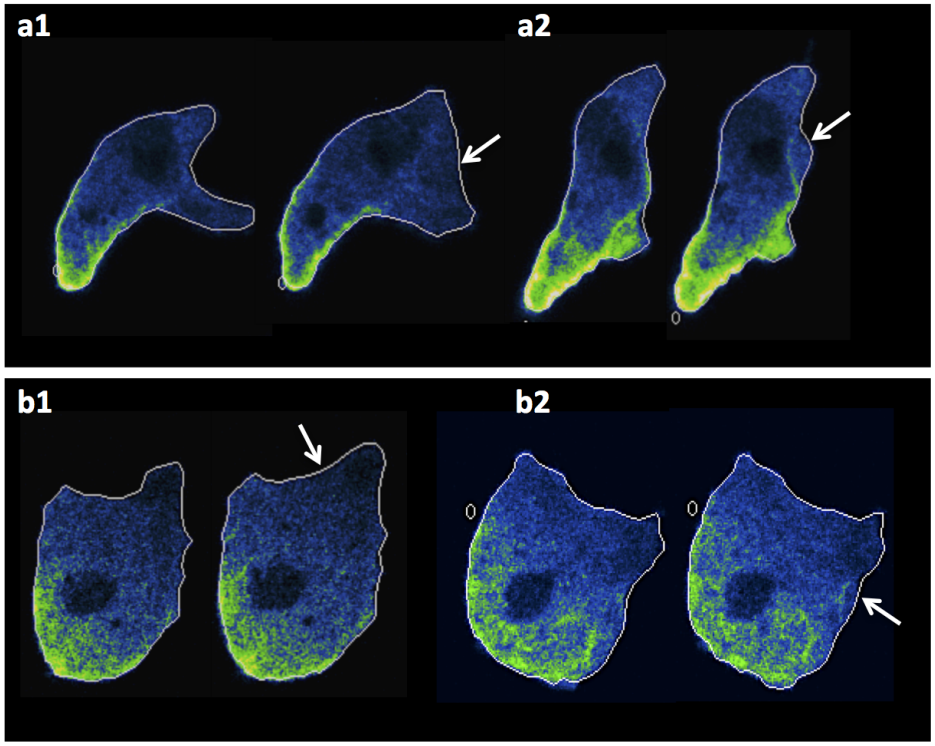

Figure 6.6: Blebs are observed to nucleate in regions of low Talin-A (a1-a2) Dictyostelium cells chemotaxing under 0.7% agar, expressing a TalinA-mNeon construct. Blebs are observed to nucleate at the front of the cell, where there is little Talin, and not observed to form at the cell rear where Talin-A is enriched. (b1-b2) Examples of bleb nucleation in cells chemotaxing under 2% agar. Again, blebs are seen to nucleate in regions where Talin-A is not enriched. Images recorded at 2 frames per second.

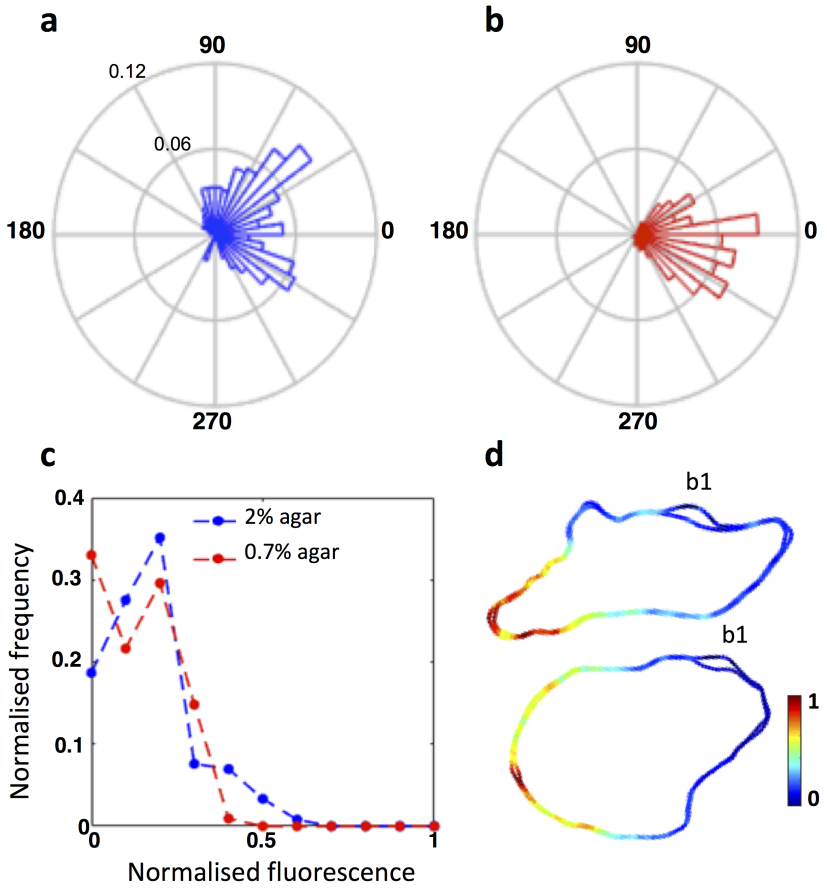

Figure 6.7: (a,b) Polar histograms of the angular distribution of experimental blebs, for the cell contours shown in figures a2 and b2, demonstrate that blebs are indeed directed towards the cell front. (2% agarose data, blue; 0.7% agarose data, red.) (c) Histograms for the observed bleb frequency against normalised TalinA-mNeon fluorescence clearly show that blebs do not nucleate in the regions of highest TalinA-mNeon. (2% agarose rank correlation coefficient, -0.80, 0.7% agarose rank correlation coefficient, -0.85). (d) Example contours with automatically detected bleb sites indicated by b1, colour scaled according to fluorescent intensity normalised for each cell (top, 0.7% agarose cell, bottom, 2% agarose cell).

Blebbing events in TalinA-mNeon expressing cells are demonstrated in figure 6.6. Angular histograms for the experimentally observed blebs over the 30 time points clearly demonstrate that blebs are directed to the cell front where the TalinA-mNeon fluorescence is lowest (figure 6.7 a,b). In addition, histograms for the experimental bleb frequency, binned according to TalinA-mNeon fluorescence, explicitly show that blebs do not occur in regions of maximal Talin accumulation (figure 6.7 c), which we have already seen coincides with the rear of the cells. The blebbing frequency negatively correlates with TalinA-mNeon fluorescence, with rank correlation coefficients of -0.80 and -0.85 for the 2% and 0.7% agarose datasets respectively. Thus we conclude that the areas of highest blebbing activity coincide with areas of lowest Talin and vice-versa. (To aid visualisation, automatically detected bleb examples for each agarose concentration are included in figure 6.7 d.)

6.5 Inclusion of a linker stiffness gradient greatly improves model fit for cells moving in low resistive environments

Figures 6.5 a,b show that the normailsed Talin fluorescence may be approximated by an exponential fit with Talin decaying from the cell rear to the cell front, however in order to apply this exponential fit to the model we first require a means by which to calibrate Talin fluorescence to linker strength. Here we incorporate work by Merkel et al. which showed that the threshold pressure required to detach membrane from cortex in aspiration assays was 60% higher at the rear compared to the front in wild type *Dictyostelium* cells, whereas this difference was abolished in Talin null cells [Merkel et al., 2000]. In line with the observed distributions of Talin and utilising a maximum increase of 60% in linker strength at the rear of the cell, we modified our model to include an exponential gradient in linker stiffness (figure 6.5 c,d).

Figure 6.8 a-c show the resulting bleb distributions and CDF plots for the 2% and 0.7% experimental datasets. For both datasets, the proportion of experimental blebs observed at the models most likely bleb site clearly increases. The Talin gradient greatly improves the 0.7% data, with the area under the CDF curve increasing from 75.60% to 83.07% compared to the theoretical maximum. On the contrary, the already good performance of the geometry-based model on the 2% data remains unchanged.

The spatial distributions of the 3 most likely bleb sites (figure 6.9 a1,a2) show that inclusion of the linker gradient efficiently directs the most likely sites of bleb nucleation to the cell front. We next compare the corresponding cumulative angular frequency plots (figures 6.9 b1,b2) to the experimental bleb frequency plots, and the model sites predicted by geometry alone. This shows that the initial geometry based model matches the 2% agarose data much better than the 0.7% data (Kuiper test p values for the null hypothesis that the distributions are the same for 2% data compared to the model: $0.005 \leq p < 0.01$, and for 0.7% data compared to the model: $0.001 \leq p < 0.002$. Circular statistics toolbox, MATLAB). Upon inclusion of the linker gradient, the shape of the cumulative frequency of the top 3 model bleb sites for 0.7% agarose much more closely represents the spatial distribution of the experimental blebs (Kuiper test p value for the distributions being the same: $p > 0.1$).

Our work therefore provides strong evidence that a graded linker distribution acts in tandem with physical geometry dependent mechanisms to influence bleb site selection.

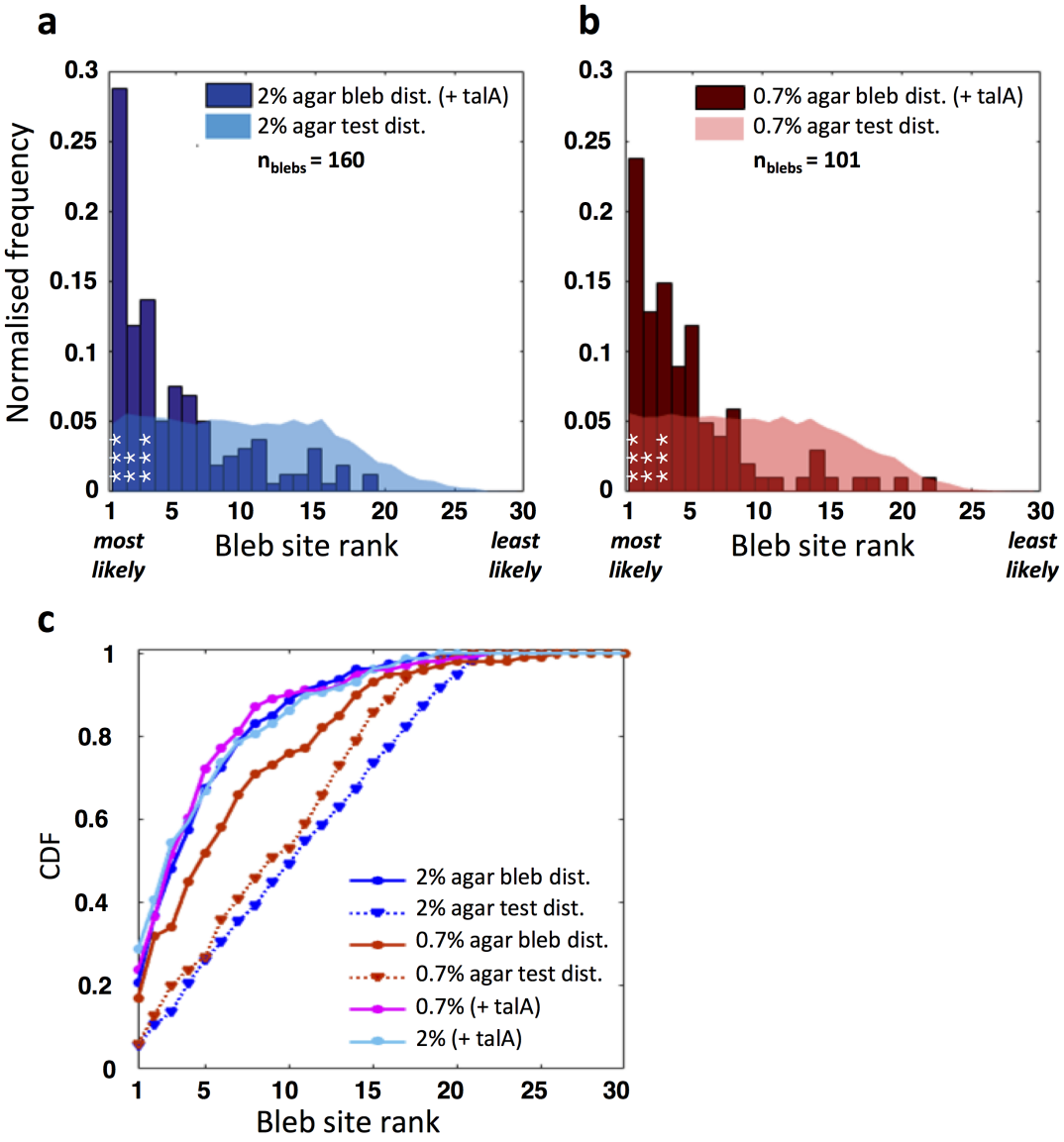

Figure 6.8: Inclusion of an exponentially graded distribution in cortex membrane linker strength greatly improves model performance for elongated cells chemotaxing in low resistive environments (0.7% agarose). (a-b) Frequency of observed blebs plotted against model bleb site rank, with corresponding test distributions in lighter colours (Blue: 2% agarose, 160 blebs across 8 cells; red: 0.7% agarose, 101 blebs across 13 cells). Bins marked *** indicate where differences to the test distributions, which assumes blebs are randomly distributed, are significant on a level of 0.001 (2 test, class widths of 1 with Bonferroni corrections for multiple comparisons). (c) Cumulative distribution functions (CDF) demonstrate that including gradients in linker strength result in much improved performance for 0.7% agarose data, with the updated CDF curve shifted up and to the left. A larger proportion of the experimental data is captured within a smaller number of model bleb sites, thus increasing the predictive power. Areas under the curve increase from 75.60% to 83.07% for the 0.7% agarose cells, whereas for 2% cells, the difference is marginal, with under curve areas of 82.37% compared to 82.48%.

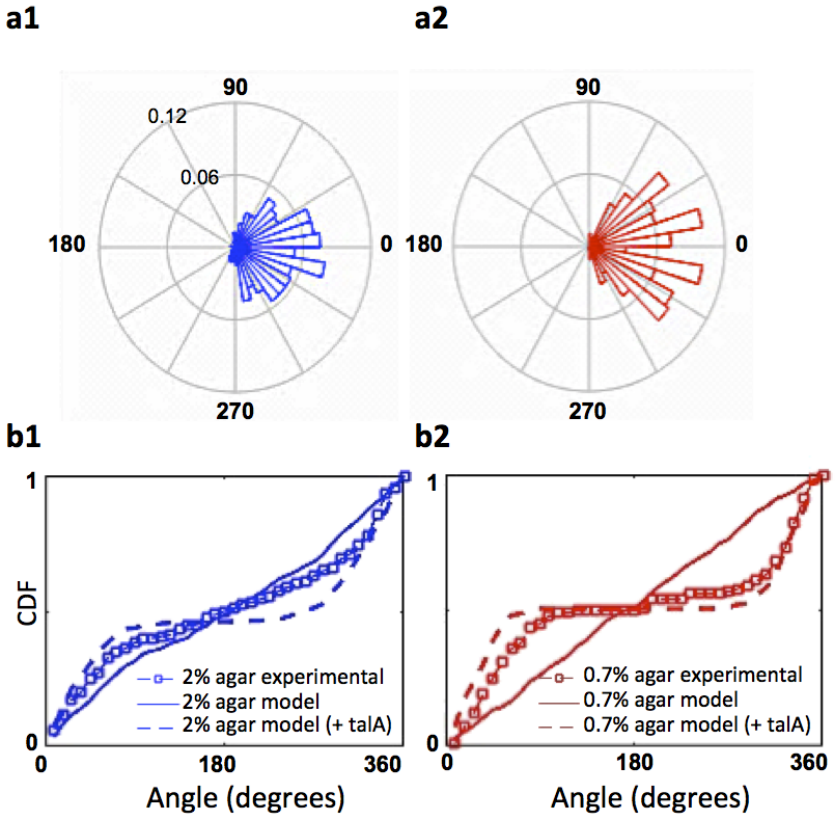

Figure 6.9: (a1-a2) Angular distributions of the 3 most likely bleb sites predicted by the model after inclusion of the gradient in linker stiffness, blebs are now seen to be efficiently directed towards the cell front. (91% and 95% of bleb sites in the cell front for 2% and 0.7% data respectively). (b1-b2) Cumulative frequency plots of the angular bleb distribution of experimental blebs compared to the top 3 model bleb sites both before and after inclusion of the linker stiffness gradient, for each agarose concentration.

Chapter 7

Ongoing work

7.1 Multi-blebbing

7.1.1 Motivation

Regions of strong negative curvature are generated on the flanks of an expanding bleb, these are likely sites for the formation of further blebs, which we refer to as daughter blebs. Daughter blebbing is particularly important in cells migrating underneath 2% agarose where cells migrate using only bleb driven motility, whereas for cells migrating under 0.7% agarose blebbing events are less frequent, thus daughter blebbing is rarely observed.

7.1.2 Characteristic time delay observed before the nucleation of daughter blebs

In an earlier version of our method for predicting bleb site selection (section 4.5.4), it was noted that a large number of false positives (blebs predicted by the model but not observed experimentally) were located in the regions of negative curvature adjacent to existing blebs. However, examination of the image sequences revealed that these were in fact often delayed true positives, where the nucleation of a daughter bleb experimentally is rarely observed in the immediately subsequent time frame to the nucleation of the parent bleb. (Note: the bleb site predictions of the earlier model were assessed as either a true positive or false negative based on the following experimental time frame).

We suggest that the reason for this time delay could be related to the build up of actin at the freshly blebbed membrane, and subsequent recruitment of linkers to the

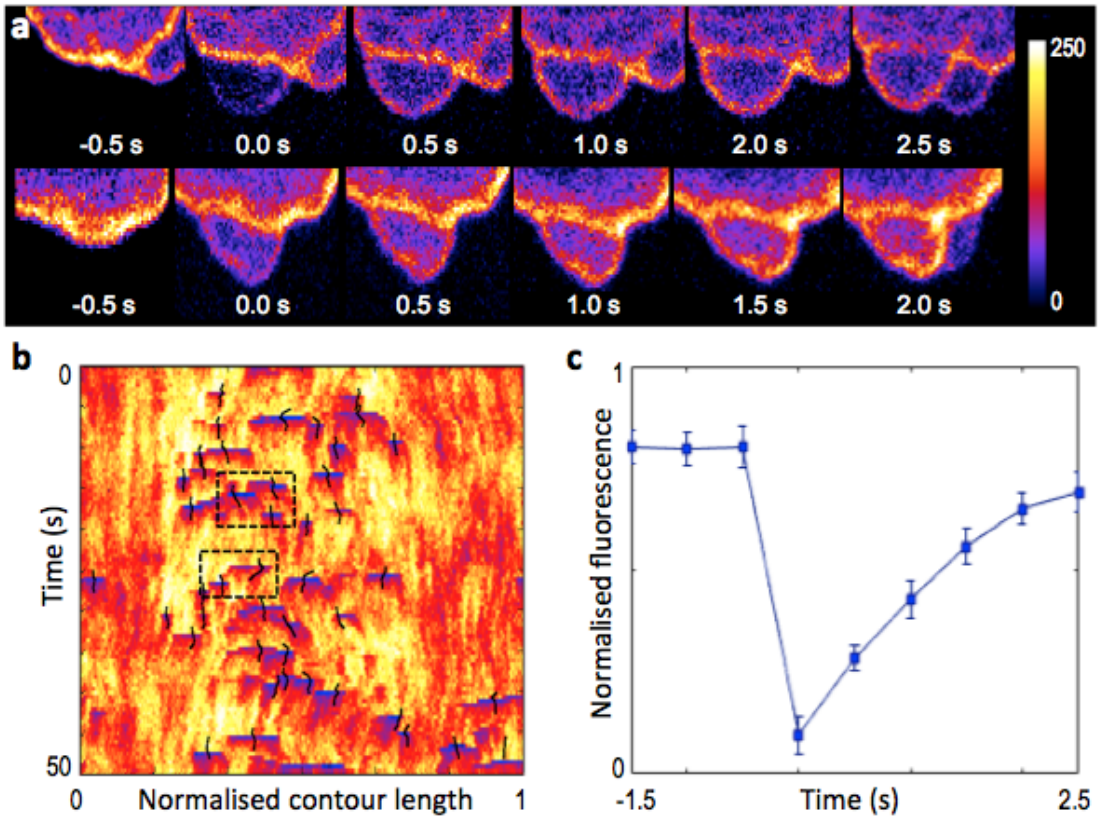

Figure 7.1: (a) Two sequences showing curvature induced blebbing of daughter blebs which appear after a delay of 2-2.5 seconds. (b) Spatio-temporal heatmap colour scaled according to ABD-GFP fluorescence intensity showing blebbing events devoid of F-actin with a subsequent recovery of actin. c) QuimP analysis software makes it possible to track blebs and extract temporal actin profiles.

newly formed cortex. At t=0 where a parent bleb nucleates, likely bleb sites exist on its flanks. However we do not observe the formation of a daughter bleb until a new actin cortex (with recruited linkers) is polymerised. The delay in daughter bleb formation is demonstrated in figure 7.1 for two blebbing cases.

7.1.3 Possible mechanisms for multi-blebbing: daughter blebbing vs. lobopodia

As discussed, following a bleb event, there is a time delay to establish a new cortex and recruitment of linkers, this time delay allows for strong linkage of the membrane to the cortex and allows the formation of distinct daughter blebs to either side of the parent

bleb (figure 7.2 c)

An alternative type of multi-blebbing can be demonstrated using the model for cases where only weak linkage is established, or where the time delay is relatively short such that only a small proportion of linkers have been recruited to the parent bleb (figure 7.2 b). In cases where the linkage between the bleb apex and the newly formed cortex is too weak to withstand the increase in strain resulting from the initialisation of a daughter bleb, the linkers may instead break across the entire region. This alternative type of multi-blebbing would then result in outward expansion of the bleb similar to the development of lobopodia, indeed this would fit with evidence from the literature that lobopodia are formed in a stepwise manner, with cortex left behind at each stage. Furthermore this form of multi-blebbing would suggest that mutant cells with linkage deficiencies would often form lobopodia, which we have observed to be the case with TalinA/B- knockout cells.

The linkage over the whole surface of the parent bleb is weak such that even if the points of initial detachment are at the bleb neck, the linkage across the bleb apex is too weak to withstand the strain required to maintain the high curvature of distinct daughter blebs, therefore instead breaking everywhere, resulting in outward expansion of the bleb similar to the development of lobopodia.

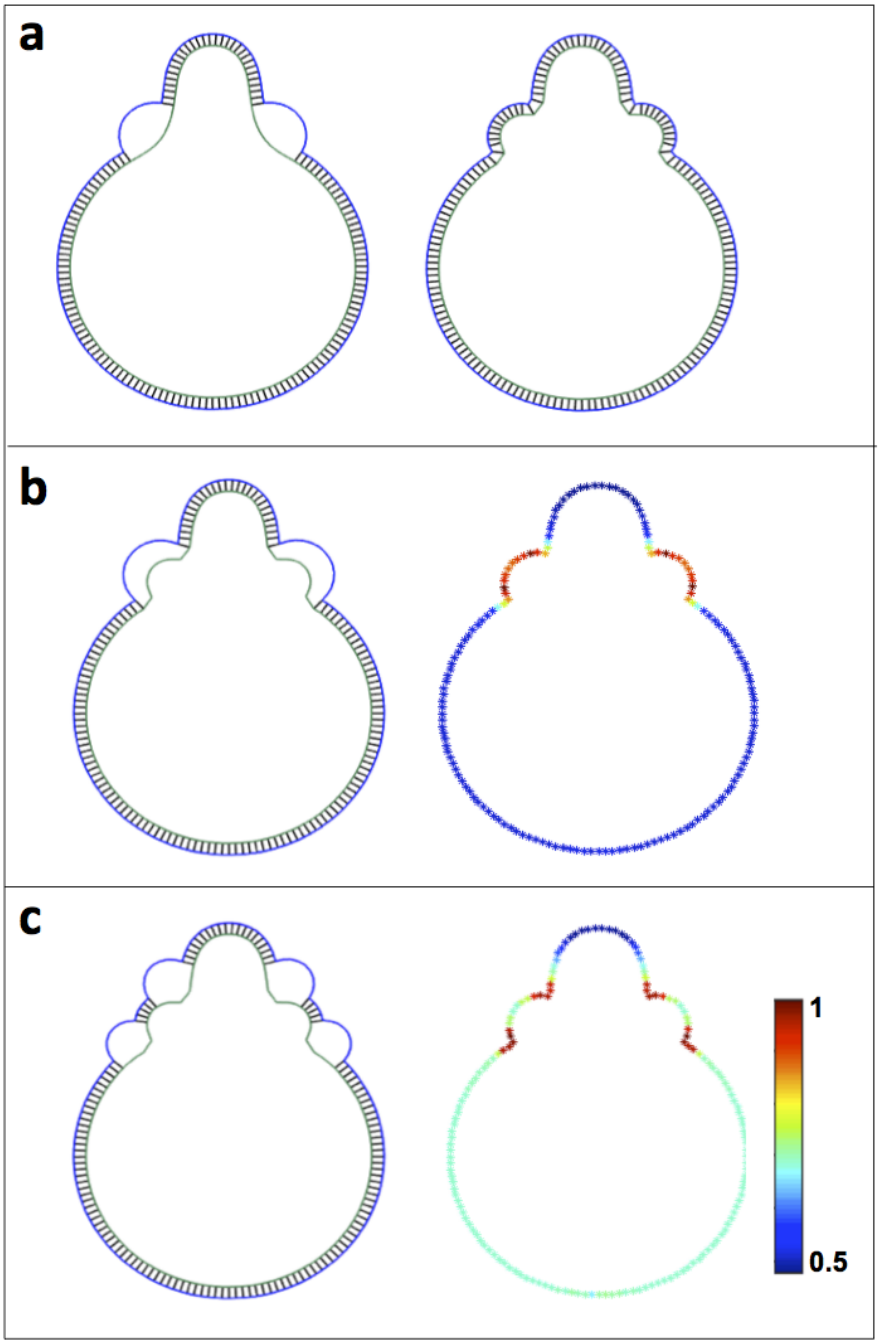

Figure 7.2: (a) Left: Model initialised using simplified cell geometry, and showing the nucleation of two blebs. Right: We rebuild the actin cortex at the blebbed membrane, and reconnect linkers. (b) Left: For cases where the new linkage is weak, the whole region detaches from the new cortex, resulting in further outwards expansion of the first bleb. We suggest that this could be the mechanism for generating lobopodia (tubular blebs), in agreement with experimental results that show that lobopodia form with a stepwise build up of actin. Right: Linker strain heatmap. (c) Left: For cases where the new linkage is strong, the nucleation of distinct daughter blebs is possible. Right: Linker strain heatmap.

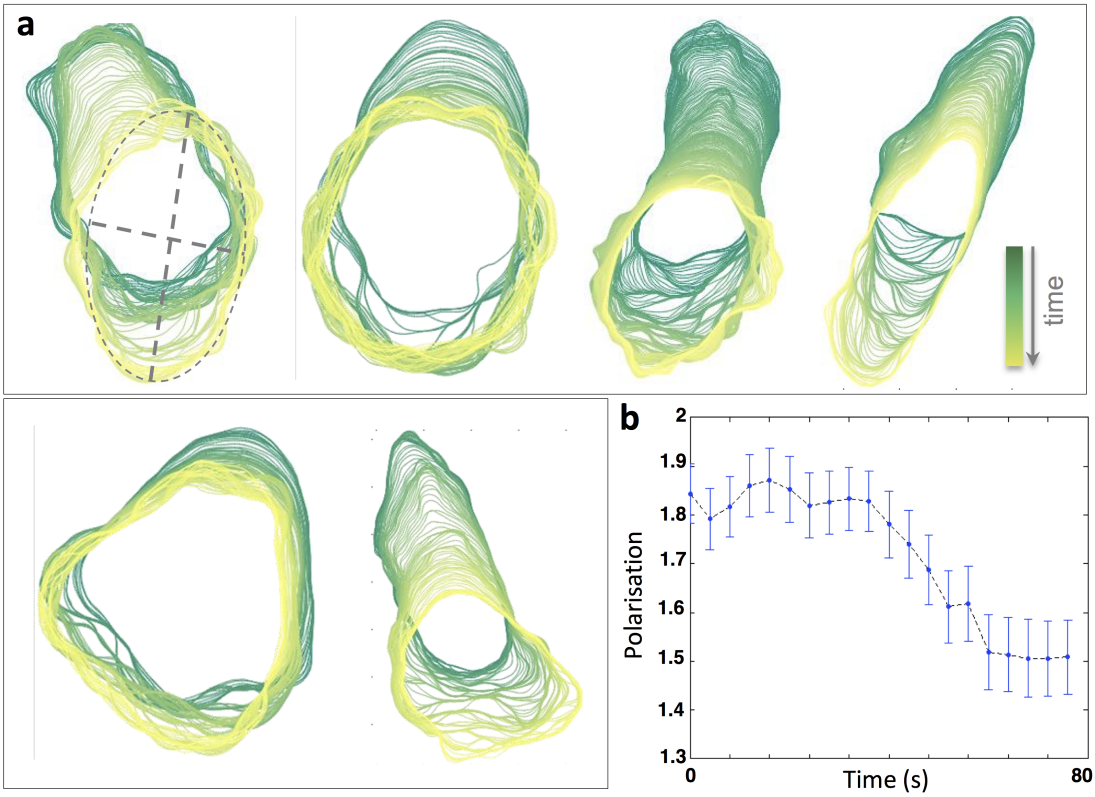

Figure 7.3: Migration over time using daughter blebbing results in curvature smoothing of the cell contour and a thus a decay in cellular polarisation. (a) Cell paths for 2% agarose cells (cells under 0.7% agarose do not migrate using many daughter blebs and so we do not include them here). Each individual contour is fitted to an ellipse, and the cellular polarisation defined to be the ratio of the major and minor axis. (b) Plot of the mean polarisation over time demonstrating the cell rounding due to repeated daughter blebbing.

7.1.4 Effect of repeated daughter blebbing on cell shape

The size of a daughter bleb is typically smaller than that of its parent bleb, the effect of this being that the daughter bleb size will decay over a number of blebbing events. We postulate that cell motility driven by repeated daughter blebbing will have a prominent effect on cell shape, smoothing the curvature profile of the cell over time, and thus reducing the number of likely sites of bleb nucleation. This is expected to cause a loss of geometric cell polarisation, thereby limiting migration ability. This phenomena is indeed observed experimentally, as demonstrated in figure 7.3, for *Dictyostelium* cells migrating in highly resistive environments.

To investigate whether this effect can be reproduced by the model, we evolve the model over time, based on the first contour of the image sequence only. On each iteration, the model nucleates a bleb in the most likely site. In order to compare experimental and model cell paths, we additionally include a rear retraction in the model, with the magnitude of the cortical contraction force based on maximum likelihood estimates. Figure 7.4 shows the the cell contour paths over time for the experimental data (a) compared to the cell paths obtained from evolving the model over 90 time frames. We see that daughter bleb size does decrease over time in the model, and with cell rounding occurring more rapidly in the model than is observed experimentally. We suggest that this is due to the model being purely deterministic, with the influence of stochastic linker kinetics becoming increasingly important with further cell rounding. Note that blebs are only observed to form in positively curved regions (unlikely according to the model) in 3% of cases, and thus implies that the contribution of stochastic effects is still small relative to the influence of geometry and linker gradients.

7.2 Towards a 3D visualisation of blebbing: diSPIM microscopy

7.2.1 Motivation

7.2.2 Is geometry driven bleb site selection a general mechanism?

Extension to other organisms: blebbing in Fundulus Deep fish cells

Here we ask the question of whether the bleb site selection mechanisms we see in *Dictyostelium* cells could be generalised across other organisms. We utilise *Dictyostelium* as a model organism to study blebbing motility since it is easily genetically manipulated, and cells are relatively easy to culture, in addition to growing rapidly. However, our end goal would be that our findings in *Dictyostelium* would be applicable in mammalian cells, with further advances in the field of cell migration aiding in development of therapeutic drugs for diseases associated with deficiencies in functionality of cell motility processes.

As an outlook to this question, we analysed blebbing data from a Fundulus deep cell (courtesy of Rachel Fink) using the quantitative method for predicting bleb site selection developed in this thesis. Figure 7.5 shows image data of a Fundulus

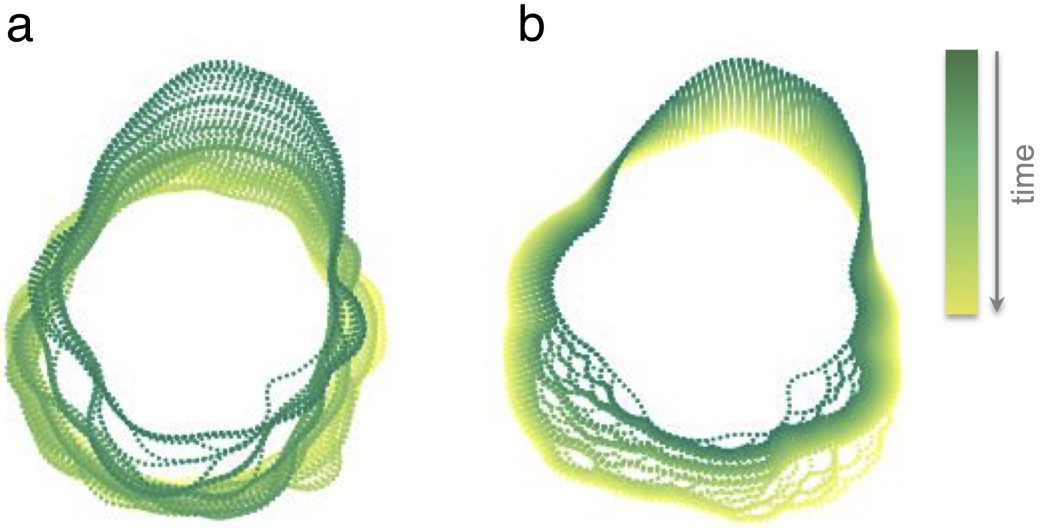

Figure 7.4: Cell contour paths over time, compared to those produced by evolution of the model by iterative blebbing in the most likely site. The model is initialised using the contour extracted from only the first image in the confocal time series. (a) Experimentally observed cell paths for a cell migrating under 2% agarose with repeated daughter blebbing. (b) Cell paths as predicted by the model, based on the first image contour only. Daughter bleb size is seen to decrease over time, and the same phenomena of cell rounding as in the experimental data is observed, although the rate at which this occurs is increased relative to the experimental data.

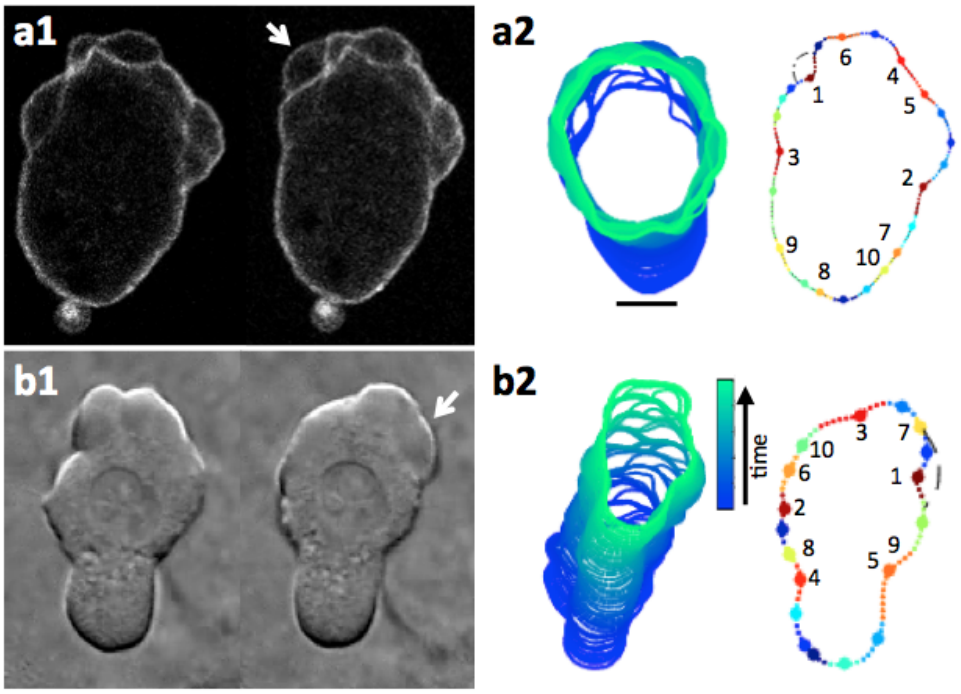

Figure 7.5: Bleb formation in *Dictyostelium* (a1, GFP-ABD, bar 5 m) and Fundulus deep cell (b1, DIC) (a2, b2) cell contour paths of sequences shown in a1) and b1), with example contour showing first 10 model bleb site rankings. Fundulus deep cell has a similar morphology to the *Dictyostelium* cells migrating in highly resistive environments, with a rounded cell rear that is geometrically distinct from the cell front, although the Fundulus deep cell has a pinched in waist region not present in *Dictyostelium* cells.

cell compared to a *Dictyostelium* cell under 2% agarose, demonstrating similar cell morphologies, with a geometrically distinct front and rear. This is also demonstrated in the box plot of cellular circularity for the Fundulus data, where we see that the fish cells have high circularities, comparable with the data from *Dictyostelium* cells migrating in highly resistive environment. The distribution of the ranked bleb sites and corresponding CDF also demonstrate the close resemblance to *Dictyostelium* 2% agarose data, as seen in figure 7.6. We see that for this example data from Fundulus deep cells, cell geometry is again a good predictor of bleb site selection. We would wish to increase the amount of data from Fundulus cells, and other organisms in the future to be able to address the question with increased statistical power.

In addition to applying our 2D methodology to other organisms to determine whether

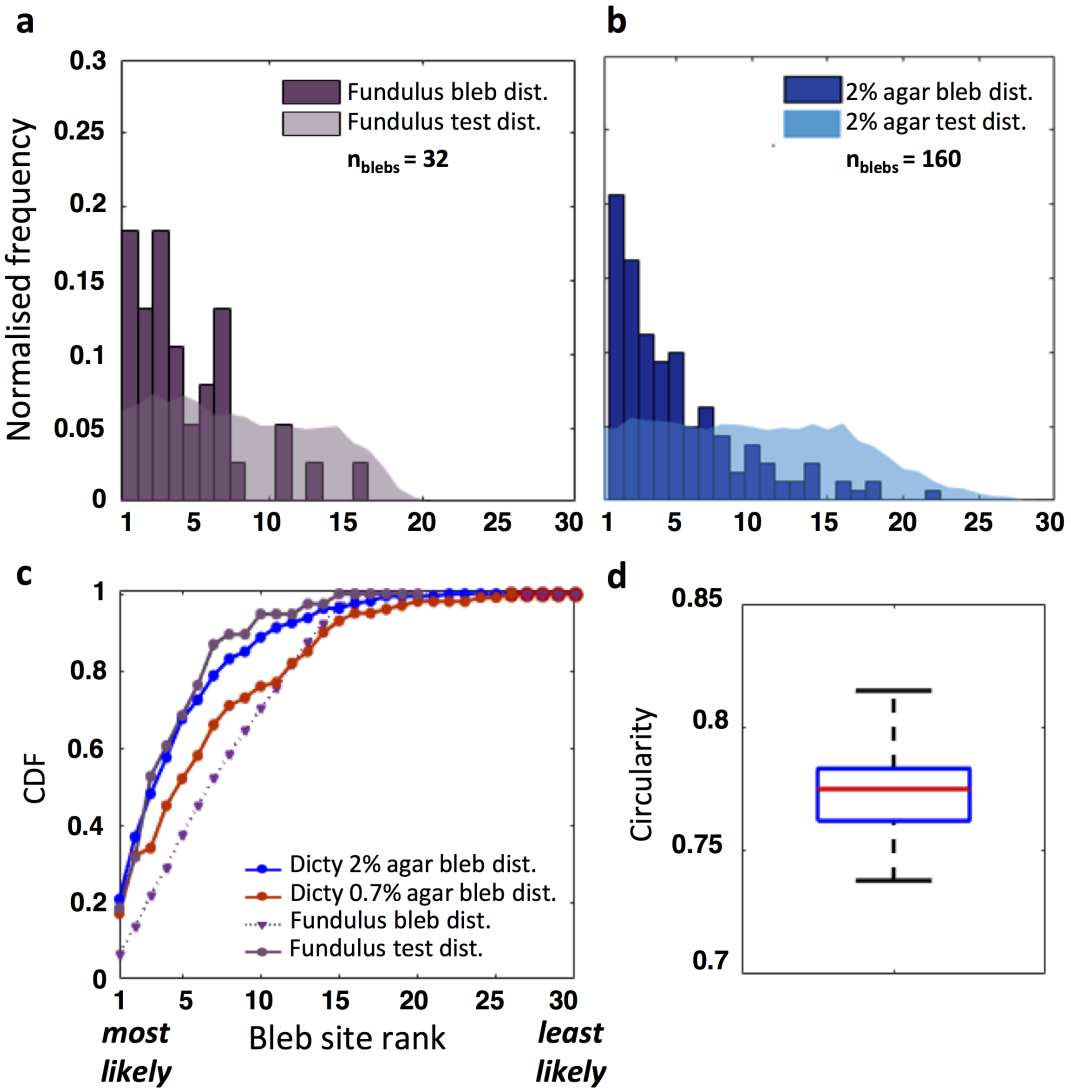

Figure 7.6: Modelling bleb site localisation in Fundulus deep cell (a) using cell geometry as input. Bleb sites scoring highest in the model prediction (low bleb site ranks) account for the largest fraction of experimentally observed blebs (in pale: test distributions for significance testing) (b) Bleb distribution for *Dictyostelium* cells under 2% agarose is shown for comparison. c) Cumulative density functions corresponding to a) and b) show that the Fundulus data matches more closely the case of *Dictyostelium* cells under 2% agar . Numbers give model bleb site ranks, showing that the bleb with the highest likelihood in the model is the one observed experimentally, indeed. d) Circularity boxplot for Fundulus deep cell image sequence again shows a resemblance to *Dictyostelium* 2% agarose data.

blebbing via physical mechanisms in combination with a graded membrane to cortex linker distribution is a general mechanism, we acknowledge the need to extend the analysis to 3D. As discussed previously, we encounter complications when mapping a 3D problem onto a 2D system, in terms of linkage at the bleb neck. Specifically with regards to the blebs maintaining a high neck curvature and preventing continued membrane unzipping. It would be useful therefore to extend the model to 3D, to see if this does indeed resolve the issue of bleb unzipping. In order to quantify the performance of a 3D version of our model against experimental data, we would first require the acquisition of high quality 3D images, with which to initialise the 3D model. (Actin, myosin and talin build up). Several interesting questions arise from a 3D analysis: (i) in terms of geometry driven bleb site selection, what is the topology of sites of bleb nucleation- do blebs arise form a local minimum in both principal curvatures, or do cases often exist where the site of nucleation is a saddle point (negative curvature in one direction, positive in the other)? (ii) what happens around a protrusion such as a pseudopod if the curvature around the flanks of the pseudopod is approximately uniform- our model in this case would predict a bleb ring (in the 2D system this simply appears to be 2 daughter blebs). Do we require a stochastic component in this case? (iii) What is the spatio-temporal localisation of proteins recruited to the bleb like? (Actin, myosin and talin build up).

To begin to address these points by proof of concept experiments we utilise a novel light sheet microscope, the dual-view inverted selective plane illumination microscope (diSPIM).

7.2.3 diSPIM imaging

Fluorescence imaging of membrane dynamics and the actin cortex demands high spatial resolution and good optical sectioning capabilities. For *Dictyostelium* cells which are particularly light sensitive, a further requirement is maintaining low phototoxicity. Due to this, obtaining high quality 3D image data with readily available laser scanning confocal microscopy (LSCM) is problematic, in terms of both acquisition speed and light exposure. This can be improved using spinning disc confocal microscopy (SDCM), which can reach 20 z-slices per second, and provides enhanced signal to noise ratio and sensitivity, enabling the amount of excitation light to be reduced. In practice however, even with the reduced exposure of SDCM, *Dictyostelium* cells round up after acquisition of only one cell volume.

The diSPIM developed by Wu et al. [Kumar et al., 2014] uses two perpendicular light sheets to provide the capability to reduce acquisition speed and photoxicity. Saturation of the fluorophores is minimised due to the sufficiently parallel excitation, and a high signal to noise ratio can be obtained at high frame rates, whilst the light sheet illumination is limited to the area of the focal plane, thus reducing photodamage to the cell.

7.2.4 Microscope configuration

The configuration of the diSPIM is demonstrated in figure 7.7. Two perpendicular water immersion objectives are used, each producing a light sheet that is imaged by the other, producing orthogonal sections through the specimen. Excitation is initiated by one objective, and the fluorescence emission collected by the other. For image acquisition, the light sheet is scanned across the surface of the sample, whilst the excitation objective is held stationary, and the emission collection objective scanning across the surface synchronously with the light sheet. The process is then repeated in the opposite direction, with the identity of the excitation and emission objectives now reversed. Thus for each full cell volume, two perpendicular image stacks are acquired, one from each objective. These two alternate views can be combined in a joint fusion-deconvolution algorithm, also developed by Wu et al, to recover the sample image with isotropic resolution. (With 3D acquisition from LSCM and SDCM, as well as other forms of light sheet microscopy, z-resolution is generally severely compromised relative to x-y resolution).

7.2.5 Deconvolution

As the DiSPIM acquires two images of the same object, perpendicular to each other, the direction in which the anisotropic point spread function (PSF) has the lowest resolution will be perpendicular to each other, and thus through fusing the two images and iteratively deconvolving them, we can remove the anisotropy. To achieve this we utilise the modified version of the Richardson- Lucy deconvolution algorithm presented by Wu et al.

Presently, there are some challenges to recovering fully deconvolved images of the cells, as diSPIM including software is still in the early development stage (with only 3 DiSPIM in the UK). Deconvolution of fluorescent beads is achievable, however deconvolution of cells requires first using fluorescent beads to 'register' the cell image, i.e to determine the misalignment in images recorded from each objective, such that

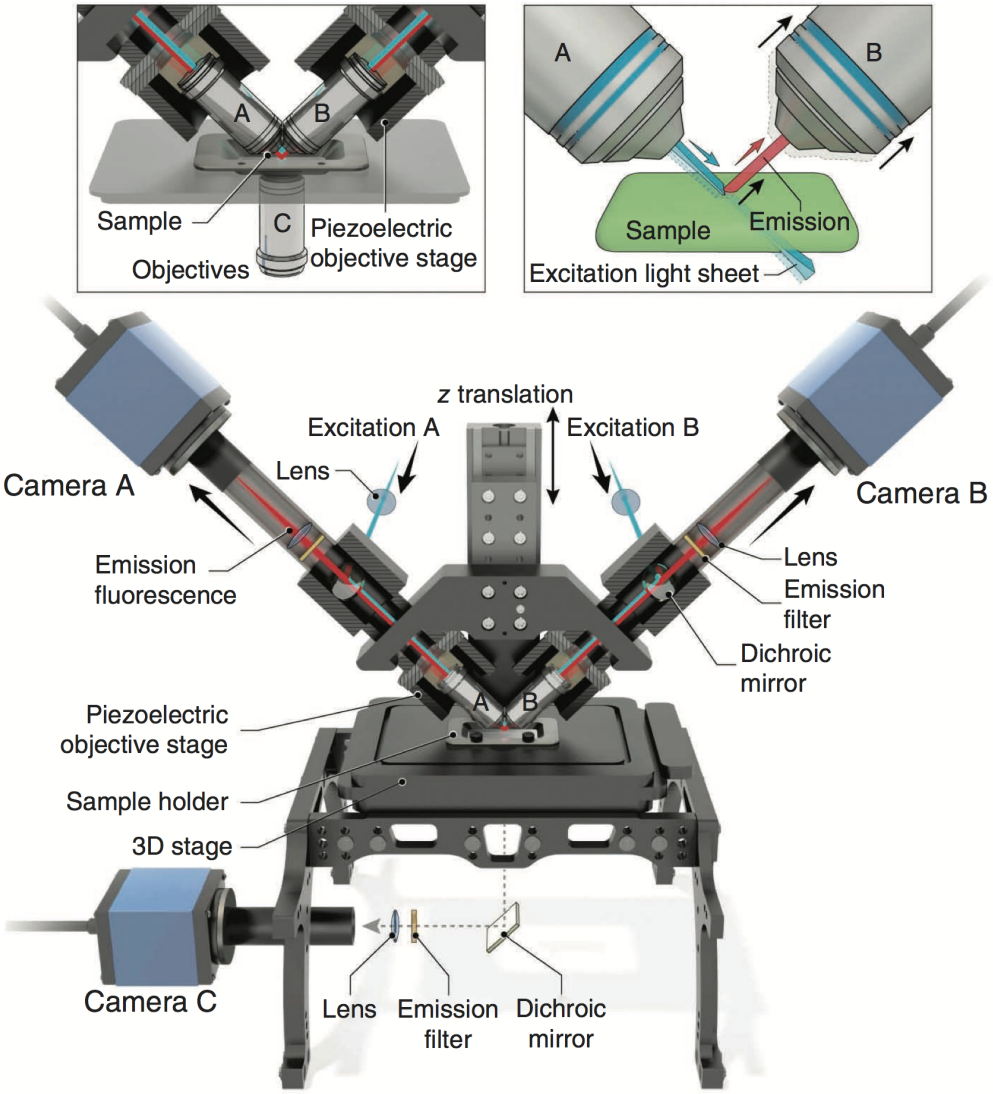

Figure 7.7: Configuration of diSPIM. Two perpendicular water immersion objectives are used, each producing a light sheet that is imaged by the other, producing orthogonal sections through the specimen. Image from [Kumar et al., 2014].

the two images can be properly overlayed. Fusion-deconvolution algorithms should now be applied on the overlayed perpendicular cell images, however, this software to achieve this has only very recently been implemented by microscope company 3i, and further development of the software is required. We therefore only present raw image data in this thesis, as a proof of concept that we can recover fast 3D images of dicty cells, capturing rapid, dynamic processes such as blebbing and macropinosomes, and can obtain multiple volumes before cells round up.

7.2.6 Preliminary results

7.2.7 Capturing blebbing in 3D

Capturing blebbing through the under agarose assay introduces several complications due to the configuration of the microscope- all 2D analysis has been performed with an inverted oil immersion microscope. This microscope setup can only image cells through a 0.2mm thick layer of agarose with the high working distance water immersion objectives. Therefore we instead choose to use cAMP shock assays. Figure 7.8 shows maximum z-projections of the 3D image data recorded on the diSPIM for a blebbing *Dictyostelium* cell. We show that after 25 volumes the cell has still not rounded up due to high levels of phototoxicity.

7.2.8 Macropinosomes

We also show here that the diSPIM is capable of capturing other rapid cellular processes, such as the opening and closing of macropinocytic cups used by the cell to take in nutrients from liquid media, figure 7.9. Again, cell rounding is not observed after successive volume acquisitions.

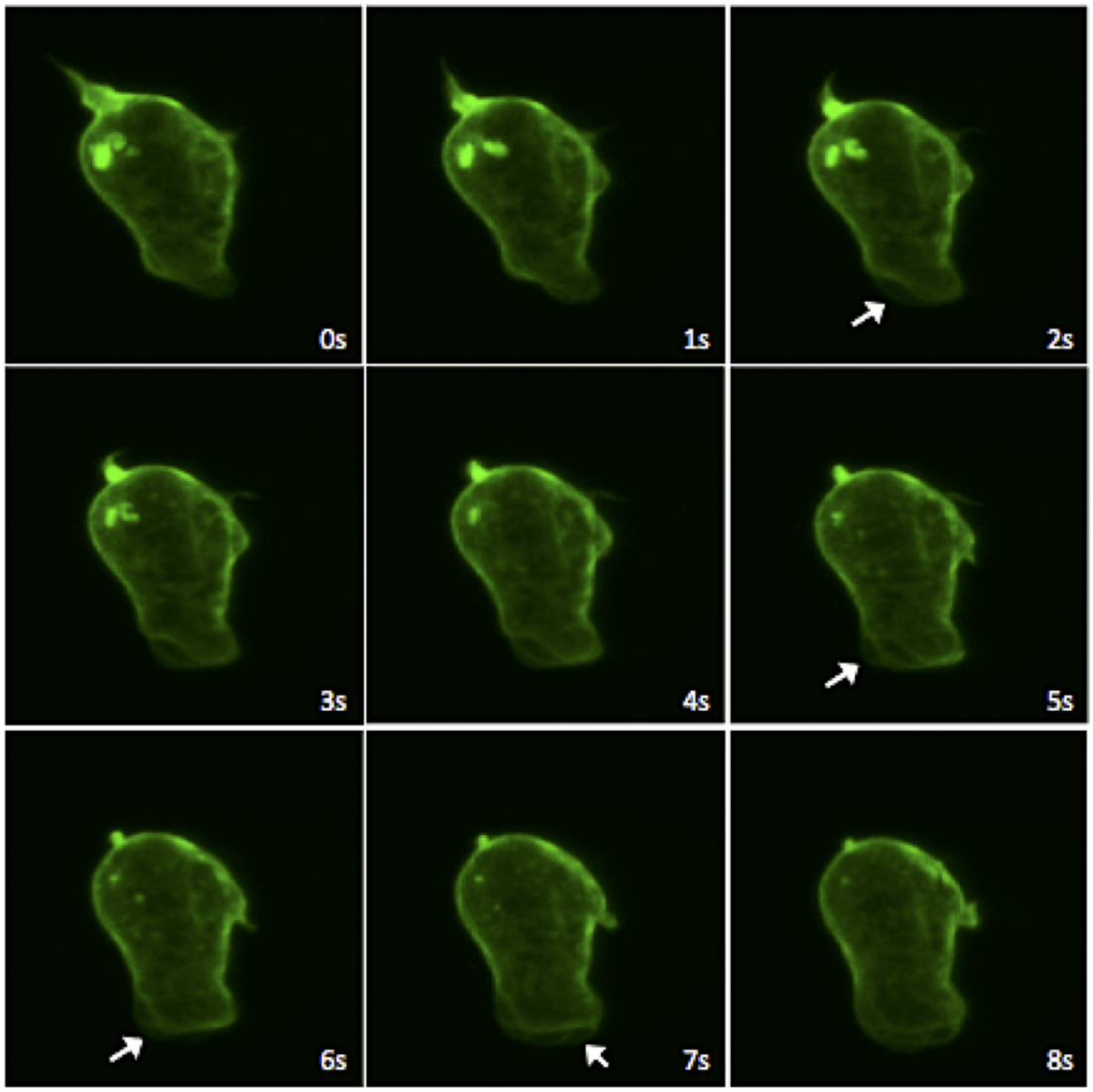

Figure 7.8: Preliminary results (maximum z-projections) of *Dictyostelium* cells blebbing, as induced by cAMP shock, captured using diSPIM. Cells express ABD-GFP, an F-actin marker. Cells do not round up after imaging of successive volumes, unlike in SDCM, where only one complete volume acquisition is possible.

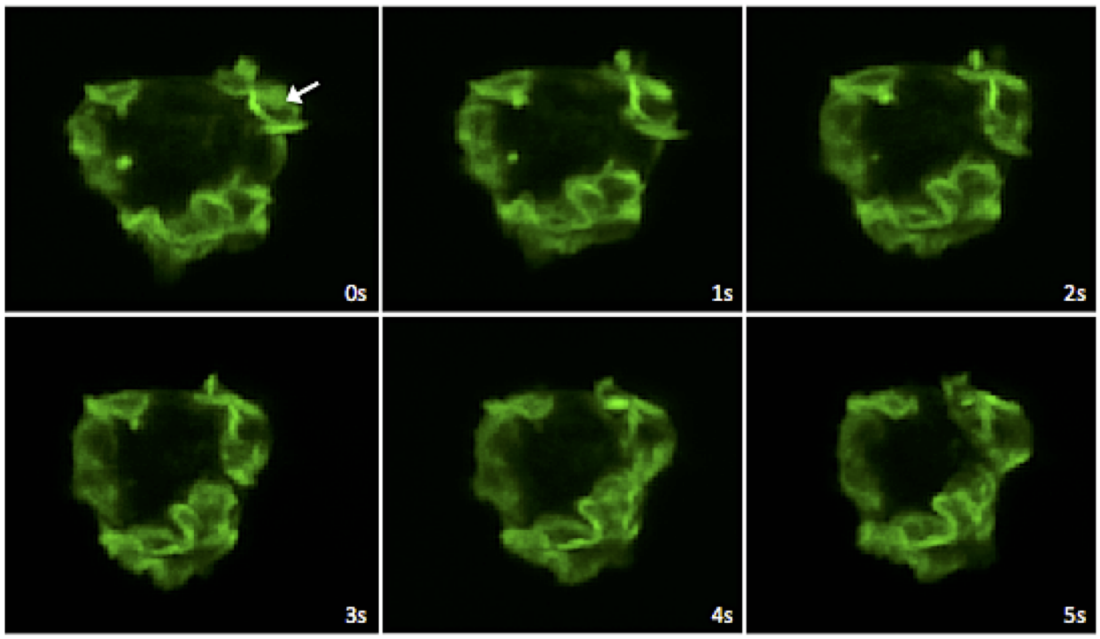

Figure 7.9: Preliminary results (maximum z-projections) of *Dictyostelium* cells opening and closing macropinocytic cups to take in surrounding media. Macropinocytosis is a very rapid dynamic process, and thus demonstrates the fast imaging capabilities of the diSPIM

Chapter 8

Discussion and conclusions

8.1 Discussion

8.1.1 Disentangling physical and biological mechanisms for bleb site selection

Migration driven by bleb expansion is characteristic of cell motility in a mechanically resistive or confined environment, where either the small pores or channels through which a cell has to navigate, or high rigidity of the surrounding material, make slow actin-driven protrusions less feasible [Charras and Sahai, 2014] [Laevsky and Knecht, 2001]. The question of how bleb sites are selected, and also restricted around the cell posterior, to aid efficient chemotactic movement in real 3D environments, as opposed to movement on a 2D surface in standard cell cultures, is therefore of great relevance.

In our model, the strain on cortex-membrane linkers is highly dependent on geometry. Whilst other models have also taken into account the influence this strain has on linker dynamics, this has only been considered across small scale local fluctuations of the membrane [Alert et al., 2015] [Alert and Casademunt, 2016], whereas our coarse grained approach allows us to study bleb site selection globally, including its dependence on active shape deformations as a result of pseudopod formation.

Previously, work by Tyson et al. suggested that bleb site selection could be driven entirely by physical mechanisms, namely cellular geometry [Tyson et al., 2014]. The direction of the resultant force of the membrane tension, which differs based on local curvature, was proposed to be the mechanism driving such geometry dependent bleb site selection, and was assumed to account for the experimental observation that

blebs preferentially nucleate from areas of negative curvature. Tyson et al. presented a biophysical model to demonstrate this, using an idealised cell contour to initialise the model, and showing the nucleation of two blebs on the concave flanks of the pseudopod. However, by utilising a simplified artificial geometry to represent a cell, they were only able to investigate a single case.

Here we develop a quantitative method to assess the predictive power of the model, initialised using real cell contour data, in which we rank bleb sites in order of nucleation likelihood. Cell contour analysis is well established in investigations of cell membrane mechanics, for example in micropipette aspiration [Merkel et al., 2000] or analysis of cell shape flickering [Park et al., 2010]. Our modelling framework is fundamentally different however, in such that we are able to predict actual cell shape changes, even in migrating cells with highly complex geometries. Additionally, our method of ranking sites according to model likelihood, and comparing to experimentally found distributions for different models proved to be useful for stochastic biological processes, and is likely to to be a useful tool in other applications. We already demonstrate that our approach is applicable to other cell types, by computing how the model fits to data from a Fundulus deep cell, and show that the same geometry dependent principles apply, figure 7.5.

Applying our method linking experimental data to predictive modelling, on images of chemotaxing *Dictyostelium* cells, we show that cell geometry is only a good predictor of bleb site selection in cells migrating in highly resistive environments. In this case, the positively curved, highly rounded cell rear disfavours blebbing, and thereby acts to polarise blebbing activity, with more blebs nucleating at the cell front. The idealised cell contour used in the Tyson paper, has a similarly distinct front and rear in terms of cellular geometry, thus explaining their conclusion that geometry alone is sufficient to orient blebs to the cell front in chemotaxing *Dictyostelium* cells.

We show however, that for cells in low resistive environments, where the front and rear of the cell are not geometrically distinct, an additional mechanism is required to polarise the spatial distribution of bleb nucleation likelihood, to reduce or inhibit blebbing at geometrically likely sites at the cell rear. We proposed that a likely candidate for preventing blebbing at the cell rear, and thus maintaining cellular polarity is a gradient in cortex-membrane linkage strength, in particular for the linker protein Talin. We have shown through the creation of a TalinA-mNeon construct, that Talin is indeed asymmetrically distributed in chemotaxing *Dictyostelium* cells, exhibiting an

exponentially graded localisation profile, increasing from front to rear. In addition to this, we have found blebbing activity to be inversely related to Talin enrichment, with no blebs nucleating in regions of maximal Talin fluorescence. Incorporating these findings into an updated version of the model greatly increases the predictive power with regards to the spatial distribution of bleb sites, for cells moving in low resistive environments. Our work therefore provides strong evidence that a graded linker distribution acts in tandem with physical geometry dependent mechanisms to influence bleb site selection.

Although molecular mechanisms responsible for generating graded linker distributions are still unknown, regulation through PIP2, the membrane lipid that binds linkers, has been a recurring theme in current literature [Yamazaki et al., 2014] [Raucher et al., 2000] [Fets et al., 2014]. Zatulovskiy et al. found clear evidence that PI3-kinase signalling plays a crucial role in *Dictyostelium* blebbing. Mutants with all five PI3Ks knocked out had previously been shown to have only minimal chemotactic defects in buffer, however, these have now been shown to be severely impaired in blebbing. The PI3Ks reduce the amount of PIP2, by phosphorylating it to PIP3, with cells deficient in PI3Ks therefore generating higher level of PIP2. Such increased levels of PIP2 (a known binding partner of Talin) are very likely to result in stronger membrane to cortex adhesion, explaining the reduced blebbing phenotype. Consistent with this, Zatulovskiy et al. additionally showed that loss of the predominate PI4P5-kinase, PikI, which results in cells with only 10% of wild-type PIP2 levels, produce a strongly blebby phenotype in buffer. However these cells can only rarely penetrate under agarose, similarly to Talin null cells.

When cells use blebs for chemotactic movement, the guiding chemotactic gradient must be able to influence where blebs form, directing them preferentially up-gradient. Our results show that this guidance could be exerted quite indirectly through cell geometry. Geometry itself is the product of previous shape changes caused by earlier cellular extensions and retractions, including blebs, F-actin driven pseudopods and spikes, and myosin-II driven retractions. Any or all of these processes could help determine where blebs form, in addition to any direct effect that chemotactic signalling may have on blebbing, such as by locally affecting the membrane-cortex linkers.

8.1.2 Extension to a stochastic model and time dependence of bleb nucleation

Many models in the literature assume bleb nucleation to be either entirely stochastic or utilise cortex ablation to artificially initiate bleb nucleation [Alert and Casademunt, 2016] [Woolley et al., 2015] [Strychalski and Guy, 2011] [Young and Mitran, 2010]. Our model differs however, with spontaneous bleb nucleation arising at geometrically likely sites, above a critical pressure. Although laser ablation is a commonly used experimental technique to induce blebbing in a controlled manner, bleb nucleation via cortical rupture is rarely observed in wild type cells. Additionally, although stochastic linker kinetics will certainly play a role in bleb site selection, we show that a deterministic model can explain a large proportion of the data. We postulate however, that stochastic effects become increasingly important when considering migration over time using only blebbing motility. In this instance, daughter blebbing (blebbing in the negatively curved regions either side of the parent bleb) is frequently observed. Migration using repeated daughter blebbing however will smooth the cell contour over time, we have observed this experimentally with a decay of cellular polarisation in cells migrating under 2% agarose. We suggest that the rate of decay of cellular polarisation would decline more rapidly in a deterministic system, as stochastic events may permit blebbing in regions of positive curvature, and could therefore act to reintroduce a curvature feature into the geometric landscape.

Interestingly, investigation of regions where the model would predict daughter blebs to form revealed a time delay before their nucleation, which we suggest is linked to the timescale of formation of a new cortex and recruitment of linkers. An alternative possibility for the time delay is to allow for sufficient repressurisation of the cell, however cells often nucleate multiple blebs in a single time frame, or nucleate a bleb in a different location before nucleation of a daughter bleb, indicating that the pressure is not the determining factor here.

8.1.3 Extension of the model to 3D surfaces: using diSPIM data to initialize the model

New 3D experimental data is required to recover the full spatio-temporal dynamics of cortical proteins and linker recruitment to the bleb. This would allow us to probe factors which rely on cortical dynamics, such as multi-blebbing and bleb retraction.

Extension of our image based modelling analysis to 3D requires high quality 3D cell data and methods for segmenting and tracking cell shapes accurately in 3D. Recent advances in lightsheet microscopy techniques, such as the development of DiSPIM, allow for the fast acquisition speeds and low phototoxicity essential for imaging rapid cellular processes in *Dictyostelium*. Here we have collected some preliminary results demonstrating that the DiSPIM has a sufficiently high frame rate to capture the rapid dynamics of blebbing in *Dictyostelium*.

8.2 Conclusions

We have introduced a novel image based modelling approach to predict bleb site selection in chemotaxing *Dictyostelium* cells. In addition to this, to aid in efficient high throughput analysis, we have developed algorithms to automatically identify experimental blebs from confocal image sequences, and to automatically determine the cell front and polarisation axis. Our results have shown that cell geometry alone is a good predictor of bleb site selection in cells in highly resistive environments, but highlighted the need for an additional mechanism to restrict blebbing activity to the cell front for cells in low resistive environments.

A likely contender for such a mechanism was an inhomogeneous distribution of the membrane to cortex linker protein, TalinA. We created a TalinA-mNeon reporter to visualise TalinA localisation in *Dictyostelium* cells, which demonstrated an exponentially graded distribution in fluorescence intensity. Inclusion of a graded linker strength in the model, in accordance with experimental observation, yielded a greatly improved fit for cells in low resistive environments.

We investigated multi-blebbing, suggesting that the low adhesion in talin knock-out cells could be responsible for the frequently observed lobopodia. We also postulated that migration using daughter blebbing will result in smoothing the cell contour over time, resulting in a decay of cellular polarisation, as was indeed observed for cells migrating under 2% agarose, where blebbing is the only mode of migration.

We outline further work using light sheet microscopy to extend our work to 3D, we have shown with preliminary results that capturing the rapid dynamics of cellular blebbing, with high acquisition speeds and low phototoxicity is possible. We intend to continue this work, with full deconvolution of the images, and extension of the model

to 3D, where high quality 3D reconstruction and segmentation would allow us to use diSPIM data to initialise the model.

We also aim to investigate how general the mechanism of geometry driven bleb site selection is in combination with a graded linker distribution, by extending the work to other organisms. We have made the first steps here, with our analysis of a Fundulus deep fish cell providing supporting evidence for this generalisation.

The quantitative method which we have developed for predicting bleb site selection allows us to probe the relative contributions of biological and physical mechanisms for cells migrating in mechanically resistive environments.

Appendix

.1 Code

```
function [linkerlength]=ThesisBlebNucleationModel(HP,G,X)

%                                                                       %
%This function reads in membrane and cortex node positions extracted from
%QuimP segmentation of cell contours obtained using confocal microscopy.
%Parameter values are initialised, some of which (such as tension stiffness
%coefficients, linker resting lengths and stiffnesses) are fixed, whilst
%other parameters such as hydrostatic pressure and number of nodes are
%updated for each cell contour. (See methods section for further info)

%We aim to numerically solve the following pde for the membrane position
%vector x:
%   > n.dx/dt=dE(x)
%where dE(x) is the variation of the total membrane energy functional (i.e.
%the force). n is the drag coefficient of the surrounding environment.
%We do this by expressing dE(x) as a finite difference approximation, and
%passing  dE(x)/n to MATLAB ode solver 23 to compute the solution at each
%timestep

%Linkers acting as linear springs in parallel connect corresponding membrane
    and
%cortex nodes. The final linkerlength at each node after force equilibrium
%has been reached is output by this function. We later use this as a
%measure of local blebbing propensity.
%                                                                       %

    %FUNCTION INPUT ARGUMENTS (HP,G,X):
    %HP = initial hydrostatic pressure parameter (varies for each cell
    %contour)
    %G = integer on the interval (1,N) where N is the number of contours
    %investigated. This simply allows us to access the input file of
    %interest
    %X = number of nodes. We hold node density constant from cell to cell,
    %thus X is computed from the perimeter/node density

%                       model parameters                                %
%                 all measures are in uN and um                         %
    avBlebR = 1.15;         %average bleb radius used to estimate a drag
       constant 1.26
    ds= 1/X;                % ds   fractional contour length
    ds2=ds*ds;              % squared ds (used in second order finite
       difference eqns)
```

```
40
41      m_ka= (17e 6)*ds^2;     % membrane stiffness coeff (Strychalski 2 10 pN/um
            )
42      m_kb= (0.14e 6)*ds^4;  % membrane bending rigidity
43      m_maxPerChange = 0.95; % percentage change in membrane length to
            determine resting length
44
45      c_ka = 0.4e 6;          % cortex tension coeff
46      c_kb = 0.4e 6;          % cortex bending coeff
47
48      L_k = 10e 6;            % linker stiffness coeff
49      L_rest=0.04;            % default linker length
50      L_break=0.056;          % maximum extension of linker before it breaks
51      L_min = 0.01;           % minimum linker length
52      L_scale = 0.5;          % scale up linkers for plotting (shrinks cortex)
            1=off
53
54      %initialise global variables that will later be updated
55      breakAtT = inf;         % time after which linkers are allowed to break
56      L_letBreak=0;           % true or false event: ==1 if t>breakAtT, ==0
            otherwise
57      HP_F = 0;               % hydrostatic pressure force
58      A = 0;                  % area inside membrane
59      A_static = 0;           % starting area inside membrane for computing
            pressure changes
60      P_static=0;             % starting perimeter of membrane
61      Perimeter = 0;          % perimeter of membrane
62      node_dens = 0;          % node density for determining force per node from
             pressure
63      avSpacing_c = 0;        % spacing between nodes of cortex
64      avSpacing_m = 0;        % spacing between nodes of membrane
65      m_restL = 0;            % resting length of membrane segment (
            m_maxPerChange*staring segment length)
66      L_intact=zeros(1,X);    % vector containing which linkers are intact (1=
            intact, 0=broken)
67      blebR = 0;              % bleb radius (last bleb only)
68
69      % position vector indices
70      l=[X,1:X-1]; r=[2:X,1];                 % left and right indexing vectors
71      px=[1:X]; py=[X+1:2*X];                  % Indicies of x then y coordinates
            of membrane
72      pxc=[2*X+1:3*X]; pyc=[3*X+1:4*X];        % Indicies of x then y coordinates
            of cortex
73      plinks =[4*X+1:5*X];                     % Indicies of linker data
```

```
74      L_k_o=ones(X,1).*(L_k);                    % Stiffness vector for linkers
75      dragConst = 6*pi*1e 3*1e-6*avBlebR;   % water 20degC 1e 3, + units of
            Radius to meters with 1e 6
76
77      % ode options
78      ops = odeset('OutputFcn', @blebOdePlot,'Events',@letBreakEvent, 'RelTol',
            1e 6, 'AbsTol', 1e 6);
79
80      %create output figure
81      hFig =figure(1);
82      cla(hFig);
83      axis equal
84      axis off
85      set(gca,'YDir','reverse');
86      hold on;
87      plotCounter = 0;
88
89          %input cell contour extracted from microscopy image
90          inputData=load(['BlebContour_' num2str(G) '.mat']);
91
92          if( size(inputData.last,2)/5~=X),
93              % 5 sets of data in matrix (membrane x, membrane y, cortex x,
94              % cortex y, linkers)
95              fprintf('X does not match node number in loaded data !\n');
96              return;
97          end
98
99          %Extract coordinate data from inputData matrix and save as vectors
100         x = inputData.last(px); y = inputData.last(py);
101         xc = inputData.last(pxc); yc = inputData.last(pyc);
102         inputData.last(plinks) = 1; % linkers intact
103
104         paramEstimation(); % set free parameters
105
106         %equilibrate system then allow breaking
107         times=[0 :0.002: 0.85]; %evenly spaced time points
108
109         breakAtT = 0.05; % time after which linkers can break, iff they have
                exceeded the critical length
110
111         [t,positions]=ode23(@vel_mem,times,inputData.last,ops);
112
113     function paramEstimation
114         per_c = sqrt( (xc(r) - xc).^2 + (yc(r) - yc).^2 );
```

```
115         avSpacing_c = mean(per_c);
116         per_m = sqrt( (x-x(r)).^2 + (y-y(r)).^2 );
117         avSpacing_m = mean(per_m);
118         A_static = 0.5*sum(x.*y(r)-x(r).*y);
119         P_static = sum(sqrt( (x-x(r)).^2 + (y-y(r)).^2 ));
120         m_restL = avSpacing_m*m_maxPerChange;
121         node_dens = 1/avSpacing_m;
122     end
123
124
125     function movement=vel_mem(t,positions)
126
127         %extract coordinates for membrane and cortex
128         x = positions(px); y = positions(py);
129         xc = positions(pxc); yc = positions(pyc);
130         L_intact = positions(plinks);
131         L_intact = L_intact==1; % 1 if intact, 0 otherwise
132
133         % set linker stiffness
134         L_k_o(:)= L_k;
135         L_k_o(~L_intact) = 0; %i.e. linker broken is same as saying it has a
              spring constant of zero
136
137         %compute normal to membrane
138         tanx = x(r) - x(l); tany = y(r) - y(l); % compute tangent vector, x
              and y components
139         n=sqrt(tanx.^2+tany.^2);                % compute magnitude of normal
               vector to contour
140         nx = -tany./n; ny = tanx./n;            % compute x and y components
              of normal vector
141
142         %compute area and Perimeter
143         A = 0.5*sum(x.*y(r)-x(r).*y);
144         Perimeter = sum(sqrt( (x-x(r)).^2 + (y-y(r)).^2 ));
145         dz = 0.01;
146         Ai=avSpacing_m*dz;
147
148         % update pressure from initial input parameter dependent on change in
               cell area
149         HP_F = (HP * (A_static/A));
150
151         % extend short linkers
152         lx=x-xc; ly=y-yc;                       % linker position vector is the
               difference between membrane and cortex positions
```

```
153         linkerlength=sqrt(lx.^2+ly.^2);          %magnitude of linker position
                vector
154         lx_u=lx./linkerlength; ly_u=ly./linkerlength; % unit lengths
155         tooshort=(linkerlength<L_min);
156         x(tooshort)=xc(tooshort)+L_min*lx_u(tooshort);
157         y(tooshort)=yc(tooshort)+L_min*ly_u(tooshort);
158
159         %compute linker direction,(point inwards) extension/compression
160         lx=x-xc; ly=y-yc;
161         linkerlength=sqrt(lx.^2+ly.^2);
162         lx_u=lx./linkerlength; ly_u=ly./linkerlength; % unit lengths
163         llx=(linkerlength-L_rest).*lx_u; lly=(linkerlength-L_rest).*ly_u; %
              compares linker length to default linker length to compute
              extension or compression
164
165
166         if(~L_intact),
167             % if all linkers are broken...
168         elseif(any(~L_intact)), %else if any linkers are broken...
169             basalLinkers = L_intact(:) - L_intact([2:end,1]); %find the two
                  linkers either side of blebbing region (we refer to these as '
                  neck linkers')
170             ref = 1:X;
171             startb = ref(basalLinkers==1);
172             endb = ref(basalLinkers==1)+1;
173             if(startb(1)>=endb(1))
174               % redefine end index of bleb if that bleb crosses both the
                     first
175               % and last nodes of the contour (closed curve constraint)
176               endb(:) = endb([2:end,1]);
177             end
178
179             for i=1:length(startb)
180                 % ensure end index of bleb cannot exceed number of nodes
181                 if endb(i)>X
182                     endb(i)=X;
183                 else endb(i)=endb(i);
184                 end
185             end
186
187             % we increase the stiffness of the neck linkers as the bleb
                  expands, in proportion to its radius, to account for the 3d
                  effect of an increased number of linkers around the bleb
                  circumference as it expands, acting to slow its growth
```

```
            outwards.
188         basalL = sqrt((xc(startb)-xc(endb)).^2 + (yc(startb)-yc(endb))
                .^2);
189         basalStrength = (basalL./avSpacing_c)*(L_k)*pi*0.5;
190         L_k_o(startb) = basalStrength;
191         L_k_o(endb) = basalStrength;
192
193        % find membrane length of blebs
194         nbBlebs = length(startb); % number of blebs
195         for i = 1:nbBlebs,
196            if( startb(i) > endb(i) ), % satisfy closed curve constraints
197                ref = [startb(i):X, 1:(endb(i)-1)];
198            else
199                ref = startb(i):(endb(i)-1); % right neighbour is always
                       under X
200            end
201            blebR = basalL(i)/2 ;
202        end
203    end
204
205    % compute membrane resting length components
206    m_xDiff = x(r) - x;  m_yDiff = y(r) - y;
207    l_seg = sqrt( m_xDiff.^2 +  m_yDiff.^2 );
208    m_xRest = (m_xDiff./l_seg).*m_restL;        % these are directional
209    m_yRest = (m_yDiff./l_seg).*m_restL;        % resting length clockwise
           (to the right of x)
210
211    %compute finite difference approximations for variation of total
           membrane energy functional
212
213    % second order derivative
214    Second_x = (x(l) - 2*x + x(r))/ds2;
215    Second_y = (y(l) - 2*y + y(r))/ds2;
216    % fourth order derivative (defined recursively in terms of second
217    % order term
218    Fourth_x = (Second_x(l) - 2*Second_x + Second_x(r))/ds2;
219    Fourth_y = (Second_y(l) - 2*Second_y + Second_y(r))/ds2;
220    % second order derivative including derivative of resting length
221    Second_x_R = (( x(l) - 2*x + x(r))  - m_xRest + m_xRest(l) )/ ds2;
222    Second_y_R = (( y(l) - 2*y + y(r))  - m_yRest + m_yRest(l) )/ds2;
223    %compute membrane movement
224    dxdt = m_ka*Second_x_R - m_kb*Fourth_x - HP_F*nx*Ai - L_k_o.*llx;
225    dydt = m_ka*Second_y_R - m_kb*Fourth_y - HP_F*ny*Ai - L_k_o.*lly;
226    %m_ka*Second_x_R:   tension
```

```
227         %m_kb*Fourth_x:      bending
228         %HP_F*nx*A_i:              pressure
229         %L_k_o.*llx:             coupling
230
231         % include drag
232         dxdt = dxdt/dragConst;
233         dydt = dydt/dragConst;
234
235         %Assume cortex is stationary on timescale of bleb nucleation
236         dxcdt = dxdt*0;
237         dycdt = dydt*0;
238
239         % break linkers by shifting dldt from 0, if applied (cannot reform)
240         dldt = zeros(X,1);
241         if L_letBreak ==1,
242             dldt(linkerlength>L_break)= 1; %doesn't matter what this value is
                , so long as it is not 0
243         end
244
245         % final output which is passed to odesolver
246         movement=[dxdt;dydt;dxcdt;dycdt;dldt];
247
248     end
249
250
251
252     function [value,isterminal,direction] = letBreakEvent(t,y,i,p)
253
254        % This event allows linkers to break after some time point
255        % (although after this time, wether a linker breaks or not is still
256        % dependent upon if its length is greater than the critical length,
257        % L_break
258
259        if(t > breakAtT),
260             L_letBreak=1;
261        end
262
263        value = t;
264        isterminal=0;
265        direction=0;
266     end
267
268
269
```

```
270     function stop = blebOdePlot(t,positions,inti,P)
271
272         %output function to odesolver  plots cell contour including membrane,
273         %cortex and linkers, and updates their positions with each timestep
274
275         if(isempty( t)),
276             stop = 1;
277             return
278         end
279
280         plotCounter = plotCounter+1;
281
282         hFig = gcf;
283         cla(hFig);
284
285         if( size(positions,2) > 1 )
286              positions = positions(:,2);
287         end
288
289         % retrieve membrane and cortex coordinates for plotting
290         xP = positions(px); yP = positions(py);
291         xcP = positions(pxc); ycP = positions(pyc);
292         % retrieve list of intact linkers
293         lOK = positions(plinks);
294         lOK = lOK==1;
295
296         if(L_scale ~=1), % scale cortex to make linkers viewable
297              % (this will shrink the cortex)
298              tanx = xcP(r)-  xcP(l); tany = ycP(r) - ycP(l);   % compute
                     tangent vectors
299              n=sqrt(tanx.^2+tany.^2);                          % compute
                     magnitude of normal vector
300              nx = (-tany./n)*L_scale; ny = (tanx./n)*L_scale;   % compute x
                     and y components of normal vector
301              xcP = xcP+nx;  ycP = ycP+ny;                      % update
                     cortex positions
302         end
303
304         lineWidth = 1.5;
305         %plot linkers in black (intact only)
306         plot([xP(lOK),xcP(lOK)]',[yP(lOK),ycP(lOK)]','k','LineWidth',
                lineWidth);
307         hold on
308         %plot membrane in red
```

```
309         plot([xP;xP(1)],[yP;yP(1)],' b', 'LineWidth', lineWidth);
310         hold on;
311         %plot cortex in green
312         plot([xcP;xcP(1)],[ycP;ycP(1)], 'Color',[0.17 0.51 0.34],'LineWidth',
                lineWidth);
313
314         drawnow
315
316         %allow user to end ode solver at any time, by entering 'e' on the
                keyboard
317         keyIn = get(hFig,'CurrentCharacter');
318         fprintf('Type e to exit: %s  \n', keyIn);
319         if(keyIn == 'e'),
320             stop = 1;
321         else
322             stop = 0;
323         end
324
325
326     end
327
328
329
330 end
```

.2 Optimisation of hydrostatic pressure: results tables

Table 1: 2% agarose data results

2 % agar:										
Parameters					FALSE	TRUE	FALSE	TRUE		
A_static	Optimum HP	Circularity	Contour Length	Mean bleb diameter	Positives	Positives	Negatives	Negatives	Sensitivity	Specificity
179.5877	8.85E-05	0.851	53.840	3.105	4	1	0	12	1.00	0.75
178.2797	8.79E-05	0.902	51.524	2.763	3	2	0	14	1.00	0.82
178.5975	8.81E-05	0.854	53.920	2.796	5	2	0	12	1.00	0.71
178.9532	8.82E-05	0.886	52.863	2.597	4	3	2	11	0.60	0.73
178.5492	8.80E-05	0.921	50.550	3.423	3	0	1	11	0.00	0.79
180.2094	8.89E-05	0.906	52.702	2.743	4	4	0	11	1.00	0.73
179.2248	8.84E-05	0.896	52.479	2.733	5	3	0	11	1.00	0.69
179.7705	8.86E-05	0.913	52.134	2.833	2	6	0	10	1.00	0.83
179.7228	8.86E-05	0.881	52.735	3.892	4	1	0	9	1.00	0.69
181.609	8.95E-05	0.859	54.362	3.061	4	2	0	12	1.00	0.75
175.3369	8.65E-05	0.900	50.536	3.041	3	0	1	13	0.00	0.81
174.9045	8.62E-05	0.812	55.177	2.652	4	3	0	14	1.00	0.78
173.3369	8.55E-05	0.866	52.263	2.935	3	3	0	12	1.00	0.80
174.6405	8.61E-05	0.885	51.433	2.755	3	1	1	14	0.50	0.82
175.7192	8.66E-05	0.888	51.328	3.114	3	1	1	11	0.50	0.79
177.0852	8.73E-05	0.920	49.319	0.000	3	0	0	0	0.00	0.00
175.7455	8.67E-05	0.863	51.678	2.690	4	1	2	12	0.33	0.75
174.322	8.60E-05	0.869	52.716	2.691	5	4	0	11	1.00	0.69
176.2372	8.69E-05	0.879	52.733	2.643	6	1	0	13	1.00	0.68
174.3307	8.60E-05	0.872	51.710	3.270	4	1	1	10	0.50	0.71
128.0232	6.31E-05	0.701	48.819	2.757	1	1	1	15	0.50	0.94
128.8054	6.35E-05	0.700	48.724	3.142	2	1	0	13	1.00	0.87
127.9332	6.31E-05	0.679	51.014	2.791	2	1	0	15	1.00	0.88
130.001	6.41E-05	0.662	51.302	3.081	2	1	0	14	1.00	0.88
129.9339	6.41E-05	0.648	52.184	2.784	3	1	0	15	1.00	0.83
193.9845	9.56E-05	0.813	56.689	4.112	7	4	2	1	0.67	0.13
193.6535	8.50E-05	0.747	60.100	3.535	2	4	0	11	1.00	0.85
188.3373	8.60E-05	0.809	55.549	3.196	4	3	0	10	1.00	0.71
193.9845	8.60E-05	0.813	56.669	4.106	1	3	3	7	0.50	0.88
144.8692	7.14E-05	0.777	49.076	2.593	3	0	1	15	0.00	0.83
143.6852	7.08E-05	0.731	50.505	2.802	2	0	1	15	0.00	0.88
144.4374	7.12E-05	0.716	52.875	3.195	3	1	0	13	1.00	0.81
147.6373	0.000072794	0.707	54.064	3.292	7	1	0	8	1.00	0.53
144.0312	7.10E-05	0.744	51.053	2.708	3	0	1	15	0.00	0.83
210.3084	8.50E-05	0.719	62.820	3.758	2	3	1	11	0.75	0.85
168.451		**0.817**	**52.784**	**2.960**	**3.429**		**0.543**		**0.710**	**0.744**

Table 2: 0.7% agarose data results

0.7% agar:										
Parameters					FALSE	TRUE	FALSE	TRUE		
A_static	Optimum HP	Circularity	Contour Length	Mean bleb diameter	Positives	Positives	Negatives	Negatives	Sensitivity	Specificity
154.369	5.00E-05	0.350	76.457	3.289	8	0	2	21	0.00	0.72
150.528	5.00E-05	0.450	65.338	2.485	6	1	0	26	1.00	0.81
154.840	6.00E-05	0.510	63.432	2.712	8	1	1	22	0.50	0.73
145.682	5.50E-05	0.470	63.373	2.754	5	2	0	23	1.00	0.82
142.759	5.00E-05	0.410	67.365	3.024	7	1	0	22	1.00	0.76
147.167	5.00E-05	0.360	73.474	3.898	4	4	0	19	1.00	0.83
139.173	5.00E-05	0.400	67.760	3.146	6	1	1	21	0.50	0.78
108.264	5.34E-05	0.570	50.879	2.139	9	1	0	24	1.00	0.73
119.974	5.00E-05	0.510	55.036	2.198	6	3	0	25	1.00	0.81
114.099	5.00E-05	0.520	53.731	2.207	8	0	1	23	0.00	0.74
119.944	5.40E-05	0.580	52.582	2.237	6	1	1	23	0.50	0.79
115.284	5.10E-05	0.590	50.055	2.405	3	1	0	21	1.00	0.88
115.788	5.20E-05	0.580	50.029	2.216	3	1	0	23	1.00	0.88
114.617	5.40E-05	0.580	50.739	2.333	5	2	1	21	0.67	0.81
155.124	4.80E-05	0.290	82.978	3.523	9	4	0	24	1.00	0.73
153.537	4.80E-05	0.290	82.174	3.835	9	3	0	21	1.00	0.70
78.722	3.88E-05	0.400	49.768	2.587	5	2	0	19	1.00	0.79
83.919	3.60E-05	0.370	53.321	2.316	5	1	0	23	1.00	0.82
145.460	5.10E-05	0.370	71.872	2.992	8	2	0	24	1.00	0.75
145.788	4.60E-05	0.370	70.981	3.570	4	1	0	20	1.00	0.83
142.165	4.40E-05	0.330	73.860	2.746	5	0	1	26	0.00	0.84
142.795	4.60E-05	0.350	72.147	2.963	7	1	1	23	0.50	0.77
134.477	5.20E-05	0.440	62.695	3.166	5	1	0	20	1.00	0.80
130.362	4.60E-05	0.420	63.141	3.405	4	1	0	19	1.00	0.83
126.593	4.60E-05	0.400	63.327	2.900	4	2	0	22	1.00	0.85
123.451	4.40E-05	0.400	61.988	2.948	3	1	0	21	1.00	0.88
117.985	5.00E-05	0.450	59.074	2.760	8	0	1	20	0.00	0.71
213.894	6.00E-05	0.370	86.821	4.104	11	2	0	21	1.00	0.66
215.446	4.60E-05	0.330	88.855	3.363	8	1	0	26	1.00	0.76
213.433	4.60E-05	0.340	87.121	4.087	5	2	0	21	1.00	0.81
138.854		**0.427**	**65.679**	**2.944**	**6.133**		**0.333**		**0.789**	**0.787**

.3 Myosin-II distribution in chemotaxing *Dictyostelium* cells

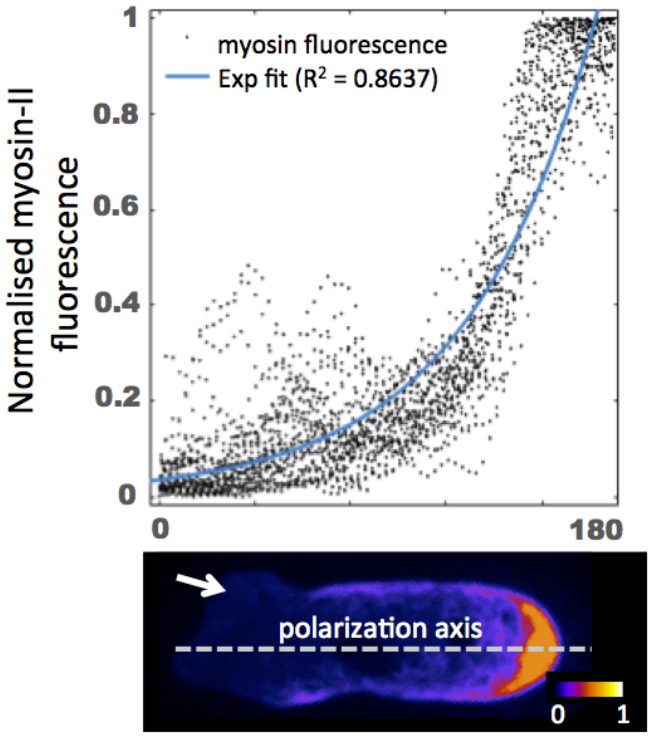

Figure 1: Normalised myosin-II fluorescence for a Dictyostelium cell chemotaxing under 1.5% agar. The normalised fluorescence is plotted along the polarization axis of the cell. 35 time frames from 1 cell were included in the analysis. Blebs are not observed in the areas of highest myosin-II fluorescence, which typically coincide with the cell posterior. Bleb indicated by arrow.

Bibliography

Aizawa, H., Y. Fukui, and I. Yahara
1997. Live dynamics of dictyostelium cofilin suggests a role in remodeling actin latticework into bundles. *Journal of cell science*, 110(19):2333–2344.

Alert, R. and J. Casademunt
2016. Bleb nucleation through membrane peeling. *Physical Review Letters*, 116(6):1–5.

Alert, R., J. Casademunt, J. Brugués, and P. Sens
2015. Model for probing membrane-cortex adhesion by micropipette aspiration and fluctuation spectroscopy. *Biophysical Journal*, 108(8):1878–1886.

Ananthakrishnan, R. and A. Ehrlicher
2007. The forces behind cell movement. *International journal of biological sciences*, 3(5):303.

Bergert, M., S. D. Chandradoss, R. A. Desai, and E. Paluch
2012. Cell mechanics control rapid transitions between blebs and lamellipodia during migration. *Proceedings of the National Academy of Sciences*, 109(36):14434–14439.

Blaser, H., M. Reichman-Fried, I. Castanon, K. Dumstrei, F. L. Marlow, K. Kawakami, L. Solnica-Krezel, C. P. Heisenberg, and E. Raz
2006. Migration of Zebrafish Primordial Germ Cells: A Role for Myosin Contraction and Cytoplasmic Flow. *Developmental Cell*, 11(5):613–627.

Bloomfield, G., D. Traynor, S. P. Sander, D. M. Veltman, J. A. Pachebat, and R. R. Kay
2015. Neurofibromin controls macropinocytosis and phagocytosis in Dictyostelium. *eLife*, 2015(4):1–25.

Bonner, J. T. and L. Savage
1947. Evidence for the formation of cell aggregates by chemotaxis in the development

of the slime mold dictyostelium discoideum. *Journal of Experimental Zoology Part A: Ecological Genetics and Physiology*, 106(1):1–26.

Charras, G. and E. Paluch

2008. Blebs lead the way: how to migrate without lamellipodia. *Nature reviews. Molecular cell biology*, 9(9):730–736.

Charras, G. and E. Sahai

2014. Physical influences of the extracellular environment on cell migration. *Nature Reviews Molecular Cell Biology*, 15(12):813–824.

Charras, G. T., M. Coughlin, T. J. Mitchison, and L. Mahadevan

2008. Life and times of a cellular bleb. *Biophysical journal*, 94(5):1836–53.

Charras, G. T., C. K. Hu, M. Coughlin, and T. J. Mitchison

2006. Reassembly of contractile actin cortex in cell blebs. *Journal of Cell Biology*, 175(3):477–490.

Chen, M.-Y., R. H. Insall, and P. N. Devreotes

1996. Signaling through chemoattractant receptors in dictyostelium. *Trends in genetics*, 12(2):52–57.

Cunningham, C. C.

1995. Actin polymerization and intracellular solvent flow in cell surface blebbing. *The Journal of Cell Biology*, 129(6):1589–1599.

Cunningham, C. C., J. B. Gorlin, et al.

1992. Actin-binding protein requirement for cortical stability and efficient locomotion. *Science*, 255(5042):325.

Dellas, C., D. J. Loskutoff, et al.

2005. Historical analysis of pai-1 from its discovery to its potential role in cell motility and disease. *Thromb Haemost*, 93(4):631–40.

Derivery, E., J. Fink, D. Martin, A. Houdusse, M. Piel, T. E. Stradal, D. Louvard, and A. Gautreau

2008. Free brick1 is a trimeric precursor in the assembly of a functional wave complex. *PloS one*, 3(6):e2462.

Diz-Munoz, A., M. Krieg, M. Bergert, I. Ibarlucea-Benitez, D. J. Muller, E. Paluch, and C. P. Heisenberg
2010. Control of directed cell migration in vivo by membrane-to-cortex attachment. *PLoS Biology*, 8(11).

Diz-Muñoz, A., P. Romanczuk, W. Yu, M. Bergert, K. Ivanovitch, G. Salbreux, C.-P. Heisenberg, and E. K. Paluch
2016. Steering cell migration by alternating blebs and actin-rich protrusions. *BMC biology*, 14(1):74.

Dormann, D., T. Libotte, C. J. Weijer, and T. Bretschneider
2002. Simultaneous quantification of cell motility and protein-membrane-association using active contours. *Cytoskeleton*, 52(4):221–230.

Fackler, O. T. and R. Grosse
2008. Cell motility through plasma membrane blebbing. *The Journal of cell biology*, 181(6):879–84.

Fets, L., J. M. E. Nichols, and R. R. Kay
2014. A PIP5 kinase essential for efficient chemotactic signaling. *Current Biology*, 24(4):415–421.

Fey, P., a. S. Kowal, P. Gaudet, K. E. Pilcher, and R. L. Chisholm
2007. Protocols for growth and development of Dictyostelium discoideum. *Nat Protoc*, 2(6):1307–1316.

Fink, R.
2003. In vivo cytoskeletal dynamics of living fish embryos movie# 2: deep cell circus movements: Actin dynamics. mount holyoke college.

Fink, R. D. and J. Trinkaus
1988. Fundulus deep cells: directional migration in response to epithelial wounding. *Developmental biology*, 129(1):179–190.

Frangogiannis, N. G., C. W. Smith, and M. L. Entman
2002. The inflammatory response in myocardial infarction. *Cardiovascular research*, 53(1):31–47.

Funamoto, S., R. Meili, S. Lee, L. Parry, and R. A. Firtel
2002. Spatial and temporal regulation of 3-phosphoinositides by pi 3-kinase and pten mediates chemotaxis. *Cell*, 109(5):611–623.

Furuta, Y., S. Kanazawa, N. Takeda, K. Sobue, N. Nakatsuji, S. Nomura, J. Fujimoto, M. Okada, T. Yamamoto, S. Aizawa, et al.
1995. Reduced cell motility and enhanced focal adhesion contact formation in cells from fak-deficient mice. *Nature*, 377(6549):539–544.

Gerisch, G.
1982. Chemotaxis in dictyostelium. *Annual Review of Physiology*, 44(1):535–552.

Gerisch, G., R. Albrecht, C. Heizer, S. Hodgkinson, and M. Maniak
1995. Chemoattractant-controlled accumulation of coronin at the leading edge of dictyostelium cells monitored using a green fluorescent protein–coronin fusion protein. *Current Biology*, 5(11):1280–1285.

Gottwald, U., R. Brokamp, I. Karakesisoglou, M. Schleicher, and A. Noegel
1996. Identification of a cyclase-associated protein (cap) homologue in dictyostelium discoideum and characterization of its interaction with actin. *Molecular biology of the cell*, 7(2):261–272.

Goudarzi, M., T. U. Banisch, M. B. Mobin, N. Maghelli, K. Tarbashevich, I. Strate, J. van den Berg, H. Blaser, S. Bandemer, E. Paluch, J. Bakkers, I. M. Tolić-Nørrelykke, and E. Raz
2012. Identification and Regulation of a Molecular Module for Bleb-Based Cell Motility. *Developmental Cell*, 23(1):210–218.

Helfrich, W.
1973. Elastic properties of lipid membranes: theory and possible experiments. *Zeitschrift für Naturforschung C*, 28:693703.

Hoeller, O. and R. R. Kay
2007. Chemotaxis in the absence of pip3 gradients. *Current Biology*, 17(9):813–817.

Holtfreter, J.
1943. Properties and functions of the surface coat in amphibian embryos. *Journal of Experimental Zoology Part A: Ecological Genetics and Physiology*, 93(2):251–323.

Holtfreter, J.
1946. Structure, motility and locomotion in isolated embryonic amphibian cells. *Journal of morphology*, 79(1):27–62.

Iglesias, P. A. and P. N. Devreotes
2008. Navigating through models of chemotaxis. *Current opinion in cell biology*, 20(1):35–40.

Insall, R., A. Kuspa, P. J. Lilly, G. Shaulsky, L. R. Levin, W. F. Loomis, and P. Devreotes
1994. Crac, a cytosolic protein containing a pleckstrin homology domain, is required for receptor and g protein-mediated activation of adenylyl cyclase in dictyostelium. *The Journal of Cell Biology*, 126(6):1537–1545.

Insall, R. H. and L. M. Machesky
2009. Actin dynamics at the leading edge: from simple machinery to complex networks. *Developmental cell*, 17(3):310–322.

Insall, R. H. and O. D. Weiner
2001. Pip3, pip2, and cell movementsimilar messages, different meanings? *Developmental cell*, 1(6):743–747.

Jaglarz, M. K. and K. R. Howard
1995. The active migration of drosophila primordial germ cells. *Development*, 121(11):3495–3503.

Janetopoulos, C., T. Jin, and P. Devreotes
2001. Receptor-mediated activation of heterotrimeric g-proteins in living cells. *Science*, 291(5512):2408–2411.

Kass, M., A. Witkin, and D. Terzopoulos
1988. Snakes: Active contour models. *International Journal of Computer Vision*, 1(4):321–331.

Keller, H. and P. Eggli
1998. Protrusive activity, cytoplasmic compartmentalization, and restriction rings in locomoting blebbing walker carcinosarcoma cells are related to detachment of cortical actin from the plasma membrane. *Cytoskeleton*, 41(2):181–193.

Keller, H., P. Rentsch, and J. Hagmann
2002. Differences in cortical actin structure and dynamics document that different types of blebs are formed by distinct mechanisms. *Experimental cell research*, 277(2):161–172.

Kesbeke, F., B. E. Snaar-Jagalska, and P. Van Haastert
1988. Signal transduction in dictyostelium fgd a mutants with a defective interaction

between surface camp receptors and a gtp-binding regulatory protein. *The Journal of cell biology*, 107(2):521–528.

Kessin, R. H.
2001. *Dictyostelium: evolution, cell biology, and the development of multicellularity*, volume 38. Cambridge University Press.

Kim, J. S., V. S. McKinnis, A. Nawrocki, and S. R. White
1998. Stimulation of migration and wound repair of guinea-pig airway epithelial cells in response to epidermal growth factor. *American journal of respiratory cell and molecular biology*, 18(1):66–74.

King, J. S. and R. H. Insall
2009. Chemotaxis: finding the way forward with dictyostelium. *Trends in cell biology*, 19(10):523–530.

Konijn, T. M.
1972. Cyclic amp as a first messenger. *Advances in cyclic nucleotide research*, 1:17–31.

Kumar, A., Y. Wu, R. Christensen, P. Chandris, W. Gandler, E. McCreedy, A. Bokinsky, D. A. Colón-Ramos, Z. Bao, M. McAuliffe, G. Rondeau, and H. Shroff
2014. Dual-view plane illumination microscopy for rapid and spatially isotropic imaging. *Nature Protocols*, 9(11):2555–2573.

Laevsky, G. and D. A. Knecht
2001. Under-agarose folate chemotaxis of Dictyostelium discoideum amoebae in permissive and mechanically inhibited conditions. *BioTechniques*, 31(5):1140–1149.

Lämmermann, T. and M. Sixt
2009. Mechanical modes of 'amoeboid' cell migration. *Current Opinion in Cell Biology*, 21(5):636–644.

Langridge, P. D. and R. R. Kay
2006. Blebbing of Dictyostelium cells in response to chemoattractant. *Experimental Cell Research*, 312(11):2009–2017.

Leber, T.
1891. *Die Entstehung der Entzündung und die Wirkung der entzündungerregenden Schädlichkeiten: nach vorzugsweise am Auge angestellten Untersuchungen.* Engelmann.

Levchenko, A. and P. A. Iglesias

2002. Models of eukaryotic gradient sensing: application to chemotaxis of amoebae and neutrophils. *Biophysical journal*, 82(1):50–63.

Lim, F. Y., K.-H. Chiam, and L. Mahadevan

2012. The size, shape, and dynamics of cellular blebs. *EPL (Europhysics Letters)*, 100(2):28004.

Lorentzen, A., J. Bamber, A. Sadok, I. Elson-Schwab, and C. J. Marshall

2011. An ezrin-rich, rigid uropod-like structure directs movement of amoeboid blebbing cells. *Journal of cell science*, 124(Pt 8):1256–1267.

Louis, J. M., G. T. Ginsburg, and A. R. Kimmel

1994. The camp receptor car4 regulates axial patterning and cellular differentiation during late development of dictyostelium. *Genes & Development*, 8(17):2086–2096.

Mast, S. O.

1926. Structure, movement, locomotion, and stimulation in amoeba. *Journal of Morphology*, 41(2):347–425.

Maugis, B., J. Brugues, P. Nassoy, N. Guillen, P. Sens, and F. Amblard

2010. Dynamic instability of the intracellular pressure drives bleb-based motility. *Journal of Cell Science*, 123(22):3884–3892.

Meili, R., C. Ellsworth, S. Lee, T. Reddy, H. Ma, and R. A. Firtel

1999. Chemoattractant-mediated transient activation and membrane localization of akt/pkb is required for efficient chemotaxis to camp in dictyostelium. *The EMBO journal*, 18(8):2092–2105.

Merkel, R., R. Simson, D. A. Simson, M. Hohenadl, A. Boulbitch, E. Wallraff, and E. Sackmann

2000. A micromechanic study of cell polarity and plasma membrane cell body coupling in Dictyostelium. *Biophysical journal*, 79(2):707–19.

Mitchison, T. and L. Cramer

1996. Actin-based cell motility and cell locomotion. *Cell*, 84(3):371–379.

Mogilner, A. and G. Oster

1996. Cell motility driven by actin polymerization. *Biophysical journal*, 71(6):3030–3045.

Nelson, R. D., P. G. Quie, and R. L. Simmons
1975. Chemotaxis under agarose: a new and simple method for measuring chemotaxis and spontaneous migration of human polymorphonuclear leukocytes and monocytes. *Journal of immunology (Baltimore, Md. : 1950)*, 115(6):1650–6.

Paluch, E., M. Piel, J. Prost, M. Bornens, and C. Sykes
2005. Cortical actomyosin breakage triggers shape oscillations in cells and cell fragments. *Biophysical journal*, 89(1):724–733.

Pang, K. M., E. Lee, and D. a. Knecht
1998. Use of a fusion protein between GFP and an actin-binding domain to visualize transient filamentous-actin structures. *Current biology : CB*, 8(7):405–408.

Parent, C. A., B. J. Blacklock, W. M. Froehlich, D. B. Murphy, and P. N. Devreotes
1998. G protein signaling events are activated at the leading edge of chemotactic cells. *Cell*, 95(1):81–91.

Parent, C. A. and P. N. Devreotes
1996. Molecular genetics of signal transduction in dictyostelium. *Annual review of biochemistry*, 65(1):411–440.

Parent, C. A. and P. N. Devreotes
1999. A cell's sense of direction. *Science*, 284(5415):765–770.

Park, Y., C. A. Best, K. Badizadegan, R. R. Dasari, M. S. Feld, T. Kuriabova, M. L. Henle, A. J. Levine, and G. Popescu
2010. Measurement of red blood cell mechanics during morphological changes. *Proceedings of the National Academy of Sciences*, 107(15):6731–6736.

Peukes, J. and T. Betz
2014. Direct Measurement of the Cortical Tension during the Growth of Membrane Blebs. *Biophysical journal*, 107(8):1810–20.

Pfeffer, W. F. P.
1884. *Locomotorische richtungsbewegungen durch chemische reize.*

Pinner, S. and E. Sahai
2008. Pdk1 regulates cancer cell motility by antagonising inhibition of rock1 by rhoe. *Nature cell biology*, 10(2):127.

Pollard, T. D. and G. G. Borisy
2003. Cellular motility driven by assembly and disassembly of actin filaments. *Cell*, 112(4):453–465.

Pomorski, P., P. Krzemiński, A. Wasik, K. Wierzbicka, J. Barańska, and W. Kłopocka
2007. Actin dynamics in amoeba proteus motility. *Protoplasma*, 231(1):31–41.

Rakic, P., R. S. Cameron, and H. Komuro
1994. Recognition, adhesion, transmembrane signaling and cell motility in guided neuronal migration. *Current opinion in neurobiology*, 4(1):63–69.

Ramalingam, N., C. Franke, E. Jaschinski, M. Winterhoff, Y. Lu, S. Brühmann, A. Junemann, H. Meier, A. a. Noegel, I. Weber, H. Zhao, R. Merkel, M. Schleicher, and J. Faix
2015. A resilient formin-derived cortical actin meshwork in the rear drives actomyosin-based motility in 2D confinement. *Nature communications*, 6:8496.

Raucher, D., T. Stauffer, W. Chen, K. Shen, S. Guo, J. D. York, M. P. Sheetz, and T. Meyer
2000. Phosphatidylinositol 4,5-Bisphosphate Functions as a Second Messenger that Regulates CytoskeletonPlasma Membrane Adhesion. *Cell*, 100(2):221–228.

Sahai, E. and C. J. Marshall
2003. Differing modes of tumour cell invasion have distinct requirements for rho/rock signalling and extracellular proteolysis. *Nature cell biology*, 5(8):711.

Saxe, C. r., G. T. Ginsburg, J. M. Louis, R. Johnson, P. N. Devreotes, and A. R. Kimmel
1993. Car2, a prestalk camp receptor required for normal tip formation and late development of dictyostelium discoideum. *Genes & Development*, 7(2):262–272.

Saxe III, C. L., Y. Yu, C. Jones, A. Bauman, and C. Haynes
1996. The camp receptor subtype car2 is restricted to a subset of prestalk cells duringdictyosteliumdevelopment and displays unexpected dif-1 responsiveness. *Developmental biology*, 174(2):202–213.

Schuster, S. L., F. J. Segerer, F. A. Gegenfurtner, K. Kick, C. Schreiber, M. Albert, A. M. Vollmar, J. O. Rädler, and S. Zahler
2016. Contractility as a global regulator of cellular morphology, velocity, and directionality in low-adhesive fibrillary micro-environments. *Biomaterials*, 102:137–147.

Spangler, E. J., C. W. Harvey, J. D. Revalee, P. S. Kumar, and M. Laradji
2011. Computer simulation of cytoskeleton-induced blebbing in lipid membranes. *Physical Review E*, 84(5):051906.

Srivastava, N., R. R. Kay, and A. J. Kabla
2017. Method to study cell migration under uniaxial compression. *Molecular biology of the cell*, 28(6):809–816.

Stockem, W., H.-U. Hoffmann, and W. Gawlitta
1982. Spatial organization and fine structure of the cortical filament layer in normal locomoting amoeba proteus. *Cell and tissue research*, 221(3):505–519.

Strychalski, W. and R. D. Guy
2011. A Computational Model of Bleb Formation. (2009):1–16.

Svitkina, T. M. and G. G. Borisy
1999. Arp2/3 complex and actin depolymerizing factor/cofilin in dendritic organization and treadmilling of actin filament array in lamellipodia. *The Journal of cell biology*, 145(5):1009–1026.

T. Mitchison, G. Charras, L. M.
2009. Implications of a poroelastic cytoplasm for the dynamics of animal cell shape. *Cell*, c(3):215–223.

Tinevez, J.-Y., U. Schulze, G. Salbreux, J. Roensch, J.-F. Joanny, and E. Paluch
2009. Role of cortical tension in bleb growth. *Proceedings of the National Academy of Sciences of the United States of America*, 106(44):18581–18586.

Tozluoglu, M., Y. Mao, P. A. Bates, and E. Sahai
2015. Cost-benefit analysis of the mechanisms that enable migrating cells to sustain motility upon changes in matrix environments. *Interface*, 12:20141355.

Tozluoglu, M., A. L. Tournier, R. P. Jenkins, S. Hooper, P. A. Bates, and E. Sahai
2013. Matrix geometry determines optimal cancer cell migration strategy and modulates response to interventions. *Nature cell biology*, 15(7):751.

Tozluolu, M., A. L. Tournier, R. P. Jenkins, S. Hooper, P. a. Bates, and E. Sahai
2013. Matrix geometry determines optimal cancer cell migration strategy and modulates response to interventions. *Nature cell biology*, 15(7):1–14.

Trinkaus, J.
1973. Surface activity and locomotion of fundulus deep cells during blastula and gastrula stages. *Developmental biology*, 30(1):68–103.

Tsujioka, M., S. Yumura, K. Inouye, H. Patel, M. Ueda, and S. Yonemura
2012. Talin couples the actomyosin cortex to the plasma membrane during rear retraction and cytokinesis. *Proceedings of the National Academy of Sciences*, 109(32):12992–12997.

Tyson, R. A., D. Epstein, K. Anderson, and T. Bretschneider
2010. High resolution tracking of cell membrane dynamics in moving cells: an electrifying approach. *Mathematical Modelling of Natural Phenomena*, 5(1):34–55.

Tyson, R. A., E. Zatulovskiy, R. R. Kay, and T. Bretschneider
2014. How blebs and pseudopods cooperate during chemotaxis. *Proceedings of the National Academy of Sciences of the United States of America*, 111(32):11703–8.

Voura, E. B., M. Sandig, and C.-H. Siu
1998. Cell–cell interactions during transendothelial migration of tumor cells. *Microscopy research and technique*, 43(3):265–275.

Watts, D. and J. Ashworth
1970. Growth of myxamoebae of the cellular slime mould dictyostelium discoideum in axenic culture. *Biochemical Journal*, 119(2):171–174.

Wolf, K., I. Mazo, H. Leung, K. Engelke, U. H. Von Andrian, E. I. Deryugina, A. Y. Strongin, E.-B. Bröcker, and P. Friedl
2003. Compensation mechanism in tumor cell migration. *The Journal of cell biology*, 160(2):267–277.

Woolley, T. E., E. A. Gaffney, J. M. Oliver, S. L. Waters, R. E. Baker, and A. Goriely
2015. Global contraction or local growth, bleb shape depends on more than just cell structure. *Journal of Theoretical Biology*, 380:83–97.

Woolley, T. E., E. a. Gaffney, S. L. Waters, J. M. Oliver, R. E. Baker, and a. Goriely
2014. Three mechanical models for blebbing and multi-blebbing. *IMA Journal of Applied Mathematics*, 79(4):636–660.

Wourms, J. P.
1972. The developmental biology of annual fishes. iii. pre-embryonic and embryonic

diapause of variable duration in the eggs of annual fishes. *Journal of Experimental Zoology Part A: Ecological Genetics and Physiology*, 182(3):389–414.

Wu, L., R. Valkema, P. Van Haastert, and P. N. Devreotes
1995. The g protein beta subunit is essential for multiple responses to chemoattractants in dictyostelium. *The Journal of cell biology*, 129(6):1667–1675.

Xiong, Y., C.-H. Huang, P. A. Iglesias, and P. N. Devreotes
2010. Cells navigate with a local-excitation, global-inhibition-biased excitable network. *Proceedings of the National Academy of Sciences*, 107(40):17079–17086.

Yamazaki, S., S. Matsuoka, M. Tsujioka, and M. Ueda
2014. Regulation for Phosphatidylinositol Lipids Signaling System by Talin. *Biophysical Journal*, 106(2):785a.

Yanai, M., C. Kenyon, J. Butler, P. Macklem, and S. Kelly
1996. Intracellular pressure is a motive force for cell motion in amoeba proteus. *Cytoskeleton*, 33(1):22–29.

Yoshida, K. and K. Inouye
2001. Myosin ii-dependent cylindrical protrusions induced by quinine in dictyostelium: antagonizing effects of actin polymerization at the leading edge. *Journal of cell science*, 114(11):2155–2165.

Yoshida, K. and T. Soldati
2006. Dissection of amoeboid movement into two mechanically distinct modes. *Journal of cell science*, 119(Pt 18):3833–3844.

Young, J. and S. Mitran
2010. A numerical model of cellular blebbing: a volume-conserving, fluid-structure interaction model of the entire cell. *Journal of biomechanics*, 43(2):210–20.

Zatulovskiy, E., R. Tyson, T. Bretschneider, and R. R. Kay
2014. Bleb-driven chemotaxis of Dictyostelium cells. *Journal of Cell Biology*, 204(6):1027–1044.